University of St Andrews

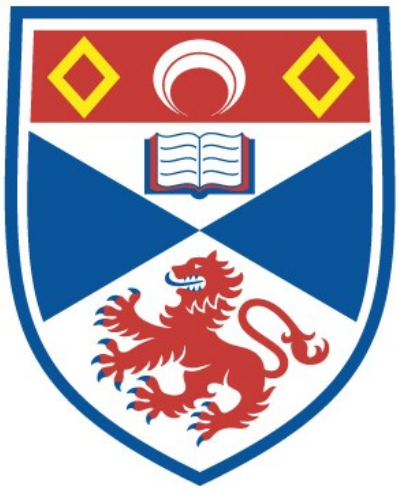

Full metadata for this thesis is available in
St Andrews Research Repository
at:
http://research-repository.st-andrews.ac.uk/

This thesis is protected by original copyright

Few optical-cycle pulse generation in the mid-infrared.

Thesis submitted for the degree of Doctor of Philosophy
to the University of St Andrews by

Thomas Beddard

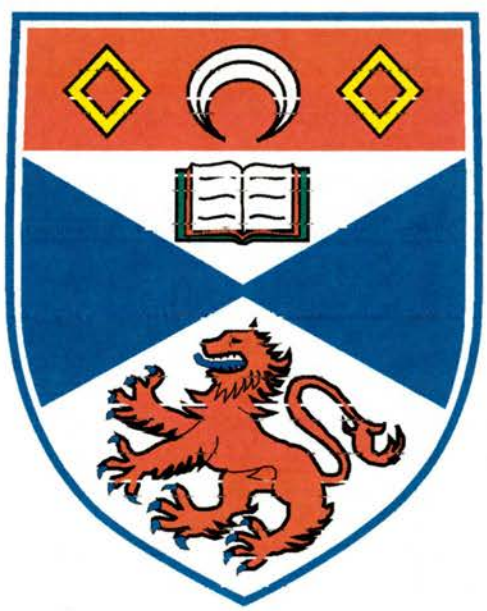

The J F Allen Physics Research Laboratories
School of Physics and Astronomy
University of St Andrews
North Haugh
St Andrews
Fife, KY16 9SS

September 2001

BIBLIOTHECA UNIVERSITATIS ANDREANÆ

Few optical-cycle pulse generation in the mid-infrared.

Thesis submitted for the degree of Doctor of Philosophy
to the University of St Andrews by

Thomas Beddard

Tm
E12.

The J F Allen Physics Research Laboratories
School of Physics and Astronomy
University of St Andrews
North Haugh
St Andrews
Fife, KY16 9SS

September 2001

For Rosamond

Declarations

I, Thomas Beddard, hereby certify that this thesis, which is approximately 32,000 words in length, has been written by me, that is the record of work carried out by me and that it has not been submitted in any previous application for a higher degree.

Date 3/1/2002 Signature of candidate .

I was admitted as a research student in October 1997 and as a candidate for the degree of Doctor of Philosophy in Physics; the higher study for which this is a record was carried out in the University of St. Andrews between 1997 and 2001.

Date 3/1/2002.. Signature of candidate ..

I hereby certify that the candidate has fulfilled the conditions of the Resolution and Regulations appropriate for the degree of Doctor of philosophy in the University of St. Andrews and that the candidate is qualified to submit this thesis in application for that degree.

Date 3/1/2002.. Signature of supervisor..

Copyright

In submitting this thesis to the University of St. Andrews I understand that I am giving permission for it to be made available for use in accordance with the regulations of the University Library for the time being in force, subject to any copyright vested in the work not being affected thereby. I also understand that the title and abstract will be published, and that a copy of the work may be made and supplied to any bona fide library or research worker.

Date 3/1/2002. Signature of candidate ..

Abstract

The work in this thesis describes the design, operation and results of high-repetition rate femtosecond pulse sources aiming for single optical-cycle pulse generation. Two different Ti:sapphire lasers are described for sub-30 fs pulse generation around 815 – 840 nm. They are then used as pump sources for femtosecond optical parametric oscillators (OPO), based on periodically-poled lithium niobate (PPLN) and periodically-poled rubidium titanyl arsenate (PPRTA), which are used for the generation of few optical cycle pulses in the mid-infrared spectral region. The implementation and relevant theory for the measurement of these ultrashort pulses is described using two-photon autocorrelation, frequency resolved optical gating (FROG) and sonogram techniques.

The first Ti:sapphire laser presented is in a ring configuration and created 13 fs pulses with a megawatt of peak power. This laser is used to pump a PPLN-OPO and is the first attempt at frequency down-converting the pump pulses to mid-infrared wavelengths while maintaining the pulse duration, thus reducing the number of optical-cycles within the pulse envelope. A second Ti:sapphire laser with a linear cavity is then used as the pump source for a PPRTA-OPO which creates 100 fs pulses with bandwidths of up to 550 nm, sufficient to support pulses of around three optical cycles.

Then a new approach to mid-infrared pulse generation with an OPO is described in detail, by using an aperiodically poled lithium niobate crystal. Because such an OPO requires the pump pulse to be frequency chirped to match the aperiodicity of its crystal, a FROG characterisation of the pump is described. The results show nearly transform-limited pulses of five optical cycles at 3 μm. A change in the OPO configuration is then discussed as it generated pulses with 720 nm bandwidths. Finally, a method for dispersion compensating these mid-infrared frequency-chirped pulses is described, as such bandwidths are sufficient to support pulses of less than two optical cycles in duration.

Contents

Chapter 1

Ultrashort Laser Pulse Generation

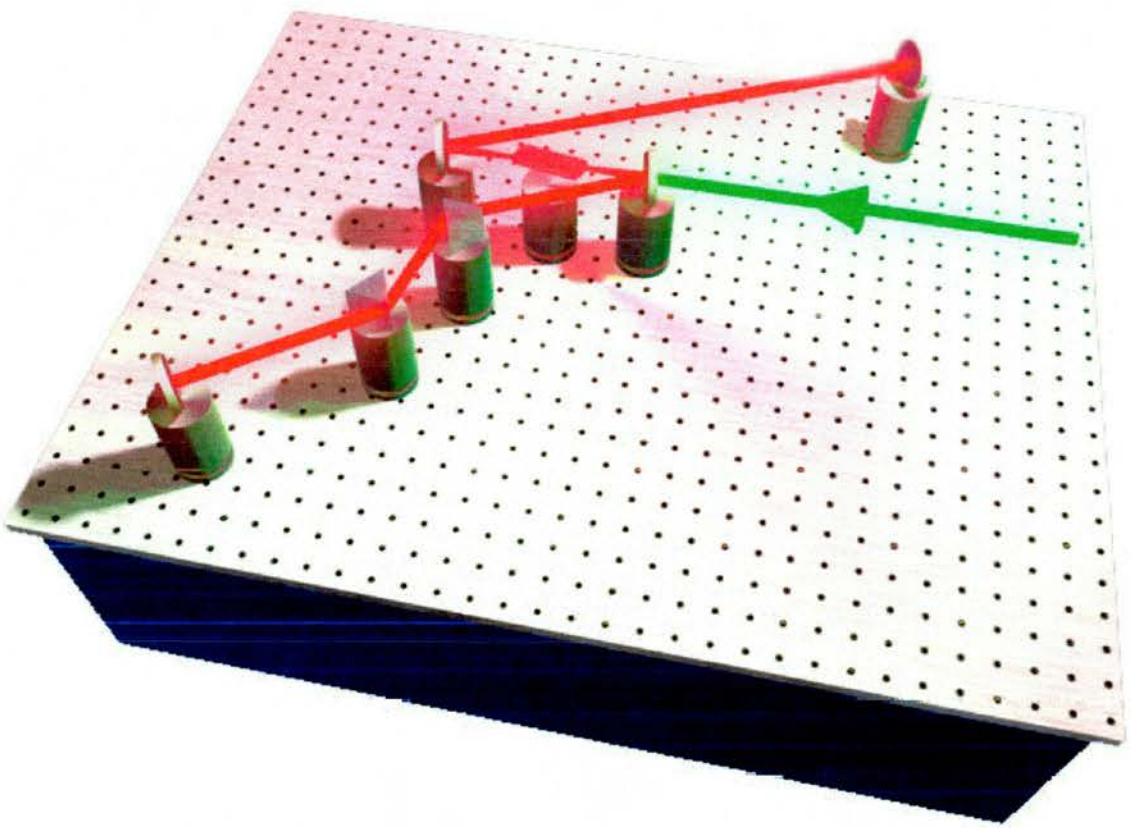

Artistic visualisation of a basic Ti:sapphire laser cavity.

1 Few optical-cycle pulse generation

The field of ultrashort pulse laser research is home to the shortest ever man-made events. Electronics may produce electric currents lasting a few picoseconds, and particle physics may create collision products which last for a few hundred femtoseconds, but both are slouches compared to the optical pulses available from modern lasers. The shortest optical pulses are now less than 5 fs in duration [1,2]. Such ultrashort pulse durations are defined by the time for which the intensity is greater than half the maximum value. Most pulses have durations much longer than the time taken for the electric field to complete one *cycle*, λ / c, where λ is the centre wavelength of the pulse and c the speed of light. So to date, the shortest laser pulses of sub 5 fs therefore contain less than 2 optical cycles, meaning that the electric field has only oscillated twice.

The history of few optical cycle pulse generation began in 1985 with the demonstration of 8 fs (4 cycle) pulses from a dye laser amplifier system operating at 620 nm [3]. A subsequent experiment in 1987 produced 6 fs (3 cycle) pulses and set a record for the shortest pulses ever created which held for ten years [4].

Generating few-cycle pulses directly from a laser is more difficult as the creation, amplification and phase control of the pulse must be carried out in a single cavity. Soliton lasers were the first to demonstrate few-cycle pulses directly. They operated in the infrared where the dispersion of a glass fibre can be very low. Two groups in 1987 reported 4 cycle pulses from such lasers at wavelengths of 1.3 μm and 1.5 μm, [5,6].

The real breakthrough in generating high quality few-cycle pulses came with a better understanding on how to control dispersion of the pulses inside the laser,

as we will see in Section 1.5. Research in the early 1990s showed that a carefully chosen pair of prisms in the laser cavity could simultaneously minimise second and third order dispersion [7] and a number of systems were demonstrated which produced pulses as short as 11 fs (4 cycles) [8,9].

Even shorter durations came in 1995 with the arrival of technology allowing the manufacture of dispersion engineered mirrors, described at the end of Section 1.5, [10,11]. By matching the mirror dispersions to that of the crystal, a laser cavity could be made with exactly the required phase characteristics. Pulses as short as 7.5 fs (2.8 cycles) were obtained from a laser comprising of no more than four mirrors and a Ti:sapphire crystal by the pioneers of this approach at the Technical University of Vienna [12]. A year later similar work at the Swiss Federal Institute of Technology obtained 6.5 fs (2.5 cycle) pulses directly from a laser [13].

The shortest pulses so far have been generated by broadening the spectral bandwidth of the laser pulse in an optical fibre then compressing the output. Using this method, researchers at the University of Groningen produced 4.9 fs (1.8 cycle) pulses [1].

Although optical pulses have yet to reach single-cycle durations, researchers looking at the terahertz region of the electromagnetic spectrum have created transient electric fields which can be launched into free space as picosecond pulses with durations of less than one cycle [14]. However, it is more straightforward to produce single or sub-cycle pulses at these wavelengths as they share more in common with radio waves than light.

Finally, few optical cycle pulse generation is possible in the mid-infrared using an optical parametric oscillator (OPO). By employing an ultrashort laser as the pump source for an OPO, pulses can be produced with a similar duration to the

pump laser but with much longer carrier wavelengths, which results in a dramatic reduction in the number of cycles within the intensity envelope. This thesis involves such experiments and mid-infrared pulses were created that contained less than 5 optical cycles [15].

1.1 Applications of few optical-cycle pulses

Before we start looking at the theory of ultrashort pulse generation, it is worth considering a few possible applications for such sources, which ultimately provide motivation for the research.

Broadband laser spectroscopy using a single pulse could become a reality with a near single-cycle mid-infrared source. For example in Figure 1-1, a single-cycle pulse centred at 3 μm would have a bandwidth broad enough to encompass several important chemical bond (C-H, O-H and N-H) and molecular resonances (H-H, H-Cl, H-Br and H-F). Using these pulses, an absorption spectrum of a molecule or reaction could be probed in a single shot so that the proportion of different reagents could be frozen in time. The conventional sources used for infrared spectroscopy provide high quality output over a narrow spectral region (such as lead-salt or gas lasers), or are broad bandwidth and coherence (e.g. glowbars). However, few-cycle mid-infrared pulses could provide coherent radiation over a huge bandwidth allowing novel interferometric or phase-sensitive techniques to be applied, which otherwise would not be possible.

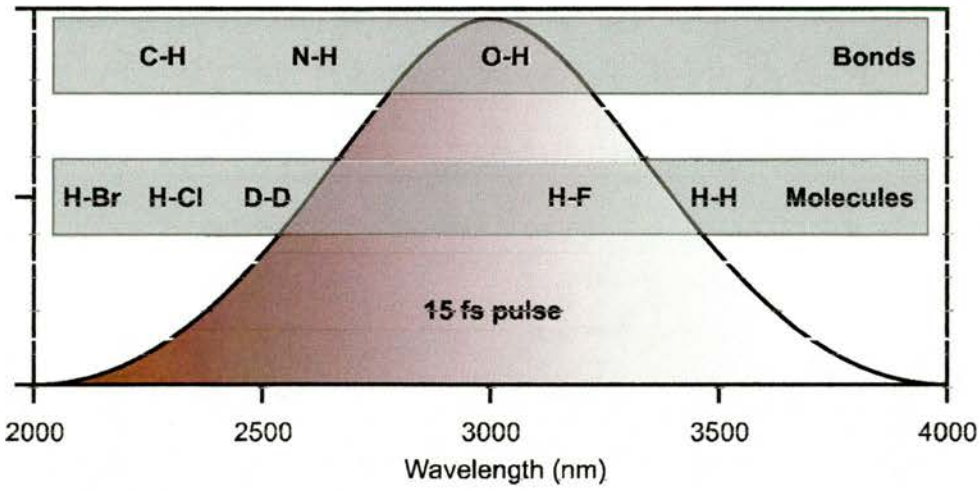

Figure 1-1 The broad bandwidth of a 1.5 cycle pulse is capable of exciting a number of chemical bonds and molecular resonances.

Another application is the coherent quantum control of molecules [16] where the objective is to prepare the molecule in a particular vibrational state of motion at a given time. Molecular vibration is quantised in discreet modes of oscillation, each with its own characteristic resonant frequency. The range of vibrational modes broadens the absorption spectrum of a molecule by providing a variety of vibrational levels to which an electron can be excited. Therefore, a chirped broadband pulse from an ultrashort pulse laser can be used to excite individual vibrational modes at different times, in a controlled fashion. This idea provides a way to localise the position and momentum of the atoms (within the limits of the Heisenberg uncertainty principle) in a molecule at a selected time. Using pulse characterisation techniques similar to those described in Chapter 3, the chirp on the pulse could be arranged, so that some time after excitation, the vibrational modes constructively interfere in a way that allows the bond displacement and motion to be know precisely. Quantum control in a molecule of iodine using 49 fs pulses has already been demonstrated [16], but the potential of using mid-infrared pulses for the control of rotational modes to excite a vibrational transition to different rotational states remains promising.

Understanding the more fundamental aspects of electromagnetic wave propagation has always been a motivation for generating few optical cycle pulses. Typically, the temporally dependent electric field associated with an optical pulse is represented with complex field amplitude

$$E(t) = \mathcal{E}(t)e^{i\phi(t)}e^{i\omega_0 t}, \tag{1.1}$$

where ω_0 is the optical carrier frequency, $\mathcal{E}(t)$ is the time varying electric field envelope and $\phi(t)$ represents the phase variation across the pulse. This equation contains the approximation that the pulse envelope is slowly varying with respect to the carrier frequency ω_0 i.e. $\Delta\omega/\omega_0 \ll 1$. This is known as the slowly varying envelope approximation (SVEA) [17]. In the SVEA limit the carrier period is much faster than the duration of the pulse. However, for few-cycle pulses the approximation will not hold, meaning that new theories of pulse propagation in dispersive media or for nonlinear frequency conversion will have to be found from the general solution of Maxwell's equations.

Experimentalists are now finding the breakdown of the SVEA to be a growing problem. Research at the Technical University of Vienna showed that for a 10 fs pulse from a Ti:sapphire laser the phase of the carrier wave does not remain locked to the envelope, but instead changes with each successive pulse [18]. As pulse durations approach that of the single-cycle, the pulse and carrier envelopes can no longer be distinguished as separate components, as Figure 1-2 illustrates. Thus, the new challenge is to achieve relative phase control as well as *absolute* phase control so that the electric field amplitude remains constant from one pulse to the next.

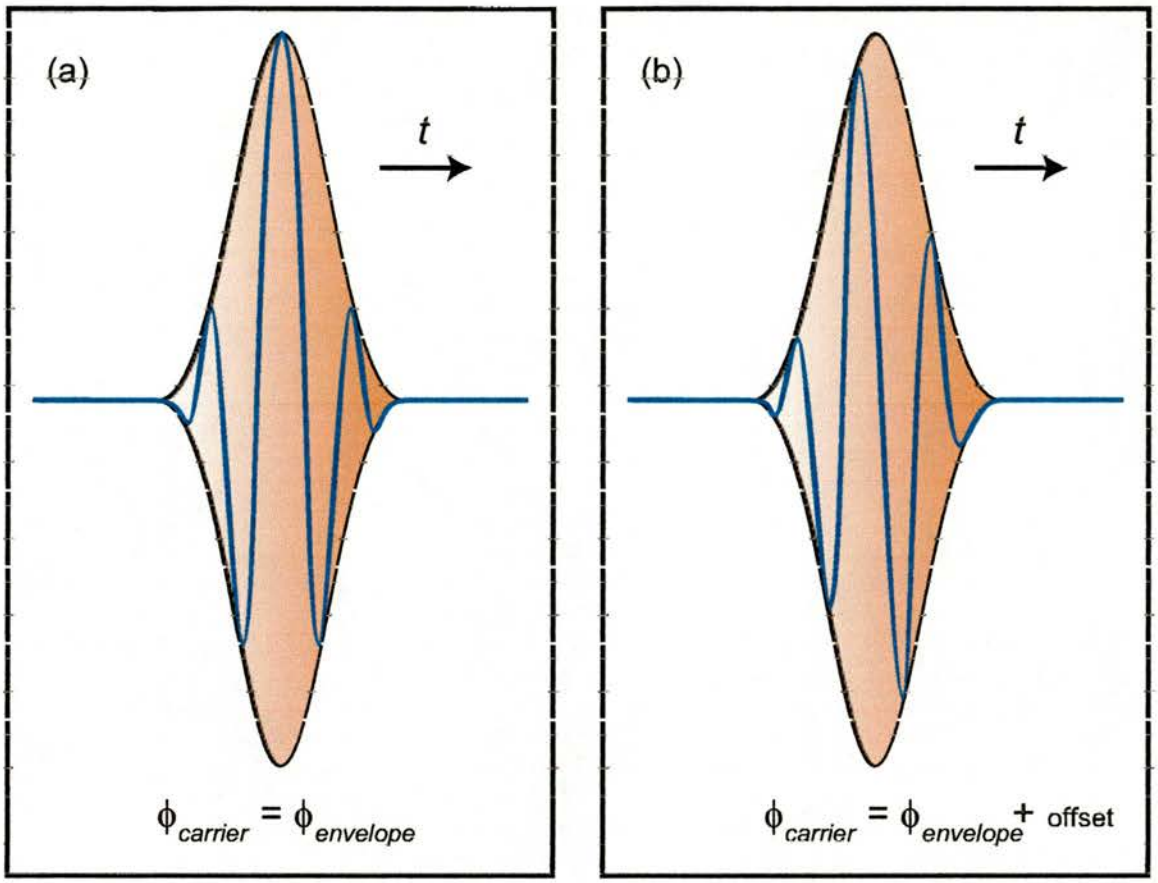

Figure 1-2 The effect of absolute carrier phase on the shape of a single-cycle pulse. The pulse envelope remains unchanged, but the phase relative to the carrier frequency determines the exact form and peak of the electric field. The carrier phase changes from pulse to pulse.

Now that we have discussed the history and motivation of few optical-cycle pulse generation, we shall continue with an overview of laser theory.

1.2 Ti:sapphire as a laser gain medium

The Ti:sapphire laser was first demonstrated in 1982 by Moulton [19,20] and has since become one of the most popular practical gain media. It offers use in the near-infrared spectral region and provides wide tunability, high output powers and is compatible with straightforward modelocking procedures.

One of the most striking features of the Ti:sapphire laser is its broad tuning range of between 660 nm and 1180 nm, which extends well beyond that of any single dye laser. The Ti:sapphire laser made the transition from a subject of laboratory research to commercial availability, and has now found its way back into the laboratory as a tool for new scientific and technological study.

Ti:sapphire ($Ti:Al_2O_3$) is a uniaxial crystal consisting of a sapphire (Al_2O_3) host doped with a small percentage (~0.1%) of titanium ions (Ti^{3+}). Its crystal structure consists of either a Ti^{3+} ion or an Al^{3+} ion surrounded by an octahedral arrangement of six O^{2-} ions, see Figure 1-3.

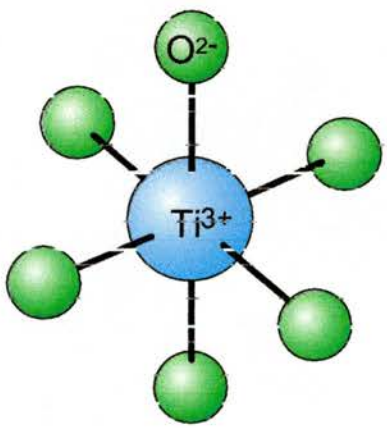

Figure 1-3. The molecular structure of Ti:sapphire

The electronic structure of the Ti^{3+} ion is a closed shell plus a single 3*d* electron [20]. The free-space, five-fold degenerate *d*-electron levels are split by the crystal field of the host. In the host Al_2O_3 the site for the Ti^{3+} ion has trigonal symmetry. The crystal field can be viewed as the combination of cubic and trigonal-symmetry components. The cubic field dominates and splits the Ti^{3+} energy levels into a triply degenerate $^2T_2$ ground state and a doubly degenerate ^2E excited state, see Figure 1-4. The trigonal field splits the ground $^2T_2$ into two levels, and the lower of these two levels is split further into two levels by the spin-orbit interaction. It is between the $^2T_2$ and ^2E levels that the laser transition takes place. Higher lying energy states of the Ti^{3+} ion require energy promotion of the single electron of the outer 3*d* shell. The energies required to achieve such transitions are substantially far greater than those required for optical pumping to establish a population inversion as subsequent laser action. Thus, the Ti:sapphire laser performance is not compromised by excited-state absorption of either the pump or the laser radiation.

The peak absorption from the ground $^2T_2$ state to the excited ^2E state occurs in the visible spectral region at 495 nm and is characterised by a dual peak spectrum caused by the Jahn-Teller splitting. Fluorescence occurs between 600 – 1100 nm with a peak at around 790 nm. Figure 1-5 shows typical absorption and fluorescence spectra for Ti:sapphire at room temperature [20].

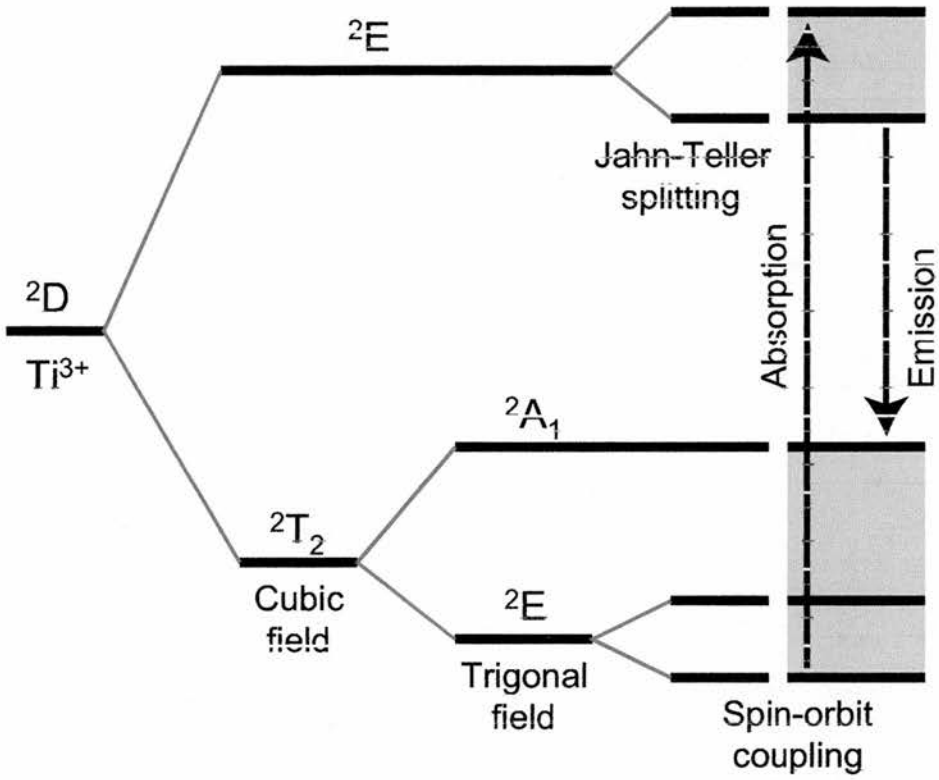

Figure 1-4. Energy level splitting in Ti:sapphire

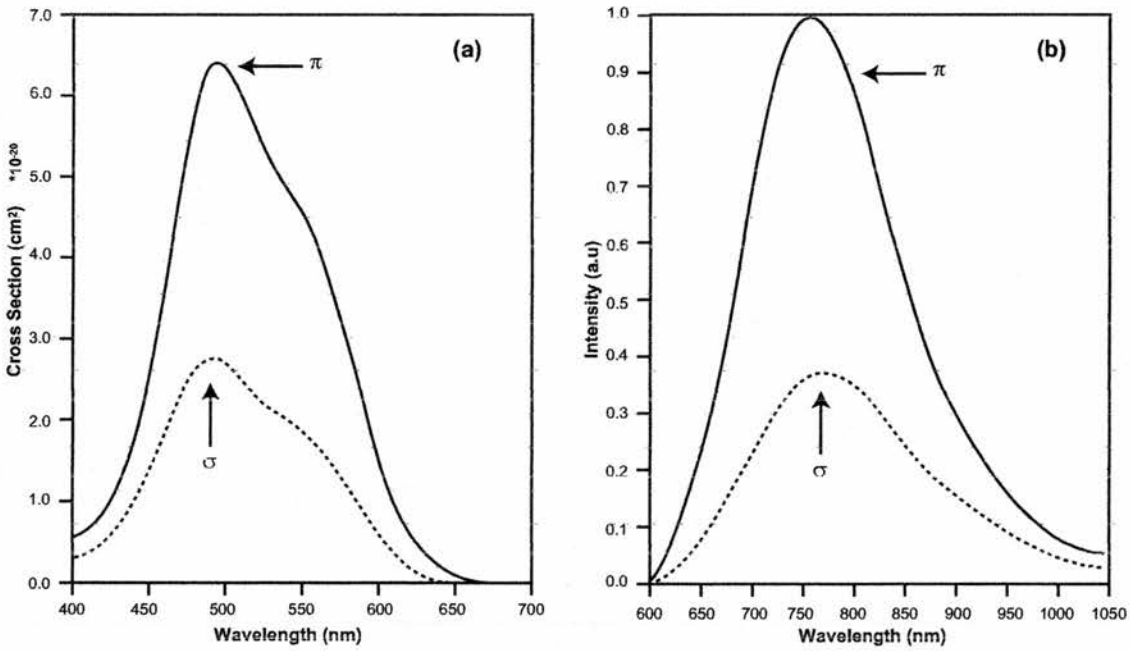

Figure 1-5. (a) Polarised absorption cross sections for the $^2T_2 \rightarrow {}^2E$ transition, and (b) polarised fluorescence spectra of Ti:sapphire [20].

The crystalline environment for the Ti^{3+} ion not only creates the levels needed for laser operation but can, by lowering the symmetry surrounding the ion, induce an electric dipole moment between the $^2T_2$ and ^2E states. The trigonal symmetry for Ti^{3+} in sapphire is particularly effective in creating a large dipole moment, and this is reflected in the relatively short (for solid state lasers) radiative lifetime of 3.15 μs (at 300 K) for the Ti:sapphire laser transition [20]. The resultant laser gain cross-section for the Ti:sapphire is higher, by at least an order of magnitude, than that for other 3d transition metal tunable lasers.

The short excited state lifetime of 3.15 μs for Ti:sapphire limits the type of pump sources to continuous wave (cw), short-pulse or Q-switched lasers. At higher temperatures, the upper state lifetime falls, and significant non-radiative decay occurs [21]. These non-radiative processes are less significant at room temperature and it is sufficient to cool the Ti:sapphire crystal using a simple low-pressure water-cooling system to 15° C. A further advantage of Ti:sapphire as a laser gain medium is its relatively large stimulated emission cross-section of $3x10^{-19}$ cm^2, which allows crystal lengths of a few millimetres to be used, compared to a few centimetres for Nd:YAG crystals. Some properties of Ti:sapphire are given in Table 1-1, for a crystal temperature of 300 K.

Traditionally, Ti:sapphire lasers were pumped by argon-ion lasers that produce noisy fluctuations in output power at 488 nm and 514 nm. Although these ion lasers are capable of producing powers in the 10 – 20 W range, they are inefficient, bulky and expensive to run; a three-phase electricity supply and high-pressure water-cooling is required.

Property	Value at 300 K
Refractive index	1.760
Nonlinear refractive index	$3x10^{-16}$ cm^2W^{-1}
Upper state lifetime	3.15 μs
Absorption coefficient	0.7 – 3 cm^{-1}
Gain cross-section	3 – $4x10^{-19}$ cm^2
Thermal conductivity	0.33 $Wcm^{-1}K^{-1}$
Peak absorption	490 nm
Peak emission	790 nm
Ti^{3+} concentration	1 – $5x10^{19}$ cm^{-3}

Table 1-1 Material and spectroscopic properties of Ti:sapphire

Development of all-solid-state diode-pumped frequency-doubled Nd:YLF, Nd:YAG and Nd:YVO_4 lasers has allowed smaller, more efficient pump lasers to take the place of the argon-ion laser. For example, the Spectra-Physics Millennia[22] (based on frequency–doubled, diode-pumped Nd:YVO_4) is a more compact device powered by single-phase mains electricity with a closed-loop water cooling system. Present models deliver output powers of either 5 W or 10 W at a wavelength of 532 nm.

1.3 Modelocking

Modelocking requires a broadband gain medium, such as Ti:sapphire, which will sustain well over 100,000 longitudinal modes in a typical laser cavity. With this it is possible to generate pulses of the order of a few femtoseconds (~10^{-15} s). The term modelocking comes from the description of the laser in the frequency domain, where the emission is considered to be made up of the sum of the radiation of each of these longitudinal modes:

$$E(t) = \sum_m E_m e^{i\left[(\omega_0 + m\Delta\omega)t + \phi_m\right]}, \tag{1.2}$$

where φ_m is the phase of the mth mode and ω_0 is chosen arbitrarily as a reference frequency. The modes have an equal frequency spacing of

$$\Delta\nu = \frac{c}{2nL}, \tag{1.3}$$

where $2nL$ is the optical path length of the laser cavity and c is the speed of light in the medium. In a free-running laser, the phases of this comb of equally spaced modes will be set randomly. The time domain transformation of such a frequency spectrum is an infinite series of identical bursts of incoherent light (Figure 1-6b), spaced in time by $T_{RT} = 1/\Delta\nu$, which is the time needed to complete a cavity round-trip. Forcing all the modes to have equal phase – a procedure called modelocking – implies that in the time domain all the waves of different frequency will add constructively at one point, resulting in a very intense and short pulse of light, Figure 1-6c. The inverse Fourier transform of an infinite series of "δ functions" equally spaced in frequency and in phase, is in the time domain, an infinite train of "δ functions" or infinitely short pulses. The modes of a linear or ring laser cavity offer a good approximation to the infinite

comb of delta functions in the frequency domain, and shows that the more modes a laser medium can support, the shorter the pulses it can generate [17].

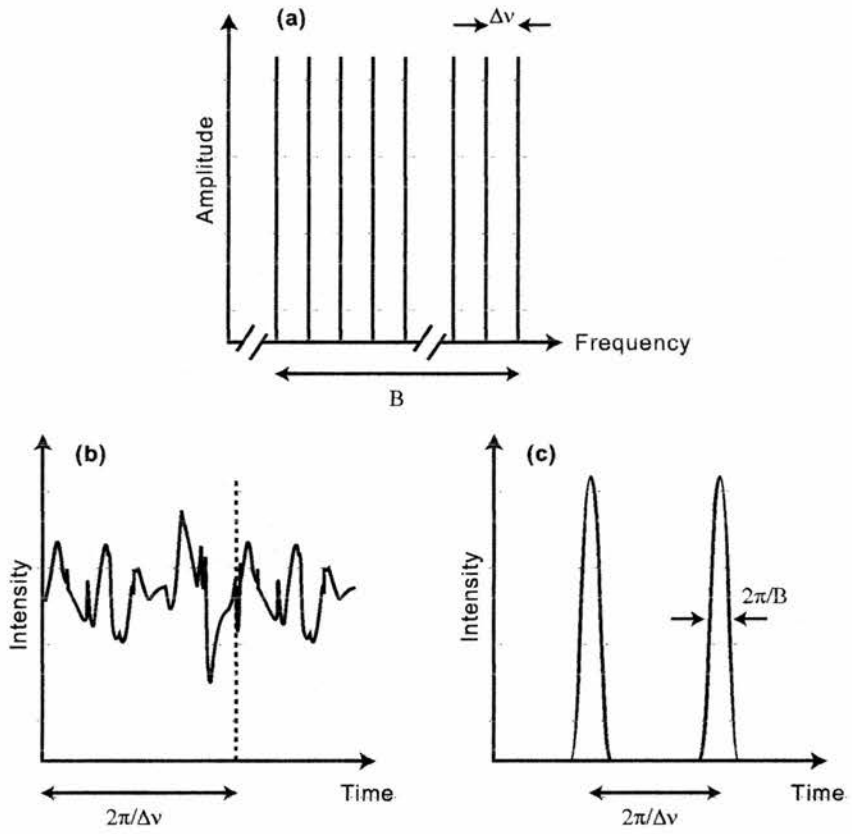

Figure 1-6 (a) A comb of equally spaced modes with the inverse Fourier transform for (b) random phase distribution and (c) all the modes are locked to the same phase.

The conditions required for modelocking can be considered in terms of the behaviour of the intracavity laser field with time. A laser will favour modelocked operation over cw operation if the cavity is aligned such that the gain required by an ultrashort pulse is less than that required during cw operation. Applying a periodic modulation to the cw field will enhance and amplify noise fluctuations until the gain required by ultrashort pulse operation is less per round-trip than for cw operation. At this point modelocking is achieved.

There are two main mechanisms to achieve modelocking in a laser; active and passive modelocking [23]. The following sections present a brief review of these mechanisms.

Active Modelocking

With active modelocking, an amplitude or phase modulator can be used to generate ultrashort pulses. With an amplitude modulator, it is placed inside the laser cavity and the round-trip frequency of the laser is exactly matched to the modulator's frequency, ω_n. In the frequency domain, each of the longitudinal modes present in the laser cavity at frequency, ω_q, will acquire modulation sidebands at frequencies, $\omega_q \pm n \times \omega_n$, because of the active modulator. The modulation sidebands from each longitudinal mode will fall on top of the other longitudinal modes in the cavity. Each of these side bands will then tend to "injection lock" the longitudinal mode with which it is in resonance and so the modulator will couple together, or modelock, each longitudinal mode to its neighbouring modes.

Modulators that use internal phase rather than loss can also be used for modelocking. This can be done by using an intracavity electro-optic crystal that will cause a phase delay to the oscillating wave proportional to the instantaneous electric field across the crystal. If the frequency of the modulating signal is chosen to match the longitudinal inter-mode frequency separation, then the distribution of energy of the modulated electric beam will form sidebands as a function of the frequency of the modulation. As in the loss modulation case, the modes will become coupled with locked phases.

By its very nature, active modelocking requires an additional component within the laser cavity that requires precise control. This adds to the experimental complexity of a system. A more elegant approach is to use a passive modelocking device which relies on the nonlinear response of an element when placed within a laser field.

Passive modelocking

In some lasers, the periodic gain gating effect occurs spontaneously and relies on the circulating laser field. In this case the laser cavity will include a nonlinear optical element, e.g. saturable dye, which posses an intensity-dependent loss such that the higher intensity features (e.g. noise spikes) of the circulating field experience less loss. Modelocked operation is favoured over free running cw operation because the phases of individual modes adjust themselves to maximise the rate of stimulated emission inside the gain medium [24]. Significantly shorter pulse durations can be obtained with passive modelocking compared to active modelocking schemes because the pulse shortening is driven by the circulating field. Exploitation and optimisation of passive modelocking in a Ti:sapphire laser has allowed the generation of pulses shorter than 5 fs [1].

There are several mechanisms to achieve passive modelocking. Some are based on the insertion of a slow or fast saturable absorber inside the laser cavity [25,26]. Others use a regenerative modelocking technique to form a high intensity pulse to initiate self-modelocking [27]. However, the most important modelocking technique (and relevant for this work since it occurs in Ti:sapphire), is based on passive modelocking using an effective fast saturable absorber and is called self-modelocking or Kerr-lens modelocking [28].

Kerr-lens modelocking

In a typical Ti:sapphire laser, the transverse (spatial) cavity mode is focused to a beam radius of a few tens of microns within the gain medium. The high power density this produces induces a nonlinearity at the frequency of the excited wave inside the crystal. This gives rise to an instantaneous change in the refractive index n_0, which is proportional to the intensity as:

$$n = n_0 + n_2 I(t) \tag{1.4}$$

where n_2 is a nonlinear coefficient. This intensity dependence of refractive index causes the optical Kerr effect [29], which can be used to produce self-phase modulation (SPM) in its longitudinal form, or self-focusing (or a Kerr lens) in the transverse form. SPM can be of benefit to an ultrashort pulse laser as it adds spectral components to the pulse allowing, with suitable phase correction, the generation of much shorter pulse durations. Self-focusing is a dramatic consequence of a nonlinear refractive index resulting in a larger index of refraction at the centre of the beam than that at its edges. Thus, the phase velocity of the wavefront will be less at the centre of the beam than at the periphery, turning the medium into an intensity dependent positive lens, which produces a progressively smaller beam waist for increasing light intensities. If an aperture is placed at a location within the laser cavity, see Figure 1-7a, such that the laser will incur less loss for high intensities, an effective saturable absorber is formed. In a suitably aligned laser cavity, such a passive amplitude modulation mechanism can favour modelocking over cw operation [28]. Self-modelocking can, however take place without any intracavity "hard" aperture, but instead use a "soft" aperture [30]. Soft-aperture modelocking occurs when the laser is configured so that the pulsed mode experiences greater overlap

with the pump beam in the laser crystal than the cw mode, and therefore experiences higher gain, see Figure 1-7b.

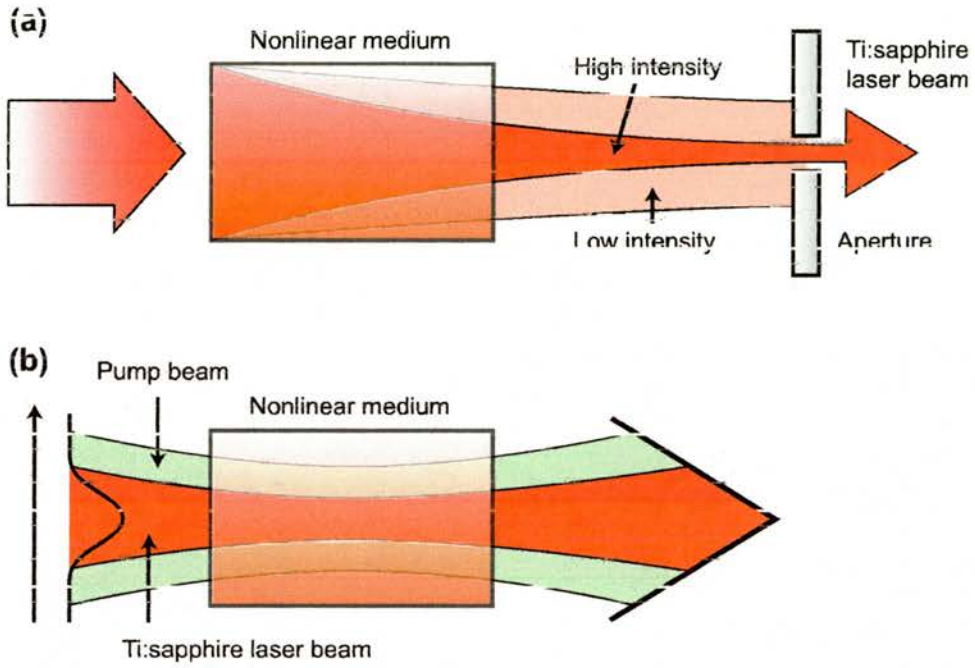

Figure 1-7. Self-focusing of a laser beam for (a) hard aperture self-modelocking and (b) soft aperture self-modelocking

Although a self-starting self-modelocked laser has been reported [31], most cases require a mechanism to create a primitive pulse of sufficient intensity to initiate the modelocked pulse train. There are several mechanisms used to initiate modelocking, the most common options being an extracavity moving mirror [32], a semiconductor saturable absorber mirror structure (SESAM) [33], or most commonly by physically tapping a cavity end mirror or prism [28]. This last method is described in more detail in Chapter 4 along with an experimental description of a self-starting self-modelocked Ti:sapphire ring laser that has no intracavity elements other than the laser rod and dispersion compensating prisms.

1.4 Linear & nonlinear optics

When a dielectric material is in the presence of an electromagnetic field E, a corresponding polarisation is induced. The induced polarisation effect, $P(\omega)$, responds linearly to the incident radiation if the field strength is low. However, when the applied field strength is comparable to the inter-atomic electric field within the dielectric, the induced polarisation has a nonlinear relation to the field strength. The frequency response of the system is characterised by the atomic susceptibility $\chi^{(1)}(\omega)$, which gives rise to linear optical effects such as refractive index, dispersion and birefringence and relates the electric and polarisation fields by:

$$P(\omega) = \varepsilon_0 \chi^{(1)}(\omega) E(\omega) \tag{1.5}$$

where $E(\omega)$ is the electromagnetic field, and ε_0 is the permittivity of free space. The refractive index is defined in terms of the atomic susceptibility:

$$n(\omega) = \sqrt{1 + \chi'(\omega)} \tag{1.6}$$

where $\chi'(\omega) = \mathrm{Re}(\chi(\omega))$. The frequency dependence of the refractive index is known as dispersion. This can be used to define a frequency dependent propagation constant, $\beta(\omega)$, where:

$$\beta(\omega) = n(\omega)\frac{\omega}{c} \tag{1.7}$$

A Taylor series expansion of β about a centre frequency ω_0 gives the expression:

$$\beta(\omega) = \beta_0 + \beta_1(\omega - \omega_0) + \tfrac{1}{2}\beta_2(\omega - \omega_0)^2 + \tfrac{1}{6}\beta_3(\omega - \omega_0)^3 + \ldots \tag{1.8}$$

The β coefficients in the expansion above describe the various different physical effects governing the propagation of a pulse through a medium. β_0 relates to the phase velocity and is written as:

$$\beta_0 = \frac{\omega_0}{v_\phi} \tag{1.9}$$

The phase velocity, v_ϕ, relates to propagation at the central carrier frequency ω_0. However, different frequencies within the pulse travel at different velocities. In a normally (or positively) dispersive system, the longer wavelength components of the pulse travel faster than the shorter wavelengths. Thus, the pulse envelope propagates with an instantaneous group velocity v_g. The second coefficient of the expansion, β_1, is related to the group velocity by:

$$\beta_1 = \frac{\mathrm{d}\beta}{\mathrm{d}\omega} = \frac{1}{c}\left(n + \omega\frac{\mathrm{d}n}{\mathrm{d}\omega}\right) = \frac{1}{v_g} \tag{1.10}$$

When broad bandwidth ultrashort pulses propagate through dispersive materials, the group velocity dispersion (GVD) is the most significant pulse broadening effect. GVD is represented by β_2 and can be written as:

$$\beta_2 = \frac{\mathrm{d}\beta_1}{\mathrm{d}\omega} = \frac{1}{c}\left(2\frac{\mathrm{d}n}{\mathrm{d}\omega} + \omega\frac{\mathrm{d}^2 n}{\mathrm{d}\omega^2}\right) = D \tag{1.11}$$

If β_2 is zero, the pulse will propagate indefinitely, without any change to its temporal envelope. Many glasses have a wavelength for which $\beta_2 = 0$, this is called the "zero dispersion wavelength". Third-order dispersion (TOD) effects become significant when generating pulses of tens of femtoseconds and therefore have to be compensated for. The third-order dispersion of a material is given by:

$$\beta_3 = \frac{d\beta_2}{d\omega} = \frac{1}{c}\left(3\frac{\mathrm{d}^2 n}{\mathrm{d}\omega^2} + \omega\frac{\mathrm{d}^3 n}{\mathrm{d}\omega^3}\right) \tag{1.12}$$

1.4.1 Nonlinear polarisation

The polarisation of equation (1.5) can be re-written for high fields resulting in the nonlinear relationship:

$$P = \varepsilon_0 \chi^{(1)} E + \chi^{(2)} E^2 + \chi^{(3)} E^3 + \ldots \quad (1.13)$$

where $\chi^{(i)}$ is a tensor describing the nonlinear susceptibilities of the medium. The magnitudes of $\chi^{(i)}$ decrease rapidly with increasing i, which is why high field strengths are required for significant nonlinear effects. $\chi^{(2)}$ gives rise to second harmonic generation, sum- and difference-frequency mixing and parametric generation. $\chi^{(3)}$ is responsible for cubic nonlinear effects such as third harmonic generation, the Kerr effect and SPM.

1.4.2 Self-phase modulation

SPM is the change in the phase of an optical pulse due to an intensity-induced nonlinearity in the refractive index of the material, induced by the propagating pulse, and is defined by equation (1.4) [23]. With regard to equation (1.4), the $n_2 I(t)$ describes the optical Kerr effect and causes the pulse to suffer a time-dependent phase delay, which also depends on the intensity of the pulse:

$$\phi_{NL}(t) = \frac{2\pi}{\lambda} n_2 I(t) L \quad (1.14)$$

Here L is the length of the medium. Thus, the induced nonlinear refractive index is responsible for the SPM of the pulse.

For a short intense pulse, this phase delay causes a nonlinear instantaneous frequency chirp defined as

$$\Delta\omega(t) = -\frac{d\phi}{dt} = -\frac{2\pi}{\lambda} n_2 \frac{dI(t)}{dt} L \quad (1.15)$$

For a pulse propagating through a dielectric medium (of $n_2 > 0$), the refractive index increases with intensity, reaching to a maximum at the peak of the pulse then returning to its original value after the trailing edge of the pulse. This causes a rapid response in the media. Due to this change in the refractive index, the leading edge of the pulse will be shifted to lower frequencies while the trailing edge to higher frequencies because the arrival of the shorter wavelengths are delayed. For a smooth pulse temporal profile, as shown in Figure 1-8a, the central region of the pulse will experience an approximately linear frequency chirp. Figure 1-8b shows the corresponding pulse spectrum which is characteristic of the spectra measured in the lab of pulses with a high degree of SPM. The peaks within the spectrum are characteristic of SPM and are the result of interference between spectral components occurring at different times, due to the shape of the frequency shift.

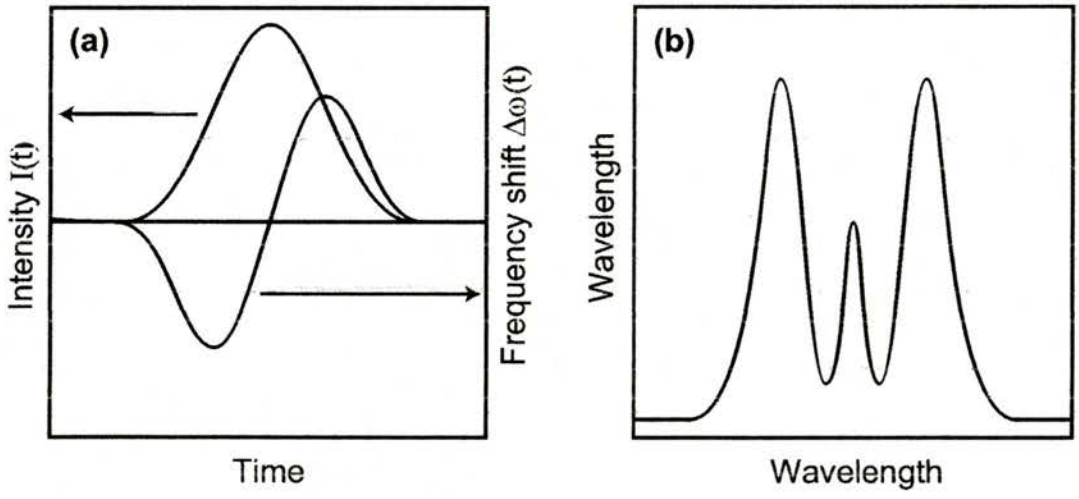

Figure 1-8. (a) The envelope of the pulse intensity $I(t)$ and the time-dependent carrier frequency chirp $\Delta\omega(t)$, and (b) a typical resultant spectrum cause by the effect of SPM.

In the frequency domain, a signal with frequency chirp will also have a phase shift of the Fourier spectrum in frequency, but importantly, it can be shown that

the presence of frequency chirp increases the spectral bandwidth, $\Delta\nu_{ch}$, compared to an unchirped pulse, $\Delta\nu$, while maintaining the same pulse width [23]. A Gaussian pulse with duration, τ_p (measured across the full width half maximum, FWHM), and with linear frequency chirp, has the ratio of the increment of the spectral bandwidth given as

$$\frac{\Delta\nu_{ch}}{\Delta\nu} = \sqrt{1+\left(\frac{b}{a}\right)^2} \tag{1.16}$$

where parameter b is a measure of the chirp and parameter a is related to the duration of the unchirped pulse by:

$$a = 2\ln(2)/\tau_p^{\,2} \tag{1.17}$$

The Fourier theorem tells us that $\Delta\nu\Delta\tau$, the time-bandwidth product is constrained by the uncertainty principle as to the shortest pulses that can be supported by a particular frequency bandwidth. In the case of Gaussian pulses, $\Delta\nu_p\Delta\tau_p \geq 0.44$, where $\Delta\nu_p$ and $\Delta\tau_p$ are measured at their FWHM. Hence, for chirped pulses, the time-bandwidth product is not a minimum and it can be shown that a Gaussian pulse with linear frequency chirp is related to the time-bandwidth product as

$$\Delta\nu_p\Delta\tau_p = 0.44\cdot\sqrt{1+\left(\frac{a}{b}\right)^2} \tag{1.18}$$

For pulses with no chirp, $b=0$, the pulse is said to be "transform limited". In the next section a technique will be described for the control of the dispersion within pulses thus minimising frequency chirp.

1.5 Dispersion compensation

There are several schemes available to compensate for GVD and thus to control dispersion; prism pairs [34], pairs of diffraction gratings [35] and chirped dielectric mirrors [36]. The experiments described in this thesis used pairs of prisms for dispersion compensation. Figure 1-9 illustrates this configuration using four prisms.

The four identical prisms are cut and orientated so that the rays are incident at minimum deviation and Brewster's angle (at that wavelength), to minimise displacement and losses.

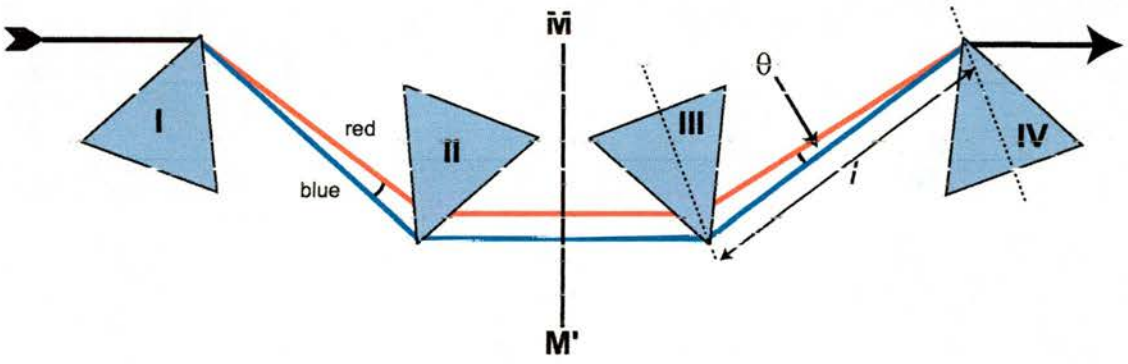

Figure 1-9. A prism sequence that provides a way of introducing GVD that is adjustable through both positive and negative values and introduces low loss.

The output face of prism I is parallel to the input face of prism II. The plane MM' is normal to the exit rays and defines a plane of symmetry for the other two prisms. If a mirror is placed in plane MM', two prisms can act as an effective four-prism arrangement. The total dispersion *D* of the prism sequence is rewritten from equation (1.11) as

$$D = \left(\frac{\lambda}{cL}\right)\frac{\mathrm{d}^2 P}{\mathrm{d}\lambda^2} \qquad (1.19)$$

where, L, is the physical length of the light path, P, is the optical path length. The derivative $d^2P/d\lambda^2$ is a function of the angular divergence, θ, the refractive index of the prism material, n, and the apex separation, l, of the prisms.

$$\frac{dP}{d\lambda^2} = 4l\left\{\left[\frac{d^2n}{d\lambda^2} + \left(2n - \frac{1}{n^3}\right)\left(\frac{dn}{d\lambda}\right)^2\right]\sin(\theta) - 2\left(\frac{dn}{d\lambda}\right)^2\cos(\theta)\right\} \qquad (1.20)$$

It can be shown that for sufficiently large values of, l, the overall dispersion becomes negative. Therefore, by changing the prism positions it is possible to vary the total dispersion of the cavity from positive to negative.

The geometric configuration of the prism pairs can only shorten Ti:sapphire laser pulses to the sub-100 fs regime when third-order dispersion becomes a limiting factor. To achieve yet shorter pulse durations it is necessary to choose a prism medium that has a combined geometric and material contribution to compensate third-order dispersion [7]. Another way of controlling dispersion, without the need of introducing intracavity glass, is by using chirped dielectric mirrors as the source of broadband negative GVD [10,36]. These have been possible since advances in semiconductor growth techniques have permitted the fabrication of Bragg mirror structures with near angstrom precision. These chirped mirrors reflect different wavelengths at different depths depending on the thickness of the Bragg layer, Figure 1-10.

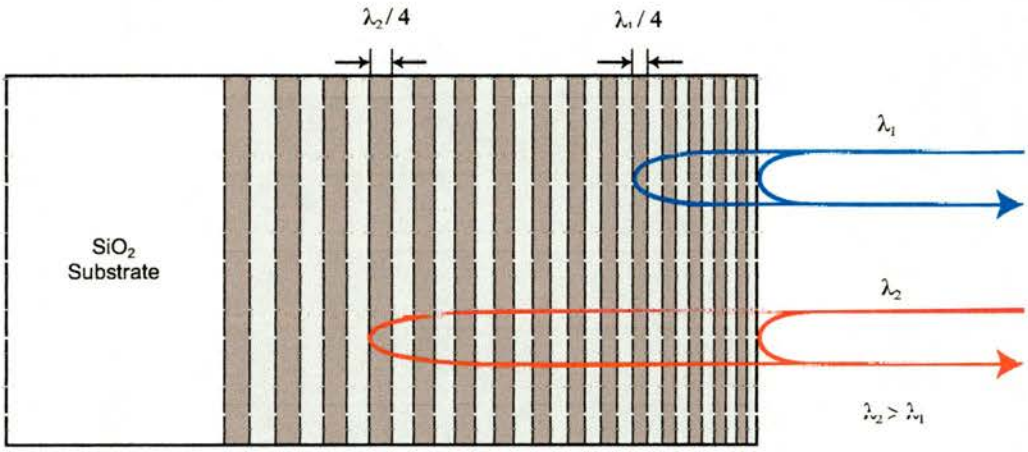

Figure 1-10 Illustration of a chirped TiO/SiO_2 Bragg mirror.

Chirped mirrors offer more exact control over the intracavity dispersion. Double chirped mirrors have been shown to permit compression of cubic phase allowing for better compression over the full lasing bandwidth. Such mirrors have facilitated the generation of sub-5 fs laser pulses [2].

1.6 Conclusions

In this chapter we have traced the history of few-cycle optical pulse generation to the current limit of 1.8 cycles [1] from an amplified laser system. A selection of possible applications of few-cycle pulses were discussed, from broadband spectroscopy in the mid infrared to the coherent quantum control of molecules. Such applications provide the motivation for few-cycle optical pulse research.

The Ti:sapphire laser is one of the most important laser sources in ultrashort pulse research, and was the driving force behind the experiments described in later chapters. Thus, the physical properties of the Ti:sapphire gain medium along with the mechanisms involved to achieve Kerr lens modelocking were examined. The behaviour of the resulting ultrashort pulses when propagating through linear and nonlinear media was also described.

The short pulse duration and high peak powers obtained from the Ti:sapphire laser are ideal as a pump source for optical parametric oscillators. The next chapter describes such devices and the concepts behind nonlinear optics.

1.7 References

1 A. Baltuska, Z. Y. Wei, M. S. Pshenichnikov, and D. A. Wiersma, "*Optical pulse compression to 5 fs at a 1-MHz repetition rate*", Optics Letters **22,** 102-104 (1997).

2 M. Nisoli, S. DeSilvestri, O. Svelto, R. Szipocs *et al.*, "*Compression of high-energy laser pulses below 5 fs*", Optics Letters **22,** 522-524 (1997).

3 W. H. Knox, R. L. Fork, M. C. Downer, R. H. Stolen *et al.*, "*Optical Pulse-Compression to 8 Fs at a 5-Khz Repetition Rate*", Applied Physics Letters **46,** 1120-1121 (1985).

4 R. L. Fork, C. H. B. Cruz, P. C. Becker, and C. V. Shank, "*Compression of Optical Pulses to 6 Femtoseconds By Using Cubic Phase Compensation*", Optics Letters **12,** 483-485 (1987).

5 F. M. Mitschke and L. F. Mollenauer, "*Ultrashort Pulses from the Soliton Laser*", Optics Letters **12,** 407-409 (1987).

6 A. S. Gouveianeto, A. S. L. Gomes, and J. R. Taylor, "*Pulses of 4 Optical Cycles from an Optimized Optical Fiber Grating Pair Soliton Pulse Compressor at 1.32-Mu-M*", Journal of Modern Optics **35,** 7-10 (1988).

7 C. P. Huang, M. T. Asaki, S. Backus, M. M. Murnane *et al.*, "*17-Fs Pulses From a Self-Mode-Locked Ti-Sapphire Laser*", Optics Letters **17,** 1289-1291 (1992).

8 P. F. Curley, C. Spielmann, T. Brabec, F. Krausz *et al.*, "*Operation of a Femtosecond Ti-Sapphire Solitary Laser in the Vicinity of Zero Group-Delay Dispersion*", Optics Letters **18,** 54-56 (1993).

9 I. P. Christov, M. M. Murnane, H. C. Kapteyn, J. P. Zhou *et al.*, "*4th-Order Dispersion-Limited Solitary Pulses*", Optics Letters **19,** 1465-1467 (1994).

10 A. Stingl, C. Spielmann, F. Krausz, and R. Szipocs, "*Generation of 11-Fs Pulses From a Ti-Sapphire Laser Without the Use of Prisms*", Optics Letters **19,** 204-206 (1994).

11 A. Stingl, M. Lenzner, C. Spielmann, F. Krausz *et al.*, "*Sub-1o-Fs Mirror-Dispersion-Controlled Ti-Sapphire Laser*", Optics Letters **20,** 602-604 (1995).

12 L. Xu, C. Spielmann, F. Krausz, and R. Szipocs, "*Ultrabroadband ring oscillator for sub-10-fs pulse generation*", Optics Letters **21,** 1259-1261 (1996).

13 I. D. Jung, F. X. Kartner, N. Matuschek, D. H. Sutter *et al.*, "*Self-starting 6.5-fs pulses from a Ti:Sapphire laser*", Optics Letters **22,** 1009-1011 (1997).

14 A. Nahata, D. H. Auston, C. J. Wu, and J. T. Yardley, "*Generation of Terahertz Radiation from a Poled Polymer*", Applied Physics Letters **67,** 1358-1360 (1995).

15 T. Beddard, M. Ebrahimzadeh, T. D. Reid, and W. Sibbett, "*Five-optical-cycle pulse generation in the mid infrared from an optical parametric oscillator based on aperiodically poled lithium niobate*", Optics Letters **25,** 1052-1054 (2000).

16 M. Freyberger, P. Bardroff, C. Leichtle, G. Schrade *et al.*, "*The art of measuring quantum states*", Physics World **10,** 41-45 (1997).

17 J. C. Diels, *Ultrashort laser pulse phenomena : fundamentals, techniques, and applications on a femtosecond time scale* (Academic Press, 1996).

18 L. Xu, C. Spielmann, A. Poppe, T. Brabec *et al.*, "*Route to phase control of ultrashort light pulses*", Optics Letters **21,** 2008-2010 (1996).

19 P. F. Moulton, Optics News **8,** 9 (1982).

20 P. F. Moulton, "*Spectroscopic and Laser Characteristics of Ti-Al2o3*", Journal of the Optical Society of America B-Optical Physics **3,** 125-133 (1986).

21 T. R. Steele, D. C. Gerstenberger, A. Drobshoff, and R. W. Wallace, "*Broadly Tunable High-Power Operation of an All-Solid-State Titanium-Doped Sapphire Laser System*", Optics Letters **16,** 399-401 (1991).

22 Spectra-Physics Lasers Inc, (1335 Terra Bella Avenue, Mountain View, CA. 94043, USA).

23 A. E. Siegmann, (*University Science Books, California*, 1996).

24 S. E. Schwarz and T. Y. Tan, "*Wave interactions in saturable absorbers*", Applied Physics Letters **10,** 4 (1967).

25 A. J. DeMaria and H. H. Stetser, "*Self mode-locking of a laser with saturable absorbers*", Applied Physics Letters **8,** 174 (1966).

26 H. Mockner and R. J. Collins, "*Mode competition and self-locking effects in a Q-switched ruby laser*", Applied Physics Letters **7,** 270 (1965).

27 D. E. Spence, J. M. Evans, W. E. Sleat, and W. Sibbett, "*Regeneratively Initiated Self-Mode-Locked Ti-Sapphire Laser*", Optics Letters **16,** 1762-1764 (1991).

28 D. E. Spence, P. N. Kean, and W. Sibbett, "*60-Fsec Pulse Generation From a Self-Mode-Locked Ti-Sapphire Laser*", Optics Letters **16,** 42-44 (1991).

29 R. W. Boyd, *Nonlinear Optics* (Academic Press Inc. (California, USA), 1992).

30 M. Piche and F. Salin, "*Self-Mode Locking of Solid-State Lasers Without Apertures*", Optics Letters **18,** 1041-1043 (1993).

31 G. Cerullo, S. Desilvestri, and V. Magni, "*Self-Starting Kerr-Lens Mode-Locking of a Ti-Sapphire Laser*", Optics Letters **19,** 1040-1042 (1994).

32 N. H. Rizvi, P. M. W. French, and J. R. Taylor, "*Continuously Self-Mode-Locked Ti-Sapphire Laser That Produces Sub-50-Fs Pulses*", Optics Letters **17,** 279-281 (1992).

33 I. D. Jung, F. X. Kartner, N. Matuschek, D. H. Sutter *et al.*, "*Semiconductor saturable absorber mirrors supporting sub-10-fs pulses*", Applied Physics B-Lasers and Optics **65,** 137-150 (1997).

34 R. L. Fork, O. E. Martinez, and J. P. Gordon, "*Negative Dispersion Using Pairs of Prisms*", Optics Letters **9,** 150-152 (1984).

35 E. B. Treacy, "*Optical pulse compression with diffraction gratings*", IEEE Journal Quantum Electronics **5,** 454 (1969).

36 R. Szipocs, K. Ferencz, C. Spielmann, and F. Krausz, "*Chirped Multilayer Coatings For Broad-Band Dispersion Control in Femtosecond Lasers*", Optics Letters **19,** 201-203 (1994).

Chapter 2

Optical Parametric Oscillators and Nonlinear Optics

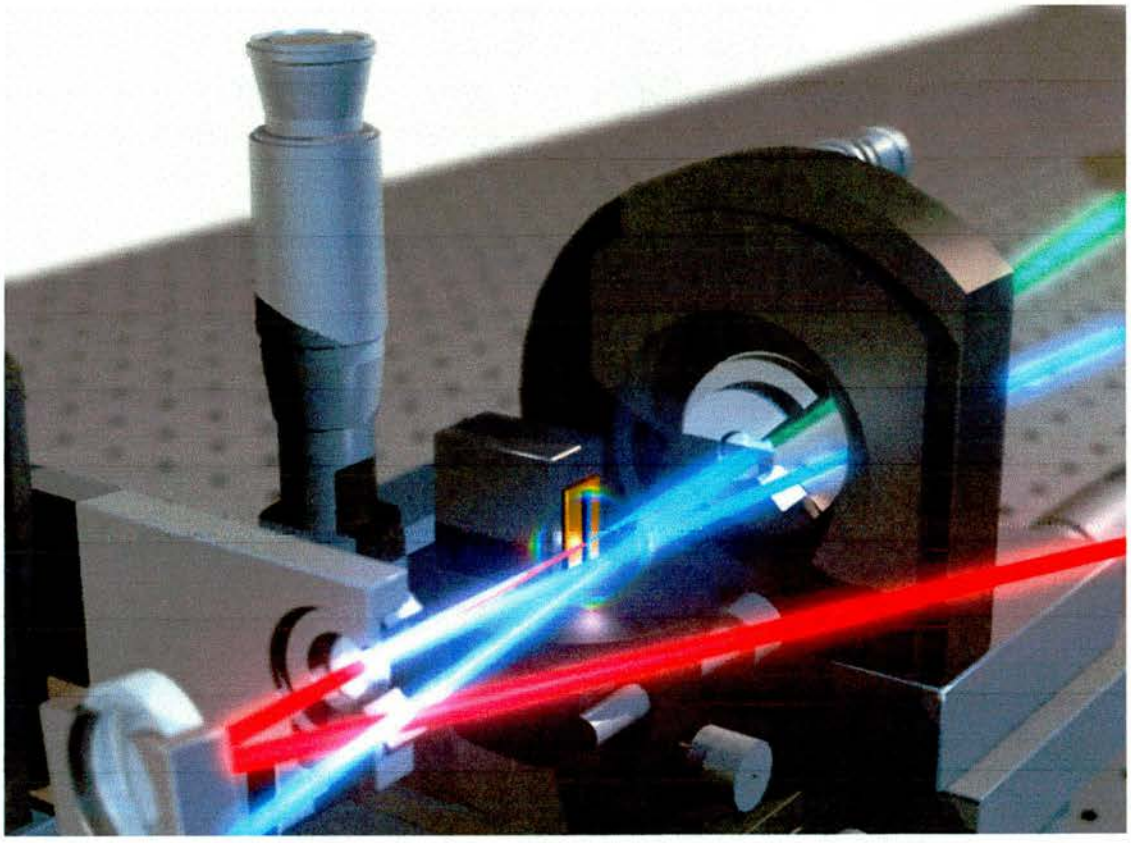

Artistic visualisation of the head of an optical parametric oscillator.

2 Femtosecond Optical Parametric Oscillators

Since the invention of the laser, a major area of research in laser physics has been in the development of complementary optical sources capable of producing coherent radiation that are continuously tunable over a broader wavelength range than lasers. In gain media such as Ti:sapphire crystals, the quantised levels are sufficiently broadened to form continuous bands, so that wavelength tunable emission can result from transitions between these bands. While conventional tunable lasers are highly effective in producing coherent radiation in different spectral regions, the tuning range of these systems is often limited. Moreover, for most broadly tunable lasers (with the exception of colour-centre lasers and mid-infrared diode lasers), the wavelength coverage is mainly around the visible spectrum.

The potential of nonlinear optical mixing techniques as a means for producing coherent radiation at new wavelengths was first realised over three decades ago. The existence of substantial nonlinearities, first demonstrated by the second harmonic generation of light in quartz, started research in the area of nonlinear optics. Soon after, the importance of the optical parametric process as a powerful tool for the generation of widely tunable radiation was recognised. Giordmaine and Miller reported the first demonstration of a tunable optical parametric oscillator (OPO) in 1965 [1]. The key attractions of OPOs are their exceptionally broad tuning ranges (typically several hundred nanometres) and their ability to cover wavelength regions not directly accessible by conventional tunable lasers.

2.1 Nonlinear polarisation

Significant nonlinear optical phenomena arise when some materials are subject to intense electromagnetic radiation. Consider a transparent dielectric material in the presence of an electromagnetic field. In a classical model, the field causes a displacement of the electrons within the material with respect to the nuclei, which causes an overall polarisation within the dielectric. The polarisation (the electric dipole moment per unit volume) responds linearly to the incident radiation if the field strength is low. The low field relationship describes the area of linear optics as mentioned in Chapter 1 and is governed by:

$$\mathbf{P} = \varepsilon_0 \chi^{(1)} \mathbf{E} \tag{2.1}$$

where $\mathbf{P}$ is the polarisation field vector, $\mathbf{E}$ is the electromagnetic field vector, and ε_0 is the permittivity of free space. The term, $\chi^{(1)}$, is the linear susceptibility of the material which gives rise to the linear optical effects such as refractive index, dispersion and birefringence and is generally dependent on the frequency, ω, of the optical radiation. In a crystal, the linear susceptibility is a tensor, which obeys the symmetry properties of the medium.

When the applied field strength is comparable to the inter-atomic electric field within the dielectric (as with laser radiation), the induced polarisation is nonlinearly related to the field strength such that:

$$\mathbf{P} = \varepsilon_0 \left[\chi^{(1)} \mathbf{E} + \chi^{(2)} \mathbf{E}^2 + \chi^{(3)} \mathbf{E}^3 + \ldots \right] \tag{2.2}$$

where $\chi^{(i)}$ is a tensor describing the nonlinear susceptibilities of the medium. This is the regime of *nonlinear optics*. The magnitudes of the tensor

components $\chi^{(i)}$, decrease rapidly with increasing i ($\chi^{(1)} : \chi^{(2)} : \chi^{(3)} \sim 1 : 10^{-8} : 10^{-16}$). It is not surprising therefore, that the exploration of many nonlinear effects was not possible until the invention of the laser.

Almost all linear and nonlinear effects of practical importance can be described by the first three terms of Equation (2.2). The second term $\chi^{(2)}$, gives rise to second harmonic generation, sum- and difference-frequency mixing and parametric generation. This quantity, referred to as the second-order nonlinear susceptibility (or chi 2), is non-zero only in *non-centrosymmetric* media. The third term, $\chi^{(3)}$, is responsible for cubic nonlinear effects such as third harmonic generation and the optical Kerr effect.

2.1.1 Propagation of waves in nonlinear media

By considering the propagation of waves within a non-centrosymmetric nonlinear medium, it is possible to derive the equations governing parametric interactions. First, consider Maxwell's wave equation for a non-absorbing dielectric medium containing no free charge:

$$\nabla^2 E = \mu_0 \varepsilon_0 \frac{\partial^2 E}{\partial t^2} + \mu_0 \frac{\partial^2 P}{\partial t^2} \tag{2.3}$$

where ε_0 and μ_0 are the electric permittivity and the magnetic permeability in the vacuum, respectively. The total polarisation of the medium, P given in Equation (2.2), can be written as the sum of linear and nonlinear components:

$$P_L = \varepsilon_0 \chi^{(1)} E \tag{2.4}$$

$$P_{NL} = \varepsilon_0 \left[\chi^{(2)} E^2 + \chi^{(3)} E^3 + ... \right] \tag{2.5}$$

As we are interested in the nonlinear polarisation term, we shall be looking for solutions to Maxwell's equation (2.3), with P_{NL} as the source term. Substituting Equations (2.4) & (2.5) into Equation (2.3) produces a wave equation in terms of P_{NL}, and assuming that $\chi^{(1)}$ is time-independent (i.e. no dispersion), we obtain

$$\nabla^2 E = \mu_0 \varepsilon \frac{\partial^2 E}{\partial t^2} + \mu_0 \frac{\partial^2 P_{NL}}{\partial t^2} \tag{2.6}$$

where $\varepsilon = \varepsilon_0 \left(1 + \chi^{(1)}\right)$. This is the wave equation describing the propagation of electromagnetic fields in nonlinear media. The terms higher than $\chi^{(2)}$ in Equation (2.5) will be ignored since we are interested in second-order nonlinear effects, so P_{NL} is written as:

$$P_{NL} \sim \varepsilon_0 \chi^{(2)} E^2 \tag{2.7}$$

To simplify the expression, we will assume that the electromagnetic waves are only travelling collinearly in the z-direction. Substituting for P_{NL} in Equation (2.6) we obtain the wave equation for second order nonlinear processes:

$$\frac{\partial^2 E}{\partial z^2} = \mu_0 \varepsilon \frac{\partial^2 E}{\partial t^2} + \mu_0 \frac{\partial^2}{\partial t^2} \left(\varepsilon_0 \chi^{(2)} E^2 \right) \tag{2.8}$$

The solution of this equation determines the behaviour of the light as it propagates through the dielectric medium.

2.1.2 Nonlinear Crystals

Crystalline materials fall into one of 32 structural categories, known as point groups. The different structures have differing degrees of symmetry, which in turn is responsible for a number of different properties of the material. These properties render the materials as either piezoelectric, pyroelectric or ferroelectric. The lowest level of symmetry divides all crystals into two groups, those that are centrosymmetric and those that are not. As with linear susceptibility, the tensor coefficients of the second order nonlinear susceptibility must reflect the symmetry properties of the crystal. A consequence of this is that in centrosymmetric media the second-order nonlinear coefficient must vanish. Thus, second-order nonlinear processes, such as optical parametric generation, are restricted to non-centrosymmetric materials [2]. Of the 32 point groups, 21 are non-centrosymmetric [3].

The susceptibility coefficients $\chi^{(n)}$ are tensors of rank (n+1), thus the second-order nonlinear susceptibility, $\chi^{(2)}$ is a third-rank tensor with 27 components, χ_{ijk}. The second order nonlinear polarisation field can be expressed in terms of the i, j and k indices as:

$$\mathbf{P}_i(t) = \sum_{i,j,k} \varepsilon_0 \chi_{ijk}^{(2)} \mathbf{E}_j(t) \mathbf{E}_k(t) \tag{2.9}$$

As well as crystal symmetry restrictions, $\chi_{ijk}^{(2)}$ satisfies two other symmetry conditions. The first is an intrinsic symmetry relation derived from equations for conservation of energy and momentum for a lossless medium. It states that $\chi_{ijk}^{(2)}(-\omega_3, \omega_2, \omega_1)$ is invariant under any combination of the j and k indices [4]. The second symmetry relation is the Kleinman's conjecture [5], which states that the

$\chi^{(2)}_{ijk}$ coefficients that are related by a rearrangement of the subscripts (i, j, k) are in fact equal.

One way of discussing the nonlinearity of a material is in terms of the piezoelectric tensor, d_{ijk}, which has elements:

$$d_{ijk} = \frac{\chi_{ijk}}{2} \tag{2.10}$$

There is no physical distinction between the subscripts j and k, so that $d_{ijk} = d_{ikj}$. Therefore, the tensor can be replaced by a 3 x 6 element matrix, of nonlinear components, d_{ij}. The resulting matrix has the same form for all members of a particular crystal class. It relates the components of polarisation and electric fields, and note that due to the Kleinman conjecture, there are only 10 unique elements in the matrix:

$$\begin{bmatrix} P_x \\ P_y \\ P_z \end{bmatrix} = \begin{bmatrix} d_{11} & d_{12} & d_{13} & d_{14} & d_{15} & d_{16} \\ d_{16} & d_{12} & d_{23} & d_{24} & d_{14} & d_{12} \\ d_{15} & d_{24} & d_{33} & d_{23} & d_{13} & d_{14} \end{bmatrix} \begin{bmatrix} E_x^2 \\ E_y^2 \\ E_z^2 \\ 2E_zE_y \\ 2E_zE_x \\ 2E_xE_y \end{bmatrix} \tag{2.11}$$

The d_{ij} coefficients can be used to calculate an *effective nonlinear coefficient*, d_{eff}, via equations which depend on the crystal class [3,6,7]. The expression for the polarisation originally shown in Equation (2.9), can now be rewritten for one frequency component as:

$$P(\omega_3) = 2\varepsilon_0 d_{eff} E(\omega_1) E(\omega_2) \tag{2.12}$$

2.1.3 Coupled wave equations

The coupled wave equations describe the phase relationships governing the direction of energy flow between any three interacting waves. In the case of parametric generation we are concerned with the interaction of three harmonic waves at frequencies ω_1, ω_2 and ω_3, which are related to each other so that energy is conserved, i.e. $\omega_3 = \omega_2 + \omega_1$. To simplify analysis, the three fields are considered as infinite uniform plane waves and the effects of double refraction and focusing are ignored. The total instantaneous field is of the form

$$\mathbf{E}(z,t) = \mathbf{E}_1(z,t) + \mathbf{E}_2(z,t) + \mathbf{E}_3(z,t) \tag{2.13}$$

Each component has a temporal dependence of

$$\mathbf{E}_j(z,t) = \tfrac{1}{2}\left[\mathbf{E}_j(z)\mathrm{e}^{i(k_j z-\omega t)} + c.c\right] \tag{2.14}$$

where k_j is the wave vector of wave j. The real electric field $\mathbf{E}_j(z,t)$ (which is the quantity involved in the wave equation) is expressed in terms of the complex amplitude $\mathbf{E}_j(z)$, which in itself is given by:

$$\mathbf{E}_j(z) = \left|\mathbf{E}_j(z)\right| e^{i\phi_j} \qquad j = 1,2,3 \tag{2.15}$$

with $\left|\mathbf{E}_j(z)\right|$ as the real field amplitude. Since the waves at the three different frequencies are interchanging energy through $\chi^{(2)}$ as they propagate through the medium, their respective amplitudes will vary with position. Hence, the complex field is expressed as a function of z.

When Equation (2.13) is substituted using Equation (2.14), into the wave equation (2.8), the resulting equation can be split into three parts, each of which describe the behaviour of one of the waves. Assuming that the complex field amplitudes $\mathbf{E}_j(z)$ are all time-independent and the field amplitudes vary slowly

over distances compared to a wavelength, the solutions of the wave equation (2.8) can be written as:

$$\frac{\mathrm{d}\mathbf{E}_1(z)}{\mathrm{d}z} = -\frac{i\omega_1}{2}\sqrt{\frac{\mu}{\varepsilon_1}}\chi^{(2)}_{(\omega_1=\omega_3-\omega_2)}\mathbf{E}_3(z)\mathbf{E}_2^*(z)\mathrm{e}^{i\Delta kz} \tag{2.16}$$

$$\frac{\mathrm{d}\mathbf{E}_2(z)}{\mathrm{d}z} = -\frac{i\omega_2}{2}\sqrt{\frac{\mu}{\varepsilon_1}}\chi^{(2)}_{(\omega_2=\omega_3-\omega_1)}\mathbf{E}_3(z)\mathbf{E}_1^*(z)\mathrm{e}^{i\Delta kz} \tag{2.17}$$

$$\frac{\mathrm{d}\mathbf{E}_3(z)}{\mathrm{d}z} = -\frac{i\omega_3}{2}\sqrt{\frac{\mu}{\varepsilon_1}}\chi^{(2)}_{(\omega_3=\omega_2-\omega_1)}\mathbf{E}_2(z)\mathbf{E}_1^*(z)\mathrm{e}^{i\Delta kz} \tag{2.18}$$

These equations are commonly referred to as *coupled wave equations*. In each case $\chi^{(2)}$ describes the interaction of the other waves in generating the resulting wave [7-11]. The quantity Δk in each of the equations above is the *wave vector mismatch* and is written as

$$\Delta k = k_3 - k_2 - k_1 \tag{2.19}$$

The value of each momentum vector k_j is defined by:

$$k_j = \frac{n_j\omega_j}{c} = \frac{2\pi n_j}{\lambda_j} \tag{2.20}$$

There are an infinite number of ways in which ω_1, ω_2 and ω_3 can interact during propagation through a nonlinear medium. However, gain will only occur with interactions that have the correct phase relationship to undergo constructive interference. This will happen when the condition $\Delta k = 0$, known as phase matching, is satisfied. Phase matching is described in more detail in Section 2.2.

The three-wave mixing process can be viewed physically in terms of the distortion of the electron charge clouds in the medium, driven by the optical

fields, ω_3, ω_2 and ω_1. These distortions lead to an oscillating polarisation at any combination of the frequencies, which in turn radiates optical waves at the corresponding frequencies. The direction of power flow amongst the interacting fields depends on the initial amplitude of the optical fields at the input to the medium and their relative phase $\phi = \phi_3 - \phi_2 - \phi_1$. In the parametric generation process, the optimum relative phase is given by $\phi = \phi_3 - \phi_2 - \phi_1 = -\pi/2$ where $\Delta k = 0$ and the pump field at ω_3 is greatly depleted. Under this condition, the generated fields ω_1 and ω_2 experience maximum growth while depleting the pump field ω_3 during its propagation through the medium.

The coupled wave equations can be solved to obtain equations that describe parametric gain and amplification in a nonlinear medium. Assuming the power drained from the pump, ω_3, by the signal and idler waves is small, i.e. the pump wave maintains constant amplitude throughout the interaction region, then Equation (2.16) and the conjugate of Equation (2.17) can be solved as a pair of coupled linear differential equations. Thus, it can be shown that in the limit of small gain, the generated waves ω_1 & ω_2 are amplified by a gain [12] given by:

$$G_I(\omega_1,\omega_2) = \frac{I_I(\omega_1,\omega_2)}{I_0(\omega_1,\omega_2)} - 1 \cong \frac{2\pi^2\omega_1\omega_2\mu_0 d_{eff}^2 l^2}{n_1 n_2 n_3 c} I_0(\omega_3)\,\mathrm{sinc}^2\left(\frac{\Delta kl}{2}\right) \qquad (2.21)$$

It is clear that the optical parametric gain has a $\mathrm{sinc}^2(x)$ dependence on Δkl and that the efficiency is proportional to d_{eff}^2 and l^2. Therefore, the maximum gain from the parametric generator is available when $\Delta k = 0$ and phasematching is achieved.

2.1.4 Manley-Rowe Relations

Examining the three-coupled wave equations in more detail, shows that Equation (2.17) can be obtained from Equation (2.16) by interchanging $\mathbf{E}_1$ and $\mathbf{E}_2$, but Equation (2.18) can not be obtained by a similar exchange. The significance of this statement becomes apparent when looking at the power flow in the interaction. If perfect phasematching is assumed ($\Delta k = 0$), then after some algebraic manipulation [2] it is possible to equate the three relations (2.16) - (2.18) to find

$$\frac{1}{\omega_1}\frac{dI_1}{dz} = \frac{1}{\omega_2}\frac{dI_2}{dz} = -\frac{1}{\omega_3}\frac{dI_3}{dz} \tag{2.22}$$

where the derivatives dI_i/dz are the change in power of the source at ω_i. This relation was first formulated by Manley & Rowe and has significant consequences. For the case of sum-frequency generation between two beams of frequencies ω_1 and ω_2, the Manley-Rowe relation states that both beams will lose power, which is gained by the sum-frequency $\omega_3 = \omega_1 + \omega_2$. But for the case of difference-frequency generation $\omega_3 - \omega_2 = \omega_1$, the relation says that the source at ω_3 loses power not only to the generated frequency ω_1, but to the source of ω_2 *as well.*

Since during difference-frequency generation the source of ω_2 gains power, there is the possibility of generating the difference-frequency between a strong source at ω_3 (pump), and a much weaker source ω_2. If the weak signal at ω_2 is passed through a nonlinear crystal repeatedly, then it will gain in power with every pass; as a consequence, the signal at ω_1 will also grow. The key point is that the weak signal at ω_2 does not have to be introduced from outside, it can

be a frequency within the noise spectrum. The many passes can be obtained by putting the crystal in a cavity resonant at ω_2, and if the single pass gain overcomes the losses then such a system will oscillate. This is the basis of an optical parametric oscillator. By convention, the waves are given names according to their wavelength. The shortest wavelength is the *pump*, $\omega_p(\omega_3)$, which generates two longer wavelengths, the shorter of which is the *signal*, $\omega_s(\omega_1)$, and the longer is the *idler*, $\omega_i(\omega_2)$. If ω_1 and ω_2 are equal then the process is said to be degenerate. The condition of energy conservation between three waves undergoing optical parametric generation is now written as:

$$\omega_p = \omega_s + \omega_i \tag{2.23}$$

2.2 Phase matching

As mentioned previously in Equation (2.19), $\Delta\mathbf{k} = \mathbf{k}_p - \mathbf{k}_s - \mathbf{k}_i$ which requires that $\Delta\mathbf{k} = 0$ for maximum gain of the second-order nonlinear interaction. This phase vector mismatch can be expressed in terms of the refractive indices, using Equation (2.20), for ideal phasematching:

$$\frac{1}{c}(n_3\omega_3 - n_1\omega_1 - n_2\omega_2) = 0 \tag{2.24}$$

This equation represents the conservation of photon momentum and must be satisfied for phasematching. The other restriction is the conservation of energy, given that $\omega = 2\pi\nu$ and $c = \nu\lambda$, Equation (2.23) then becomes:

$$\frac{1}{\lambda_p} - \frac{1}{\lambda_s} - \frac{1}{\lambda_i} = 0 \tag{2.25}$$

Both Equations (2.24) and (2.25) above must be simultaneously satisfied for macroscopic amplification to occur in a three wave mixing process. Phasematching can be achieved either collinearly or noncollinearly, where the wave-vectors are arranged as shown below:

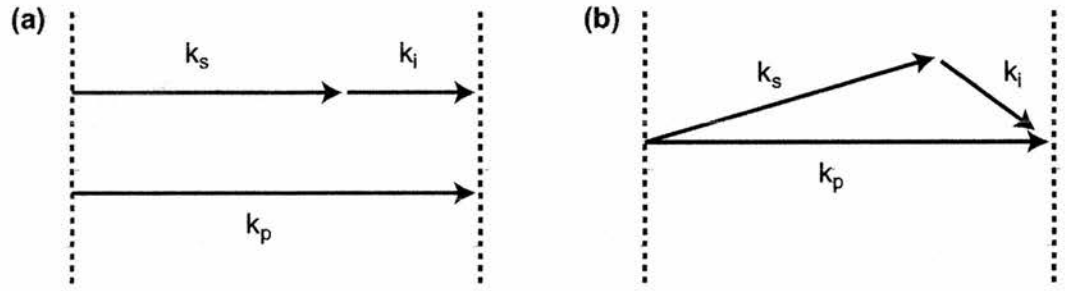

Figure 2-1 Wavevector arrangement for (a) collinear and (b) non-collinear phasematching.

During propagation through the nonlinear crystal, the three waves are subject to material dispersion, which leads to an increase in Δk so the different waves generated travel at different velocities. The result of this is that the interacting fields gradually become out of step and lose their relative optimum phase. The waves will convert to other wavelengths and then are converted back, until such a time that the phase relation favours forward conversion once again, and the process repeats itself. Over the crystal length the overall conversion to new wavelengths is negligible and no useful light is generated. This is illustrated in Figure 2-4. The material dispersion sets an upper limit on the maximum interaction length useful for parametric generation. This is called the *coherence length*, l_c, which is defined as the interaction length over which, due to dispersion, the parametric gain is reduced by half of its peak value at $\Delta k = 0$. This distance corresponds to a relative phase change of the waves of π, and is given by:

$$l_c = \frac{\pi}{\Delta k} \tag{2.26}$$

Typical values of the coherence length in non-birefringent crystals are of the order 10 μm, but a crystal length this short will produce negligible optical gain! Thus, with isotropic crystals the phasematching condition will never be fulfilled because of normal dispersion. However, high conversion efficiencies can be obtained by exploiting some material properties of nonlinear crystals as described in the following sub-sections.

2.2.1 Birefringent phase matching

The first method for achieving the phasematching condition, $\Delta k = 0$, exploits the birefringence of optically anisotropic materials to offset dispersion. In such materials, the index of refraction of a wave depends on the direction of propagation through the media, its state of polarisation as well as its frequency. Therefore, by careful choice of polarisation states and crystal orientation, it is possible to maintain phase matching at every point along a direction of propagation throughout the crystal for a particular combination of frequencies $(\omega_3, \omega_2, \omega_1)$. This condition means that the coherence length, l_c becomes infinite and the maximum useful interaction length is only limited by the physical length of the crystal.

Birefringent materials are classified as either positive or negative *uniaxial* or *biaxial* crystals. The optical characteristics of such crystals are often described in terms of a three-dimensional index surface called the *optical indicatrix,* see Figure 2-2. In uniaxial crystals $n_x = n_y \neq n_z$ so the optical indicatrix is a prolate ellipsoid about the z-axis if positive and oblate if the crystal is negative uniaxial.

In biaxial crystals, the indicatrix is a general ellipsoid with three unequal axes as n_x, n_y, n_z are all different. The plane containing the z axis and the wave vector, $\mathbf{k}$, of the light wave is termed the *principal plane*. The light beam whose polarisation is normal to the principal plane is called the *ordinary wave* or *o-wave*. The light wave propagating with the orthogonal polarisation at an angle θ to an axis, will experience a value of refractive index dependent on that angle, is called the *extraordinary wave* or *e-wave*. In this way, the phasematching condition can be satisfied for a suitable choice of polarisations and propagation angles for the incident light where $n_0 = n_e$ so the photons will travel at the same speed, hence the interaction length is long.

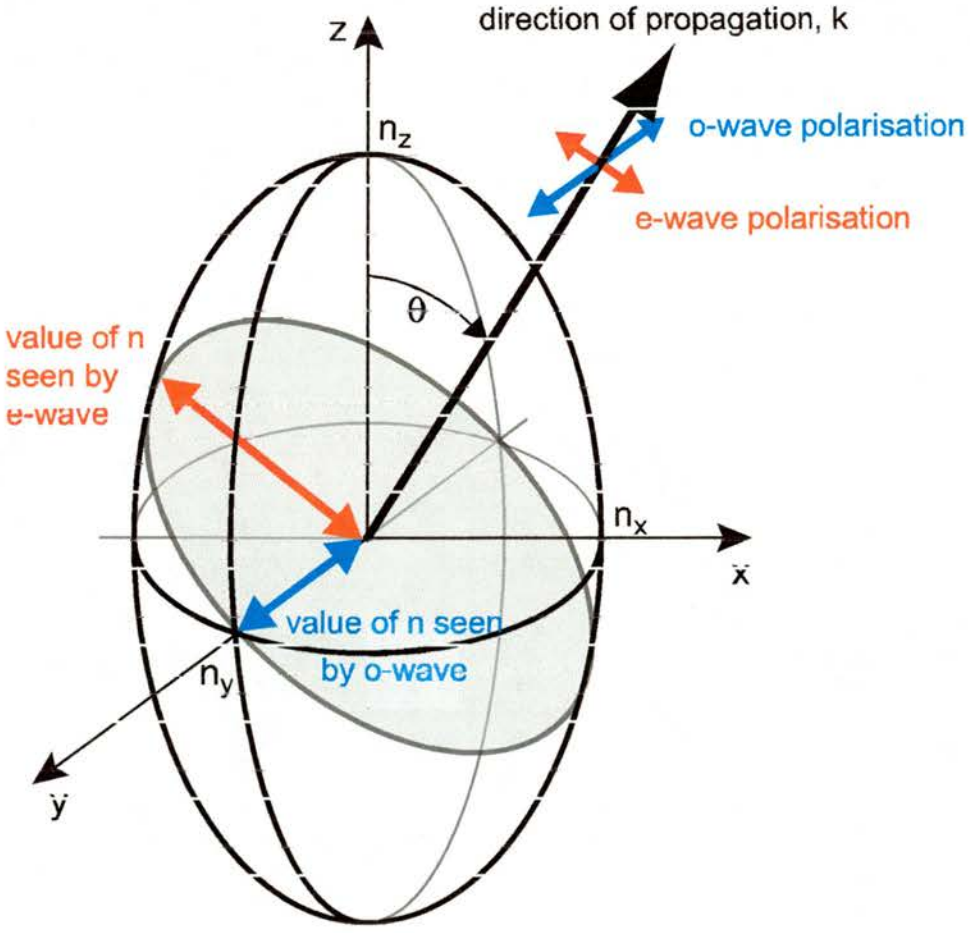

Figure 2-2. Optical indicatrix showing the refractive indices for the o and e-waves on propagation through a birefringent crystal at angle θ to the optic axis In this case $n_x = n_y \equiv n_0$ and $n_z \equiv n_e > n_o$ so the crystal is positive uniaxial.

It is customary to define the principal axes of the indicatrix in terms of the *ordinary* index n_o (instead of n_x or n_y) and *extraordinary* index n_e (instead of n_z). Uniaxial crystals have a unique direction along which all allowed polarisation states experience the same refractive index. This is known as the *optic* axis and in uniaxial crystals is coincident with the principal axis, z, of the indicatrix (when θ = 0 in Figure 2-2). Uniaxial crystals are defined as being positive, when $n_e > n_o$, or negative when $n_e < n_o$. Biaxial crystals have two optic axes that generally lie in different directions from the principal axis of the indicatrix. The refractive indices have distinct values and relate to each other as either $n_x > n_y > n_z$ or $n_x < n_y < n_z$.

In general, there are two distinct types of phase-matching, referred to as *type-I* (or parallel) and *type-II* (or orthogonal) phase-matching. In type-I phase-matching, the polarisation vectors of the generated waves at ω_1 and ω_2 are parallel (and orthogonal to that at of the pump at ω_3). Whereas the type-II process the polarisation vectors at ω_1 and ω_2 are perpendicular (with the pump polarisation being parallel to one of the generated waves). When the propagation direction is along one of the principal axes of the indicatrix, the phase-matching is termed *noncritical*, while for any other direction it is referred to as *critical* phase-matching. With optical parametric generation in both positive and negative uniaxial crystals, the type of phasematching involves the combinations of the polarisations shown in Table 1.

	Type I $(\lambda_3 \rightarrow \lambda_1 + \lambda_2)$	Type II $(\lambda_3 \rightarrow \lambda_1 + \lambda_2)$
Positive	$o \rightarrow e+e$	$o \rightarrow e+o$ $o \rightarrow o+e$
Negative	$e \rightarrow o+o$	$e \rightarrow o+e$ $e \rightarrow e+o$

Table 1 Combination of wave polarisations used depending on the type of phasematching, where $\lambda_3 < \lambda_2 < \lambda_1$.

In practice, the attainment of perfect phase-matching is not possible because of the finite frequency spectrum and spatial divergence of the light beams involved in three-wave interaction. The increase in the magnitude of Δk arising from the finite bandwidth of the coupled waves can be measured in terms of $\partial(\Delta k)/\partial\omega$, which is then used to obtain the *spectral acceptance bandwidth* of the crystal by confining the phase mismatch to within the full-width half-maximum of the parametric gain curve, $|\Delta kl| \cong 2\pi$. A typical value of the spectral acceptance bandwidth for a 1 mm Type I KDP crystal is 5.6 nm [13].

Phase-matching is also sensitive to angular deviations and can be determined in the same way by evaluating $\partial(\Delta k)/\partial\theta$. Together, with the condition $|\Delta kl| \cong 2\pi$, this defines the *angular acceptance bandwidth* of the crystal in the θ-direction. Which, for the same KDP crystal, is 5.3 mrad [13].

The variation of refractive index with wavelength can be described by the experimentally obtained Sellmeier equations for the particular crystal [3,14,15]. The phase matching condition of Equation (2.24) can now be rewritten using the Sellmeier equations. By also considering the angular variation of the refractive

index, it is possible to determine the angle required by the incident pump light of given wavelength to generate specific signal and idler wavelengths.

The configuration shown in Figure 2-2 has an angular variation of n_e defined by:

$$n_e(\theta) = n_o \sqrt{\frac{1+\tan^2(\theta)}{1+\left(\frac{n_0}{n_e}\right)^2 \tan^2(\theta)}} \tag{2.27}$$

This makes it possible to angle tune the output of an OPO by slowly turning the crystal so that the pump beam experiences a slowly varying refractive index. The phasematching condition still holds, provided the angular acceptance bandwidth is not exceeded, as the signal and idler wavelengths change to maintain phase-matching.

Phase-matching can also be sensitive to the variations in refractive indices through changes in the crystal temperature. This can also be used to tune the OPO output. The sensitivity can be similarly determined from the expression $\partial(\Delta k)/\partial T$, which defines the *temperature acceptance bandwidth* for the particular phase-matching geometry.

Spatial walk-off

In addition to the phase-mismatch issues described previously, spatial and temporal walk-off play an important role in the operating efficiency of optical parametric oscillators. From Equation (2.21), it is clear that the magnitude of gain in the parametric amplifier is strongly dependent on the interaction length l^2. Even in the presence of perfect phase-matching, walk-off effects can severely limit the maximum useful interaction length, resulting in limitations of the nonlinear gain. Such effects are a result of the reduction in spatial or

temporal overlap of the interacting beams as they propagate through the nonlinear crystal.

Spatial walk-off arises when the propagation of the wave phase vector ($\mathbf{k}$) does not coincide with that of the wave energy vector ($\mathbf{S}$). As the extraordinary wave propagates in a crystal, its power flow direction differs by the *double refraction angle* ρ from its phase velocity direction. This effect, referred to as a Poynting vector walk-off, leads to walk-away of the beam energy $\mathbf{S}$ at an angle ρ from the momentum vector $\mathbf{k}$ - see Figure 2-3.

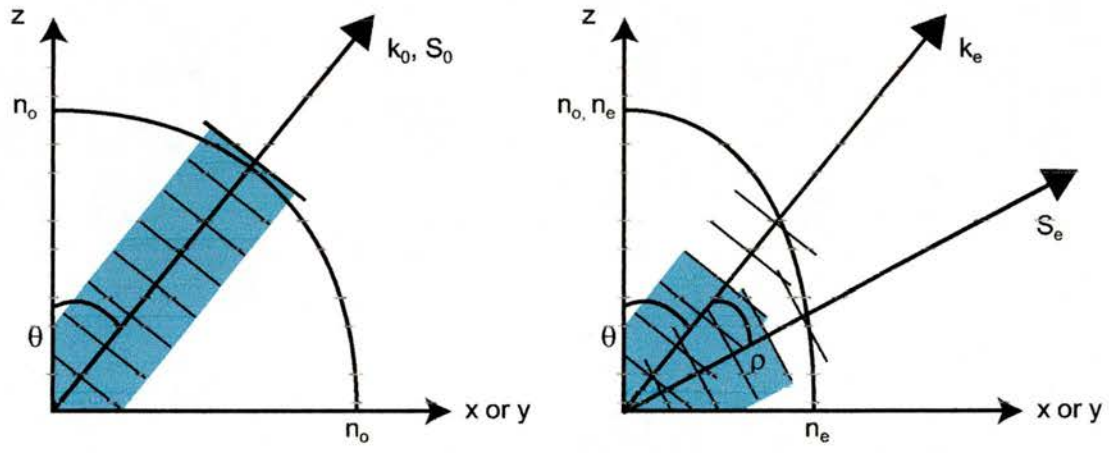

Figure 2-3. Direction of propagation of momentum vector $\mathbf{k}$ and Poynting vector $\mathbf{S}$ for (a) an o-wave and (b) an e-wave. The shaded area represents the region of spatial overlap between the o and e beams.

This results in a reduction in the interchange of energy between the pump and the generated fields with propagation through the medium. The double refraction angle is given by:

$$\rho(\theta) = \pm \arctan\left[\left(\frac{n_0}{n_e}\right)^2 \tan(\theta)\right] \mp \theta \qquad (2.28)$$

where a negative crystal corresponds to the upper sign and a positive crystal to the lower one. Note, there is no Poynting vector walk-off when $\theta = 90^\circ$ because

$\lim_{\varphi\to\infty} \arctan(\varphi) = 90^\circ$ therefore $\rho(\theta) \to 0$. This is the case for a non-critically phasematched arrangement. The distance which sets the upper limit to the maximum useful crystal length in the presence of spatial walk-off, is known as the *aperture length* and is given by

$$l_a = \frac{\sqrt{\pi} w_o}{\rho(\theta)} \tag{2.29}$$

where w_o is the input beam radius. For example, in a BBO crystal with $\rho \approx 5^\circ$ and a beam waist radius of 100 μm, the aperture length will be of the order of 2 mm.

The problem of spatial walk-off can be overcome by using a scheme called non-collinear phasematching. In this case, the ordinary and extraordinary waves are propagated with their momentum vectors at an angle to each other. The extraordinary Poynting vector walks onto the ordinary Poynting vector, thus increasing the interaction length.

Temporal walk-off

As well as spatial walk-off, temporal walk-off effects can also have a strong diminishing effect on the nonlinear gain, by limiting the useful interaction length. Temporal walk-off effects become even more significant in the ultrashort pulse regime. It is usual to describe the interaction of ultrashort pulses propagating through a dispersive medium in terms of their group velocities, as this is the speed at which the pulse envelope, and hence the pulse energy travels. On the other hand, the phase velocity defines the speed at which the different spectral components within the pulse travel through the medium. Temporal walk-off arises from the mismatch in the group velocity of the interacting pulses. This

has the effect that the nonlinear coupling and energy transfer between the pump and parametric pulses is reduced as they propagate through the crystal. Hence, the efficiency of nonlinear interaction can be severely limited by the mismatch in group velocities, despite proper matching of the phase velocities. For two collinearly propagating pulses, temporal walk-off, w, can be quantified in terms of the *pulse-splitting length*, l_s, which is defined as the distance after which they separate by a path equal to their pulse width, and is given by:

$$w = \frac{1}{v_{g1}} - \frac{1}{v_{g2}}$$
$$l_s = \frac{\Delta\tau}{w} \qquad (2.30)$$

where $\Delta\tau$ is the full-width half-maximum pulse duration and $v_g = \partial\omega/\partial k$ is the group velocity. Typical values of walk-off, for common OPO crystals, such as lithium niobate, are of around 100 fs/mm.

2.2.2 Quasi phase matching

The technique of birefringent phasematching, already mentioned, has been applied successfully for many wavelength regions. However, it does have its limitations particularly for the generation of mid-infrared wavelengths because there are very few materials that are both transparent and capable of phasematching beyond 4 μm with near infrared pumping. A different technique called quasi-phase matching (QPM) makes it possible to combine the convenience of noncritical phase-matching with the wavelength coverage of a critical geometry. Quasi-phase matching was devised independently by

Bloembergen *et al.* [4] and Franken & Ward [16] in 1962. The technique, which actually predates the development of birefringent phase-matching, corrects the relative phase at regular intervals by means of a structural periodicity built into the nonlinear medium. A particularly good type of periodic structure is one in which the effective nonlinearity of the crystal alternates between $-d_{eff}$ and $+d_{eff}$. The first demonstration of QPM was obtained using a stack of thin GaAs plates rotated by 180° to each other [17]. The most successful implementation of QPM has been in the growth of nonlinear ferroelectric crystals to which periodic field poling (or periodic poling) [18] is applied as described in the next section.

Consider a situation within an OPO where the pump, signal and idler wavelengths propagate collinearly through the crystal, but the interaction is not phasematched as the phase velocities are different. The sign of the power flow from one wave to the other is determined by the relative phase between the waves. The continuous phase slip between these waves caused by their differing phase velocities, leads to an alternation in the direction of power flow. This situation is shown by curve B in Figure 2-4. It can be seen that the alternating sign of the power flow leads to a repetitive growth and decay in the output power along the length of interaction. Throughout the crystal, the overall conversion efficiency will be negligible and no useful light will be generated. This detrimental effect is overcome by reversing the sign of the nonlinear crystal when the accumulated phase mismatch Δkl reaches π so that the phase difference is 'reset' back to zero. This creates a step-wise growth in the output power along the crystal length so that, on average, the proper phase relationship is maintained for growth of the generated interaction - see curve C in Figure 2-4. This represents the process of quasi-phasematching.

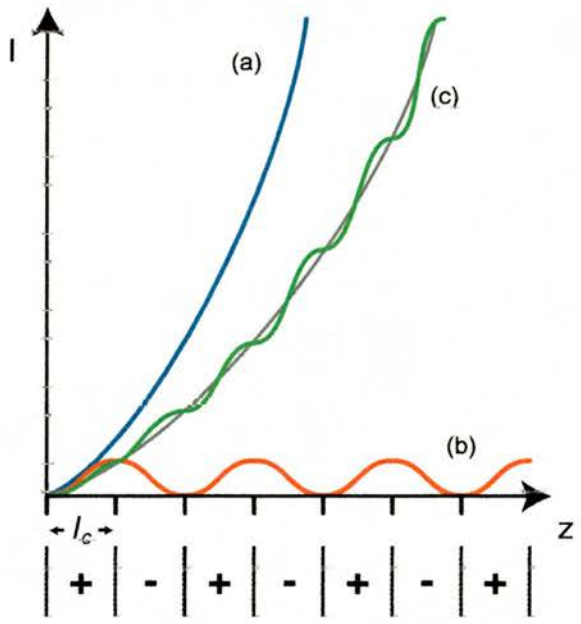

Figure 2-4. Plot of output power versus crystal length for (a) Perfect phasematching, (b) Non-phasematched interaction, (c) First order QPM

The modulation of the nonlinear sign within the crystal is referred to as a grating, and has an optimal grating period of, $\Lambda = 2l_c$. To introduce this periodic modulation, the nonlinear coefficient d_{eff}, is expressed by the Fourier expansion of its spatial harmonics along the direction of propagation [19]:

$$d_{eff}(z)e^{-i\Delta kz} \rightarrow d_{eff}\left[g(z)\right]e^{-i\Delta kz}$$
$$g(z) = \sum_{m=-\infty}^{\infty} G_m e^{-ik_m z} \tag{2.31}$$

where G_m are the Fourier coefficients and the m^{th}-harmonic grating vector

$$k_m = \frac{2\pi m}{\Lambda} \tag{2.32}$$

Thus, the grating period is introduced as an extra parameter in the wave-vector mismatch equation as:

$$\Delta k_Q = k_p - k_s - k_i - k_m \tag{2.33}$$

A value of $m = 1$ is referred to as a first order process. From Equation (2.31) we see that QPM is obtained when the period is chosen such that the spatial

harmonics $im(2\pi/\Lambda)z$ and the phase mismatch $-i\Delta kz$ compensate each other. In accordance with Equation (2.32), the grating period can then be written:

$$\Lambda = m\frac{2\pi}{\Delta k} \tag{2.34}$$

Let $g(z)$ from Equation (2.31) be a rectangular function of period Λ taking values of ± 1 (with the positive sections of length l), the duty cycle will be $D \equiv l/\Lambda$. The corresponding Fourier coefficients can be written as:

$$G_m = \frac{2}{\pi m}\sin(\pi m D) \tag{2.35}$$

Since $d_{eff}^{Q} = d_{eff}G_m$, the optimum effective nonlinearity for quasi-phasematching will occur with a duty cycle of 50% (i.e. $l \equiv \Lambda/2$) and $m = 1$. As the conversion efficiency in a nonlinear process varies as the square of the nonlinear coefficient, there exists a $(2/\pi)^2$ reduction on this efficiency of a first order QPM process compared with birefringent phase-matching, as shown in Figure 2-4. Thus, the nonlinear coefficient for a QPM process is given as:

$$d_{eff}^{Q} = \frac{2}{\pi m}d_{eff} \tag{2.36}$$

There are considerable advantages of quasi- over birefringent phasematching. The reliance of quasi-phasematching on a grating means that a nonlinear crystal can be tailored to phasematch any combination of wavelengths within the transparency range of the crystal. No limitations due to birefringence properties, any propagation direction and polarisation combination can be used. This means that beams can always be propagated along a crystal axis to avoid problems caused by Poynting vector walk-off. Temporal walk-off can still affect QPM and becomes more problematic for shorter pump pulses.

2.2.3 Periodic poling

Although QPM was initially proposed before birefringent phasematching, it was not widely used due to difficulties in fabrication. The fabrication of crystals suitable for QPM requires a method that can achieve uniform micrometer-scale periodic structures that maintain the materials nonlinearity, transparency and power handling capability. Recent advances in fabricating practical QPM materials have increased the popularity of QPM over birefringent phasematching.

QPM can be implemented in ferroelectric materials. Periodic reversal of the ferroelectric domains corresponds to a sign reversal of the nonlinear coefficient. Several techniques of varying success have been developed for periodically poling crystals. Chemical in-diffusion can produce patterns of shallow layers, suitable for waveguides but not deep enough for bulk devices [20,21]. Bulk devices have been made by modulation of the crystal growth process, but it suffers from axial variations in domain periodicity resulting in poor conversion efficiency [22,23]. Electron beam writing can produce good periodicity in bulk samples, but the reproducibility is poor and the process does not lend itself to commercial manufacturing [24]. A more reliable technique for fabricating gratings is called electric field poling [25].

Electric field poling was used to fabricate the crystals used in this work. The crystal is prepared by depositing a mask onto its surface, which defines the structure of the grating. There are two configurations for producing the mask both of which are patterned onto the +z surface of the wafer, Figure 2-5. In the first case, the conductor grating is patterned by lift-off lithography and a layer of photoresist applied on top. In the second case, a grating pattern of photoresist

is applied and covered by a film of conductor. In both cases the photoresist layer insulates the electrode lines, inhibits the domain growth between grating lines, and when covered with electrolyte, forms the contour of an isopotential surface.

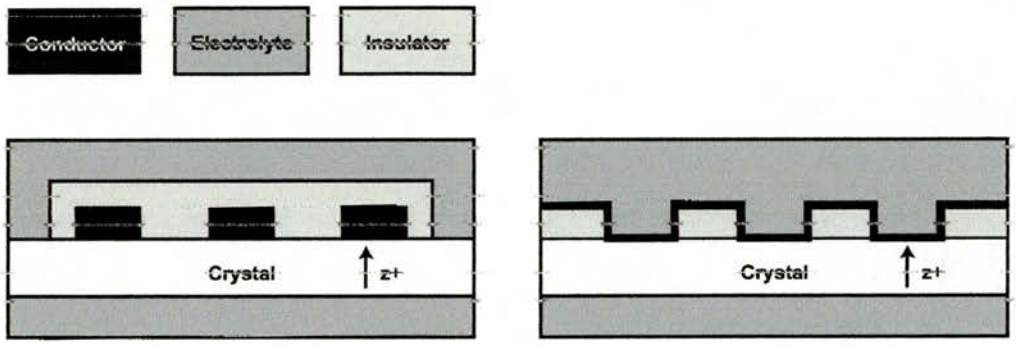

Figure 2-5. Electrode configurations for electric-field poling. The left figure shows insulator over conductor; the right figure shows a variant with conductor over insulator. In both cases the covering electrolyte connects the sample to a circuit that applies the electric field.

An electric field is then applied along the material that acts on the unprotected sections of the crystal to reverse the polarity. A qualitative picture of ferroelectricity in $LiNbO_3$ is shown in Figure 2-6.

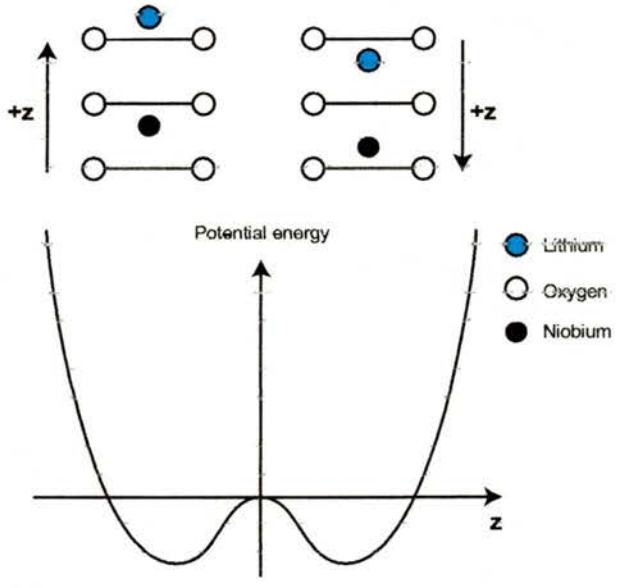

Figure 2-6. Qualitative illustration of ferroelectricity in $LiNbO_3$. Polarity of the two stable domain orientations is determined by the direction of offset of the metal ions relative to the oxygen layer.

The polarity of a ferroelectric domain is determined by the offset of the metal ions either above or below the oxygen layers. Domain reversal occurs when the applied electric field is greater than the coercive field of the material, which is ~21 kV/mm for $LiNbO_3$. The amount of charge Q required to reverse a single domain crystal of area A is related to the spontaneous polarisation P_s as

$$Q = 2AP_s \tag{2.37}$$

The poling process lasts long enough for the domain reversal to leak sideways into neighbouring domains. For this reason, the duty cycle of the mask has to be compensated in order to produce a precise 50:50 grating. The crystals are then annealed at a low temperature to reduce the strain imposed during the poling process.

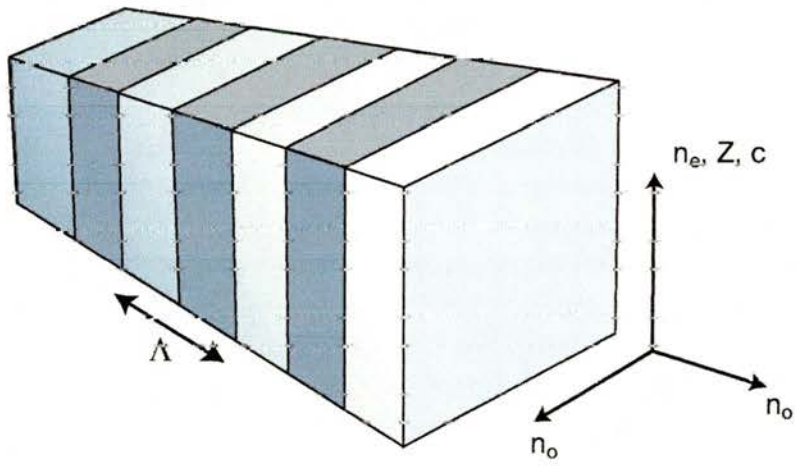

Figure 2-7 Illustration of a periodically poled crystal showing the alternating optical domains.

The final crystal consists of a series of nonlinear sections with alternately opposing domain polarisations. As light propagates through the crystal its phase will change by π for every domain change. For every odd multiple of the crystal coherence length l_c, such a reversal occurs and a phase shift builds by increments of π resulting in only constructive interference.

2.3 Conclusion

This chapter has discussed the basic concepts of nonlinear optics. Phasematching was discussed along with the birefringent and quasi-phasematching techniques used to achieve this. The general theory of QPM was reviewed along with the implementation of QPM devices by the periodic-poling technique in ferroelectric materials. It was shown that periodically poling these materials enables access to the largest nonlinear coefficients, therefore allowing more efficient frequency conversion processes.

This chapter has reviewed the theory behind the experiments described in the chapters to follow. The physical properties of the RTA and PPLN nonlinear crystals used in this work are given in Chapters 4 and 5 respectively.

2.4 References

1 J. A. Giordmaine and R. C. Miller, Physical Review Letters **14,** 973 (1965).

2 Zernike and Midwinter, *Applied Nonlinear Optics* (Wiley, 1973).

3 V. G. Dmitriev, G. G. Gurzadyan, and D. N. Nikogosyan, *Handbook of Nonlinear Optical Crystals*, Second Ed. ed. (Springer-Verlag, Belrin, 1997).

4 J. A. Armstrong, N. Bloembergen, J. Ducuing, and P. S. Pershan, "*Interactions between light waves in nonlinear dielectrics*", Physics Review Letters **127,** 1918-1939 (1962).

5 D. A. Kleinman, "*Nonlinear dielectric polarisation in optical media*", Physics Review Letters **126,** 1977 (1962).

6 P. G. Harper and B. S. Wherrett, *Nonlinear Optics*, Vol. Proceedings of the sixteenth Scottish Universities Sumer School in Physics (Adacdemic Press, New York, 1975).

7 R. W. Boyd, *Nonlinear Optics* (Academic Press Inc. (California, USA), 1992).

8 G. P. Agrawal and R. W. Boyd, *Contemporary nonlinear optics* (Academic Press, San Diego, 1992).

9 A. Yariv, *Optical Electronics*, 4th ed. (Saunders College Publishing USA, 1991).

10 R. L. Byer, in *Parametric oscillators and nonlinear materials*, 1977 (Academic Press, London).

11 M. Ebrahimzadeh, in *Laser Sources & Applications*; *Vol. 47*, edited by A. Miller and D. M. Finlayson (IOP, 1995).

12 S. E. Harris, Proc IEEE **57,** 2096 (1969).

13 R. S. Craxton, S. D. Jacobs, J. E. Rizzo, and R. Boni, IEEE Journal of Quantum Electronics **17,** 1781 (1981).

14 G. J. Edwards and M. Lawrence, "*A Temperature-Dependent Dispersion-Equation For Congruently Grown Lithium-Niobate*", Optical and Quantum Electronics **16,** 373-375 (1984).

15 D. H. Jundt, "*Temperature-dependent Sellmeier equation for the index of refraction, n(e), in congruent lithium niobate*", Optics Letters **22,** 1553-1555 (1997).

16 P. A. Franken and J. F. Ward, "*Optical harmonics and nonlinear phenomena*", Review Modern Physics **35,** 23-39 (1963).

17 D. E. Thompson, J. D. McMullen, and D. B. Anderson, "*Second harmonic generation in GaAs 'stack of plates' using high power CO2 laser radiation*", Applied Physics Letters **29,** 113 (1976).

18 L. E. Myers, R. C. Eckardt, M. M. Fejer, R. L. Byer *et al.*, "*Quasi-Phase-Matched Optical Parametric Oscillators in Bulk Periodically Poled Linbo3*", Journal of the Optical Society of America B-Optical Physics **12,** 2102-2116 (1995).

19 M. M. Fejer, G. A. Magel, D. H. Jundt, and R. L. Byer, "*Quasi-Phase-Matched 2nd Harmonic-Generation - Tuning and Tolerances*", IEEE Journal of Quantum Electronics **28,** 2631-2654 (1992).

20 M. L. Bortz, M. A. Arbore, and M. M. Fejer, Optics Letters **20,** 49 (1995).

21 E. J. Lim, M. M. Fejer, and R. L. Byer, Electronic Letters **25,** 174 (1989).

22 Y. Lu, L. Mao, and N. Ming, Optics Letters **19,** 1037 (1994).

23 G. A. Magel, M. M. Fejer, and R. L. Byer, Applied Physics **56,** 108 (1990).

24 H. Ito, C. Takyu, and H. Inaba, "*Fabrication of Periodic Domain Grating in Linbo3 By Electron- Beam Writing For Application of Nonlinear Optical Processes*", Electronics Letters **27,** 1221-1222 (1991).

25 M. Houe and P. D. Townsend, "*An Introduction to Methods of Periodic Poling For 2nd-Harmonic Generation*", Journal of Physics D-Applied Physics **28,** 1747-1763 (1995).

Chapter 3

Ultrashort Pulse Measurement

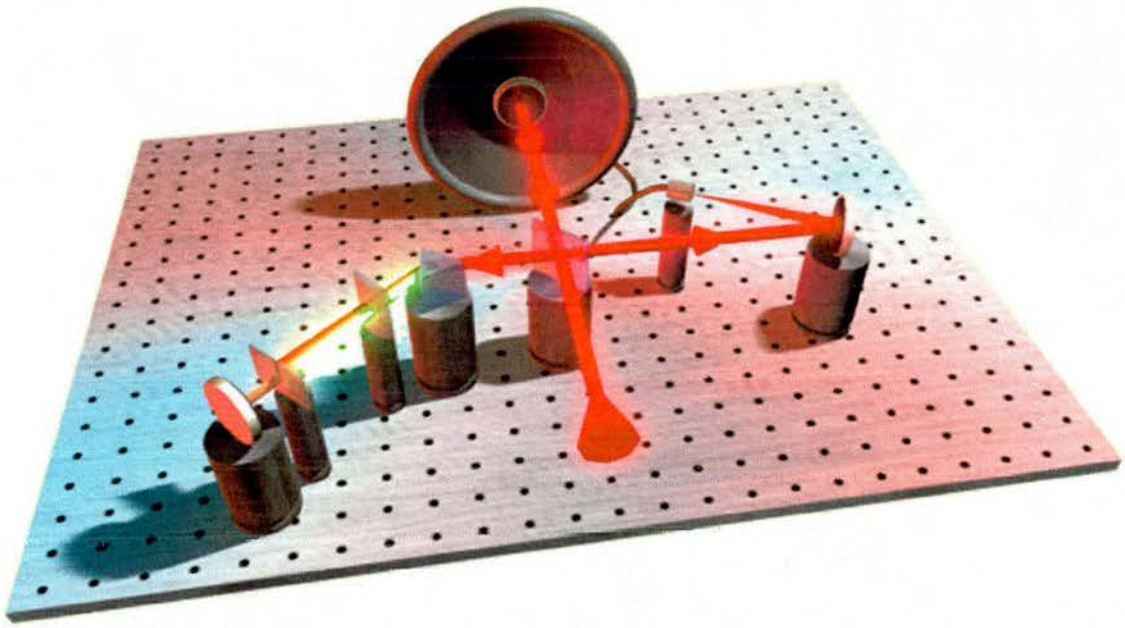

Artistic visualisation of the experimental sonogram setup.

3 Ultrashort Pulse measurement

It is widely understood that in order to measure the duration of an event, an even shorter event is required. This becomes a significant problem when trying to measure the fastest events man has ever made – the ultrashort light pulse. A photodiode and oscilloscope can give some information about the pulse train and inter-pulse effects, but the fastest photo-detectors operate at ~ 50 GHz frequencies so we are limited by their response times of tens to picoseconds [1]. The electron-optical streak camera provides direct linear measurements of optical pulses at resolutions close to 0.5 ps [2], but below picosecond durations less direct and more ambiguous techniques are required for pulse characterisations.

In this chapter, I will describe the experiments that were used to measure femtosecond pulses in the visible and mid infrared spectral regions. I will start by describing second harmonic generation autocorrelation, leading onto two-photon autocorrelation. This will be followed by two techniques; frequency resolved optical gating (FROG) and the sonogram, which are the time-frequency conjugates of each other.

3.1 Autocorrelation

The autocorrelation of an optical pulse allows conversion of the difficult problem of measuring timescales in the order of 100's of femtoseconds into two parts; firstly measuring lengths in the order of microns and secondly the signal intensity. For instance, in 100 fs light will travel 30 μm in air.

Correlation techniques can be classified in a number of ways; the first, *cross* correlation, is when one or more separate signals are correlated. The second is *auto*correlation where two or more replicas of a single pulse are used. The intensity of the incoming train of pulses is split within a Michelson type of optical delay line to form two pulse-trains of equal intensity. Since one pulse train is used to measure the other, the measurement process by definition cannot be shorter than the pulses duration. The convolution of one pulse with another creates an ambiguity and requires an assumption to be made about the pulse-shape before the pulse duration can be measured. However, this assumption can be corroborated with a spectral trace of the pulsed output acquired as a complement to the autocorrelation data. Spectral measurements of ultrashort laser and OPO pulses were acquired using a Rees E200 Series laser spectrum analyser [3].

3.1.1 Intensity autocorrelation

When the detector used in an autocorrelator has a slow frequency response (photomultiplier tube and oscilloscope), it will record a time average of the intensity autocorrelation data. This is called the intensity autocorrelation and is described in terms of the delay τ by

$$G_i(\tau) = \int_{-\infty}^{\infty} E^4(t)dt + \int_{-\infty}^{\infty} E^4(t-\tau)dt + 4\int_{-\infty}^{\infty} E^2(t)E^2(t-\tau)dt \qquad (3.1)$$

Considering the fact that $\int_{-\infty}^{\infty} I^2(t)dt = \int_{-\infty}^{\infty} I^2(t-\tau)dt$ where $I(t) = |E(t)|^2$ and when normalised for a background of unity, Equation (3.1) can now be written as

$$G_i(\tau) = 1 + 2g(\tau) \tag{3.2}$$

where $g(\tau)$ is the background free autocorrelation function described by

$$g(\tau) = \frac{\int_{-\infty}^{\infty} I(t)I(t-\tau)dt}{\int_{-\infty}^{\infty} I^2(t)dt} \tag{3.3}$$

The above equations are defined in terms intensity and so it follows that this type of autocorrelation is unaffected by the presence of chirp in the measured pulses. Even so, it is possible to deduce a certain amount of information about the behaviour of the laser under scrutiny. As shown in Figure 3-1a, the intensity autocorrelation trace of a perfectly modelocked pulse train exhibits a 3:1 contrast ratio between the signal peak and the background. For CW laser operation, the trace is resolved as a spike with a 3:2 ratio, Figure 3-1b. For the case of an incompletely modelocked pulse train, a CW spike will be superimposed on a broad pedestal, Figure 3-1c. Finally, double pulsing will create traces characteristic of Figure 3-1d.

An autocorrelation trace must always be a symmetric function about $\tau = 0$. As a result, the autocorrelation provides very little information on the pulse shape, because an infinity of symmetric and asymmetric pulse shapes can have very similar autocorrelations. Nevertheless, the intensity autocorrelation is generally the most widely used diagnostic technique, because it can be easily implemented, and is the first tool used to determine whether a laser is producing short pulses rather than the intensity fluctuations of continuous lasing.

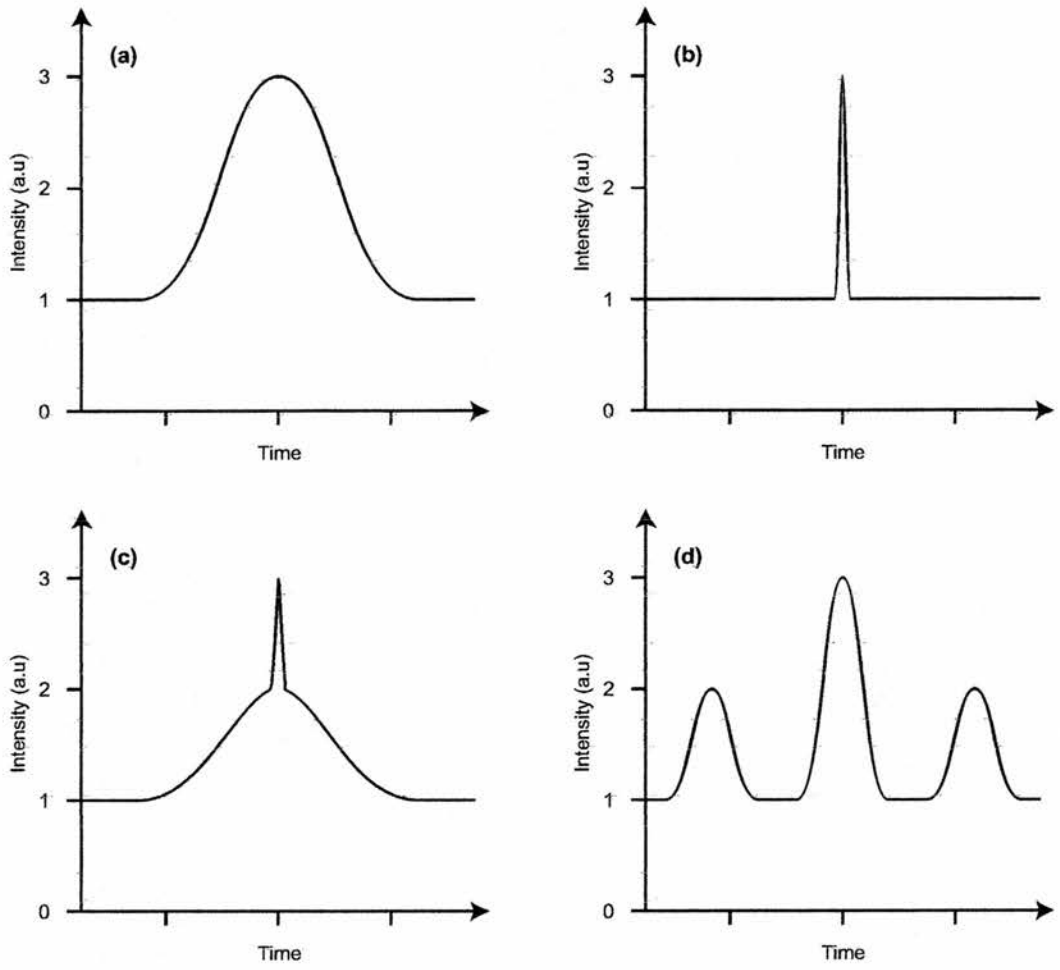

Figure 3-1 Example intensity autocorrelations of (a) modelocked pulse, (b) CW radiation, (c) partially modelocked pulse and (d) double pulsing.

In order to deduce a pulse duration from an intensity autocorrelation, a pulse shape has to be assumed (generally sech^2 or a Gaussian shape). This pulse shape is represented by a constant k in the relationship between the measured intensity autocorrelation width Δt and the FWHM pulse duration $\Delta\tau_p$, which is written as

$$\Delta\tau_p = \frac{\Delta t}{k} \tag{3.4}$$

The values of k are shown in Table 1 for various different pulse shapes.

Pulse profile	Time-bandwidth product $\Delta\tau_p\Delta\nu$	$k_{intensity}$	$k_{interferometric}$
Gaussian e^{-t^2}	0.441	$\sqrt{2}$	1.697
$\mathrm{sech}^2(t)$	0.315	1.543	1.897

Table 1 Theoretical conversion factors for intensity and interferometric autocorrelations.

3.1.2 Interferometric autocorrelation

A fringe-resolved autocorrelation is achieved by improving the time response of the detector (usually by impedance matching the oscilloscope to the detector with a suitable termination resistor). When $G(\tau)$ is normalised to give unit background, the interferometric autocorrelation can then be described by

$$G_f(\tau)=\frac{\int_{-\infty}^{\infty}\left|\left[E(t)\cos(\omega_0 t+\phi(t))+E(t-\tau)\cos(\omega_0(t-\tau)+\phi(t-\tau))\right]^2\right|^2 dt}{2\int_{-\infty}^{\infty}E^4(t)dt} \quad (3.5)$$

For values of the delay where pulses overlap, the interference terms will cause oscillation of the signal. The signal alternates between maximum and minimum values over a delay change of $\Delta\tau=\pm\pi/\omega$. This means that the autocorrelation is self-calibrating: the fringe separation corresponds to one optical cycle at the centre wavelength of the pulse. For instance, pulses centred at 840nm will have an optical cycle period of 2.8 fs.

For frequency unchirped pulses the envelopes that correspond to the upper and lower bounds (see Figure 3-2) of the fringes can be described by:

$$G_{fu} = \frac{\int_{-\infty}^{\infty} |E(t) + E(t-\tau)|^4 \, dt}{2\int_{-\infty}^{\infty} E^4(t)dt}$$
$$G_{fl} = \frac{\int_{-\infty}^{\infty} |E(t) - E(t-\tau)|^4 \, dt}{2\int_{-\infty}^{\infty} E^4(t)dt} \quad (3.6)$$

The contrast ratio for the interferometric measurements is found to be 8:1 because $G_f(\tau = 0) = 8$ for an unchirped pulse. This is much higher than the 3:1 contrast ratio from intensity autocorrelation measurements and conveys additional information regarding the frequency chirp present on a pulse. This is because a variation of the instantaneous phase over the duration of the pulse will reduce interference of the delayed pulses and hence reduce fringe visibility. Figure 3-2 shows a fringe-resolved interferometric autocorrelation trace.

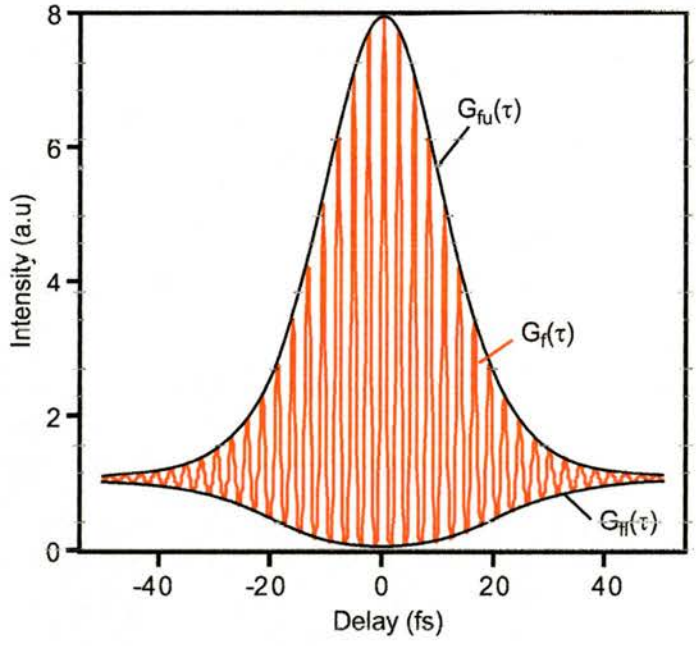

Figure 3-2 Interferometric autocorrelation.

3.1.3 Autocorrelation measurement

The first autocorrelator systems were based around a second harmonic generation (SHG) crystal. The nonlinear response of the SHG crystal provides a signal proportional to the degree of overlap of the pulses in the interferometer. The experimental arrangement of a SHG autocorrelator is described in Figure 3-3. The input pulse passes through a Michelson-type delay arrangement and the correlation, or overlap, of the pulses is designed to occur within a nonlinear crystal, such as β-barium borate (BBO). The pulses from each arm of the interferometer are spatially collinear and temporally overlapped. Pulses in one arm of the interferometer have a temporal delay τ relative to the other arm. Translating one of the mirrors about a point of coincidence varies the optical delay in the interferometer.

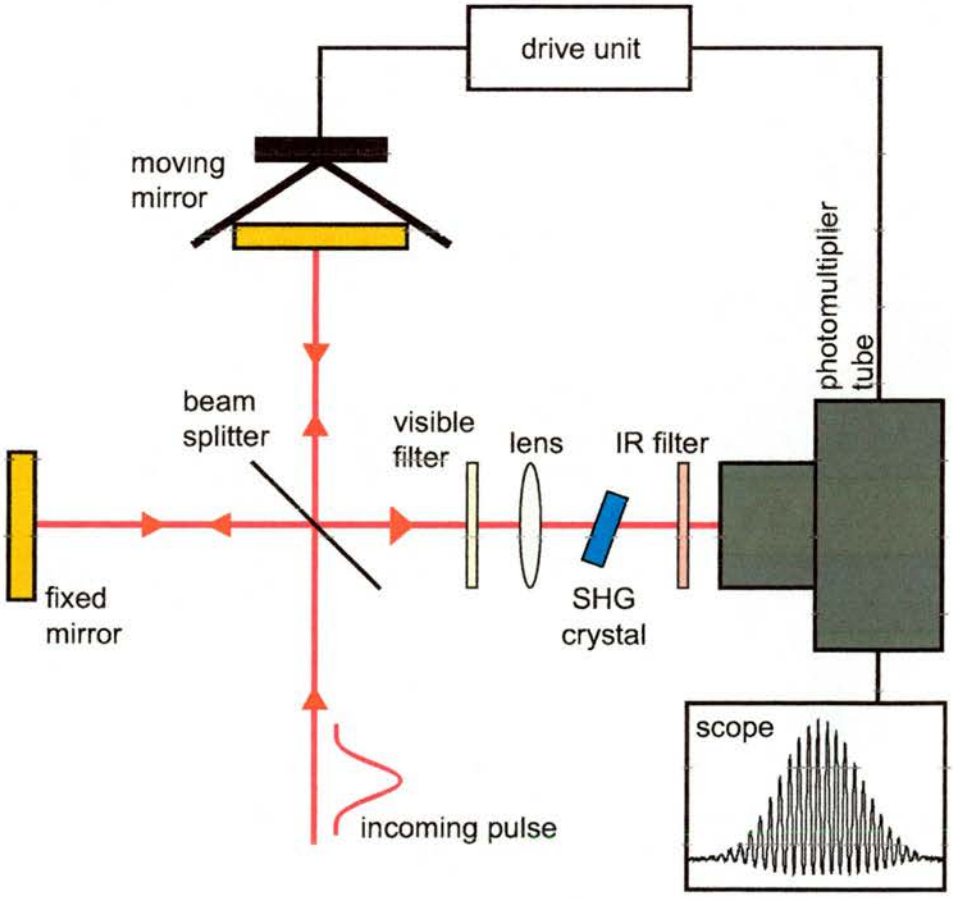

Figure 3-3 Schematic of the SHG autocorrelator.

Real-time monitoring of the autocorrelation function is accomplished by mounting one of the mirrors on an audio loudspeaker, for which the cone is made to scan at a low frequency ~20 Hz. As the speaker moves in and out, the path length for one sub-pulse is changed, so a delay is introduced into its arrival time at the crystal. When the path lengths for the two pulses are equal, the pulses will exactly coincide at the crystal and the amount of second harmonic light generated will be a maximum. As the speaker changes the delay, the second harmonic generation will drop. The speaker frequency is much less than the pulse repetition frequency, so the autocorrelation trace is made up from the second harmonic produced from many pulses, each subject to a different delay time.

The photomultiplier tube detects the second harmonic light generated in the nonlinear crystal and the resultant electrical signal is integrated over a period that is long compared to the pulse duration. The average power of the second harmonic light of the recombined beam is then recorded as a function of delay. The autocorrelation produced has a background level due to the signals from each arm, and a peak corresponding to the second harmonic generation when the pulses overlap. As mentioned before, the ratio of the peak to the background is well defined for a perfect modelocked pulse; hence, the autocorrelation can be used to adjust the laser for optimum performance.

3.1.4 Two-photon autocorrelation

Although the SHG autocorrelator is widely used, it does have several limitations, especially when trying to measure ultrashort pulses. The biggest drawback is the lack of suitable SHG crystals for the UV and mid-IR pulses. Even when a suitable crystal is used, systematic errors can occur due to the finite phasematching bandwidth available when measuring ultrashort pulses. In this case crystal thickness has to be kept to a minimum to ensure conversion of the entire phasematching bandwidth, but this is at the expense of the generated power. For longer pulses a thicker crystal could be used which in turn could introduce unwanted effects such as temporal walk-away and Poynting vector walk-off. In addition, when characterising large spectral ranges multiple doubling crystals may be needed due to its finite spectral bandwidth and phasematching properties.

As an alternative, semiconductor devices utilising two-photon absorption (TPA) can produce the necessary quadratic dependence of photocurrent on incident peak intensity required for autocorrelation measurements. TPA requires that the bandgap energy of the semiconductor is greater than the photon energy of the laser to be characterised. The TPA process involves one photon exciting a valence band electron into a virtual energy level, and the other photon provides the remaining energy to promote this electron into the conduction band. The response of this effect has a quadratic dependence on the intensity of the incident light [4], thus making it a suitable detector for second-order autocorrelation.

Although first reported in 1992, TPA autocorrelation has gained more attention recently with experiments demonstrating ultrashort pulse autocorrelation using

readily available, inexpensive devices such as LEDs and photodiodes, shown in Table 2.

Device	λ_{meas} [μm]	$\Delta\tau_p$	Ref.
AlGaAs LED	0.8	90 fs	[5]
Si photodiode	1.5	1.6 ps	[6]
InGaAs photodiode	2.5, 3.45	90 fs	[7]
GaAsP, GaP photodiodes	0.8	6 fs, 100 fs	[8] [9]
ZnSe photoconductive switch	0.8	120 fs	[10]
AlGaAs waveguide	1.047	17.7 fs	[11]
GaAs p-i-n waveguide	1.5	150 fs	[12]

Table 2. Summary of published TPA autocorrelation measurements

The use of TPA has several advantages over SHG for autocorrelation measurements. The TPA process is polarisation independent and non-phasematched, which greatly simplifies alignment! (see Figure 3-4 below).

Autocorrelation measurement is only possible as long as the TPA signal can be unambiguously resolved from the fundamental, so the incident wavelength must correspond to photon energies between half and one times the bandgap. This large range makes TPA autocorrelation well suited to measuring sub-10 fs laser pulses [8,9] and can eliminate realignment for tunable sources.

A number of different autocorrelator systems were used in this work and all were based around the design of Figure 3-4.

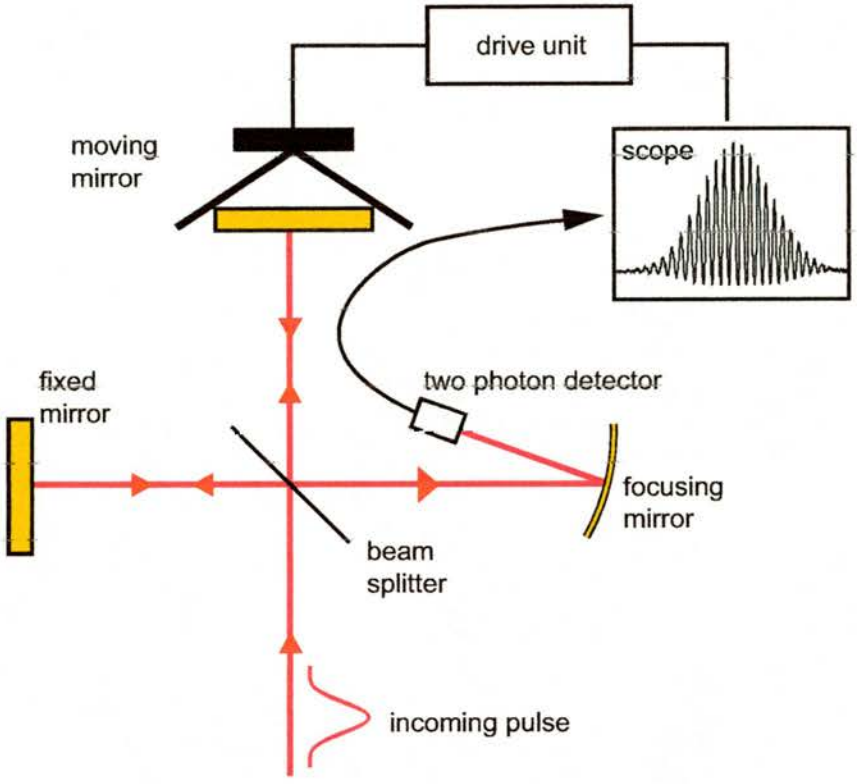

Figure 3-4 Schematic of the TPA autocorrelator

For the laser autocorrelation at 810 - 840 nm, a GaAsP photodiode (Hamamatsu G1116) was used with a set of gold mirrors. Another autocorrelator used an ultra-bright AlGaAs LED (E_g = 660 nm, Hamamatsu) with silver mirrors to measure the signal pulses around 1.1 μm from the various OPO systems. Finally, the idler pulses from the OPOs were measured with an InGaAs photodiode (Hamamatsu G5852-01) for ~3 μm wavelengths and an extended InGaAs photodiode (Hamamatsu G5853-01) for the 3.5 μm pulses. The experimental simplicity of TPA autocorrelation has resulted in the production of a commercial system based on a design by Dr Derryck Reid. Manufactured by Elliot Scientific, this system is known as "The Timewarp". It comprises of two small units; the detector and the driver boxes and simply requires the input pulse to be aligned normally into detector box. A significant time saver!

3.2 Frequency Resolved Optical Gating

The techniques for pulse measurement described so far can only provide qualitative information about the phase $\phi(t)$ of the pulse. In addition to that, autocorrelation requires prior assumptions about the functional form of the pulse envelope $I(t)$ [13]. However, in recent years a variety of time-frequency domain methods have been developed for making an absolute measurement of the amplitude and phase of the complex electric field $E(t)$ associated with an optical pulse. Direct optical spectral phase measurement (DOSPM) [14,15], frequency domain phase measurement (FDPM) [16], frequency-resolved optical gating (FROG) [17], and the sonogram [18].

The following sections describe two measurement techniques used in this work; the FROG which is the pulse spectrogram (intensity vs. frequency traces for different time delays), and the sonogram (intensity vs. time measured for different frequencies).

The experimental FROG setup is very similar to the SHG autocorrelation configuration; expect that a spectrometer is placed after the SHG crystal instead of a photomultiplier tube. The pulse to be measured is split into two replicas in a Michelson-type delay and then crossed in nonlinear optical medium. The experimental setup of the SHG FROG as used in this research project is shown in Figure 3-5. This design is optimised for measuring femtosecond laser pulses in that it uses an off-axis parabolic mirror to focus the two beams onto the KDP crystal and a split beam-splitter so that each beam experiences the same losses.

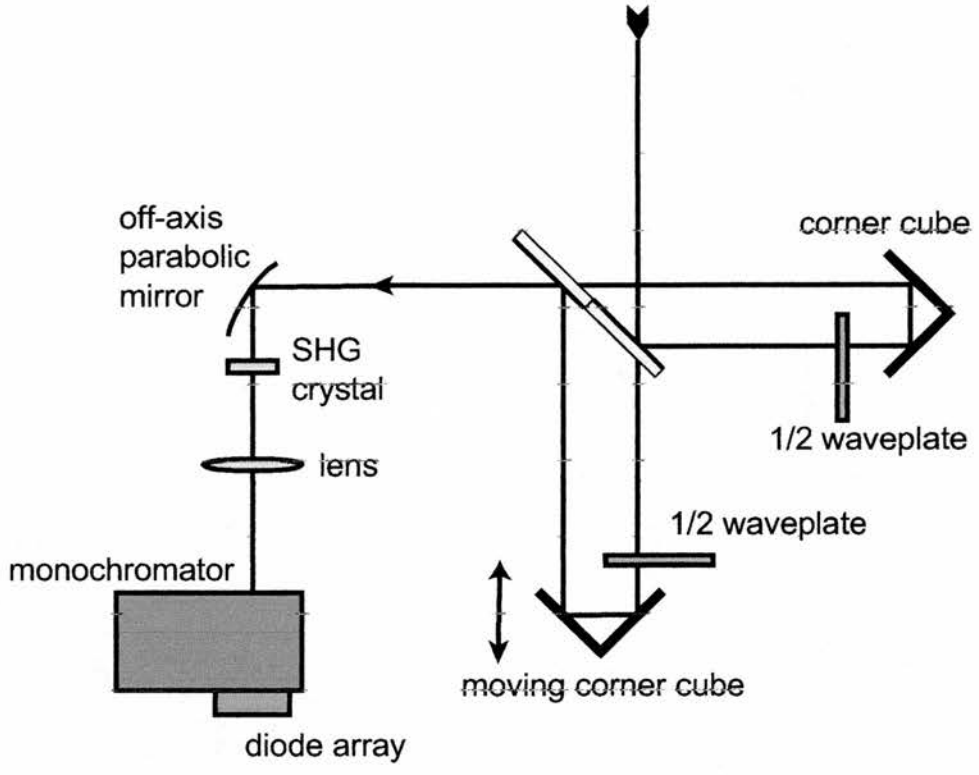

Figure 3-5 Experimental FROG setup. This design is optimised to minimise dispersion.

Examples of general SHG-FROG traces for different pulses can be seen in Figure 3-8. The results obtained from this FROG system are presented in Chapter 6 along with the experimental details.

The nonlinear mixing signal obtained from crossing the beams in the crystal is then resolved as a function of delay between the two beams and has an envelope of the form

$$E_{sig}(t,\tau) = E(t)g(t-\tau) \tag{3.7}$$

where $E(t)$ is the complex envelope of the pulse to be measured, $g(t-\tau)$ is an variable-delay gate function and τ is the delay between the two beams. A variety of nonlinear mechanisms can be used: polarisation (Kerr) rotation (polarisation-gate, PG-FROG), three-wave mixing (self-diffraction, SD-FROG) and second-harmonic generation (SHG-FROG). The nonlinear signal is then

used as the input to a spectrometer and the intensity is detected by a CCD array to yield the spectrogram, or FROG trace

$$I_{FROG}(\omega,t) = \left|\int_{-\infty}^{\infty} E_{sig}(t,\tau)e^{i\omega t}dt\right|^2 = \left|E_{sig}(\omega,\tau)\right|^2 \tag{3.8}$$

The FROG trace is a positive real-valued function of two variables, the frequency ω, and time delay τ, between the two pulses. The resulting pulse spectrogram shape depends on the choice of gating technique from which it was generated, in each case giving a significantly different trace.

Once the FROG trace has been captured, it is used as an input for an iterative two-dimensional numerical algorithm [19,20], which determines the full complex electric field, i.e. both the intensity and phase of the pulse that created the FROG trace.

A key component in the retrieval algorithm of spectrograms and sonograms is a mathematical concept known as generalised projections [21]. Projections offer a simple way to visualise the operation of these types of iterative algorithms and they provide a significant increase in the power of spectrogram and sonogram retrieval algorithms. This concept is described the next section.

3.2.1 Principal Component Generalised Projections

The retrieval of amplitude and phase of a pulse from a spectrogram or sonogram is done by applying an iterative minimisation algorithm based on principal component generalised projections (PCGP) [18,22-24].

The task of the retrieval algorithm is to find a signal field $E_{sig}(\omega)$ that satisfies two distinct constraints, i.e., the ability to be generated from a physically realisable field $E(\omega)$ through a known nonlinear optical process, and also the constraints of either Equations (3.8) or (3.12), that the magnitude squared of its Fourier transform match the experimentally measured trace.

This situation is illustrated in Figure 3-6, which shows that the correct solution lies at the intersection of the two sets of fields that satisfy the two individual constraints, the method of solution based on projections is also diagrammed. Starting with an arbitrary signal field (which will most likely be outside both constraint sets), a projection onto the first constraint set is made. A projection is chosen to the nearest point inside the target set. This is accomplished by minimising a distance metric between the starting point and a general point in the set. From this new point a projection into the second set is then performed, followed by a projection back onto the first set, etc. By iteratively projecting onto the two sets, we will eventually arrive at the intersection of the two sets, that is at the correct answer.

The sets shown in Figure 3-6 are convex; a line joining any two points on one set never leaves that set. When both constraint sets are convex convergence is guaranteed (this is known as the method of projections). In the case of one or both of the sets being nonconvex, convergence can not be guaranteed mathematically (this method is known as general projections, GP's) and the method can become stuck on protrusions in the constraint sets. This is the case

for FROG and sonograms where the constraint sets are both nonconvex, however, GP's work well in the retrieval algorithms for these measurements.

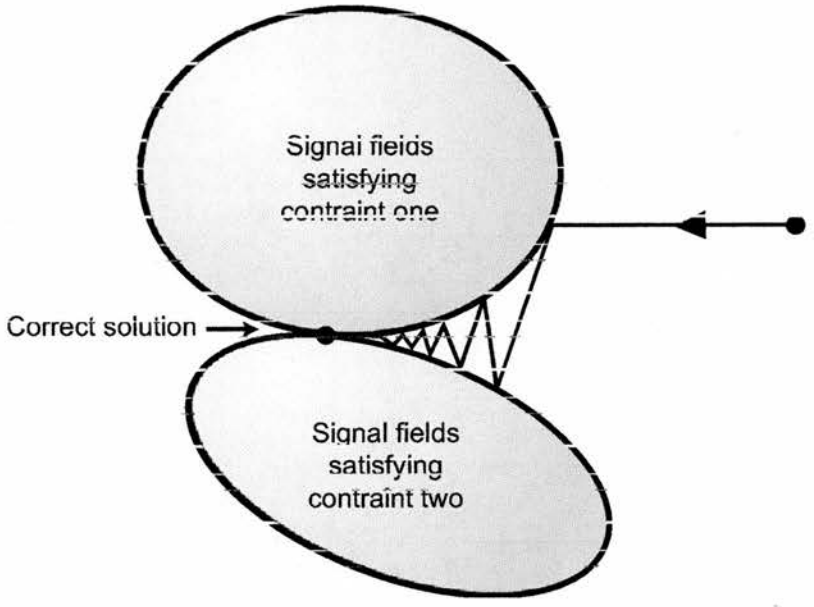

Figure 3-6 Schematic of the method of generalised projections. The figure is illustrative; in FROG or sonograms the sets reside in higher order space and may be of a more complicated structure.

The problem with the basic implementation of general projections is that it is quite slow to determine the next guess for the electric field, which minimises the error (distance) to the next point on the other constraint set. However, the principal component general projection (PCGP) algorithm avoids the need for minimisation [17]. Based on the idea that the FROG or sonogram can be constructed from an outer product of two vectors representing the pulse and gate, the PCGP algorithm reduces the construction of a new guess for the pulse and gate to a calculation of two eigenvectors.

Finally, it is possible to determine the properties of the gate and signal pulses without prior knowledge. The pulse-extraction problem is now much more complex and it would not appear that the spectrogram or sonogram contains

sufficient information to determine both pulses. However, the mathematics used in the two-pulse-extraction problem is equivalent to two-dimensional blind deconvolution [25]. This is a technique originally from image science that quite counter intuitively allows the extraction of both the image and an unknown blurring function from a blurred image. Although the one-dimensional blind deconvolution problem has ambiguities, the two-dimensional version surprisingly yields essentially unique results provided a simple constraint exists. Variations of blind-deconvolution algorithms succeed in extracting the signal and gate pulses from spectrograms and sonograms.

3.2.2 FROG Pulse Retrieval

The FROG algorithm is shown diagrammatically in Figure 3-7. Starting with a guess solution for the field $E(t)$ we generate a signal field from that guess field using Equation (3.7), and then Fourier transform it into the (ω,τ) domain. The intensity of the signal field $E_{sig}(\omega,\tau)$ is then replaced by the intensity of the measured FROG trace $E'_{sig}(\omega,\tau)$:

$$E'_{sig}(\omega,\tau)=\frac{E_{sig}(\omega,\tau)}{\left|E_{sig}(\omega,\tau)\right|}\left[I_{FROG}(\omega,\tau)\right]^{1/2} \tag{3.9}$$

This forms the first projection onto the set of signal fields that satisfy the first constraint given by Equation (3.8).

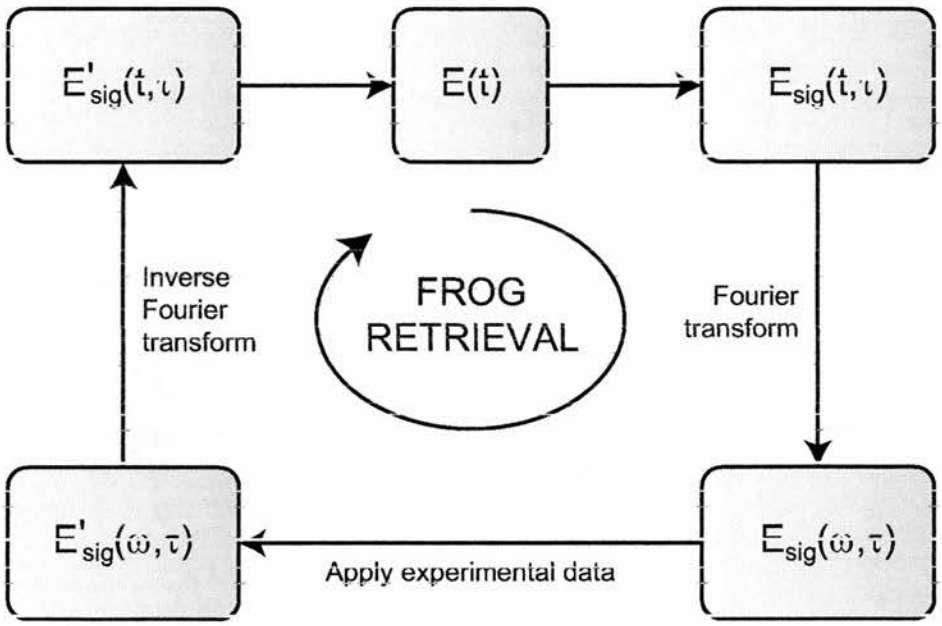

Figure 3-7 Flow diagram of the FROG pulse-retrieval algorithm

An inverse Fourier transform then converts the signal electric field $E'_{sig}(t,\tau)$. In order to implement the second projection a signal field is determined that satisfies the second constraint, Equation (3.7) and is closest to $E'_{sig}(t,\tau)$. This results in an improved guess pulse $E(t)$ and the process continues until the algorithm has converged sufficiently and the pulse can be identified. The convergence is monitored by calculating the root-mean-square (rms) error G, of the experimentally measured FROG trace I_{FROG} and the square of the magnitude of the signal field generated by the current guess for $E(t)$:

$$G = \sqrt{\frac{1}{N^2}\sum_{\omega,\tau=1}^{N}\left(I_{FROG}(\omega,\tau) - \left|E_{sig}(\omega,\tau)\right|^2\right)^2} \qquad (3.10)$$

The value N is the number of delay events for which there are N frequency values. The delay and frequency increments are related by

$$\partial\nu = \frac{1}{N\partial\tau} \qquad (3.11)$$

A $N \times N$ square array is required in order to use fast Fourier transforms.

3.3 Sonogram

The experimental quantity measured by FROG is the pulse spectrogram (intensity vs. frequency traces for different time delays), but an alternative measurement able to provide equivalent information is the sonogram of the pulse, (intensity vs. time measured for different frequencies):

$$I_{sonogram}(t,\Omega)=\left|\int_{\infty}^{-\infty}E(\omega)_{sig}G(\omega-\Omega)\mathrm{e}^{-i\omega t}d\omega\right|^2 \qquad (3.12)$$

The sonogram records the group delay of each frequency component using a frequency-filter $G(\omega-\Omega)$ around a variable centre frequency Ω, followed by a time-resolved measurement of its intensity.

A sonogram is obtained experimentally using a Michelson interferometer that has been modified to provide a near dispersionless filter (for example, the nondispersive grating spectrometer design described in [26]). In the interferometer the pulse is split into two replicas, one of these is frequency filtered and then cross-correlated with the other using a second-order nonlinearity. The experimental sonogram measurement of a femtosecond laser pulse is described in Chapter 4.

Unlike SHG FROG, a sonogram measured using this experimental procedure is not symmetric; therefore it is possible to determine the sign of the chirp on the pulse. A further advantage of the sonogram over SHG-FROG measurement is that it can be recorded using two-photon absorption in a photodiode [5] to provide the second-order nonlinearity. This allows for the characterisation of short femtosecond pulses without introducing systematic errors that can arise from the limited phase-matching bandwidth of a frequency-doubling crystal [27].

A visual comparison of how the traces of an autocorrelation, SHG-FROG and SHG-sonogram vary with different pulse shapes can be seen in Figure 3-8.

Note that the sign of the chirp on a pulse is represented by the tilt on the sonogram trace, whereas the FROG trace is identical for positive and negative chirp.

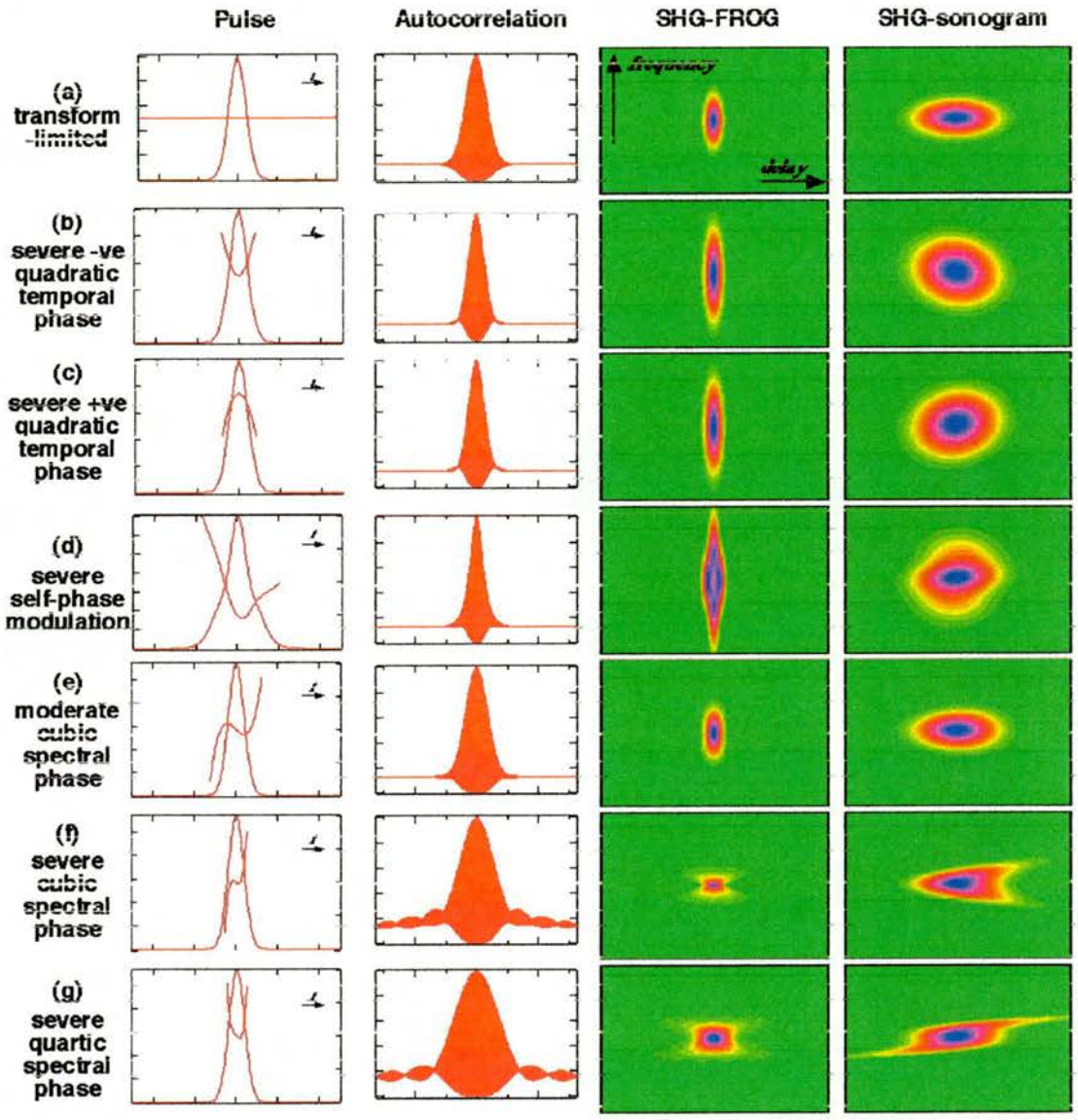

Figure 3-8 A comparison of interferometric autocorrelation, SHG-FROG and SHG-sonogram with different pulse shapes

3.3.1 Sonogram Pulse Retrieval

Sonogram pulse retrieval uses a blind-deconvolution PCGP algorithm. It is based on a matrix approach using the idea that a sonogram can be generated from the outer product of the pulse spectral amplitude and the frequency filter [18]. The procedure for generating a sonogram can be seen in Figure 3-9. Firstly the outer product between the pulse and filter row vectors $E_i(\omega)$ and $G_j(\omega)$ is formed. A row rotation procedure then sorts the resulting matrix into columns of constant frequency delay Ω (which is the difference between the centre frequencies of the pulse and the filter) and rows of constant pulse local frequency ω. The columns are then arranged into increasing frequency delay order [17]. Fourier transforming the matrix rows gives the complex amplitude of the sonogram signal. The intensity of this matrix is the sonogram trace, which is measurable experimentally. Applied in reverse, this process forms the basis of the pulse-retrieval algorithm depicted in Figure 3-10.

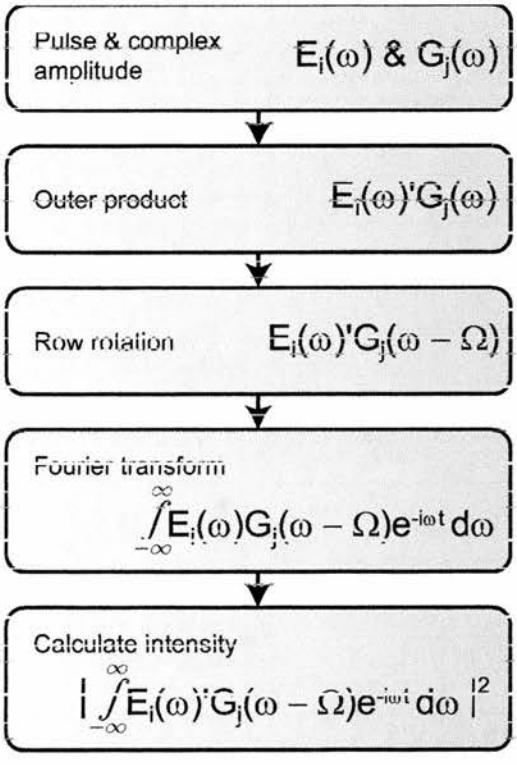

Figure 3-9 Procedure for generating a sonogram using the outer product formulation.

The filter and pulse trial solutions are created by generating a Gaussian envelope with random phase. The envelope is used directly as the trial solution for the filter transmission and is Fourier transformed to provide a trial solution for the pulse spectral amplitude. The sonogram complex amplitude corresponding to the trial pulse and filter is then calculated and its intensity is then replaced by the intensity of the laboratory-measured sonogram. The resulting pseudo-sonogram is manipulated into the outer-product form and the next guess for the pulse spectral amplitude and the filter transmission found by principal component decomposition.

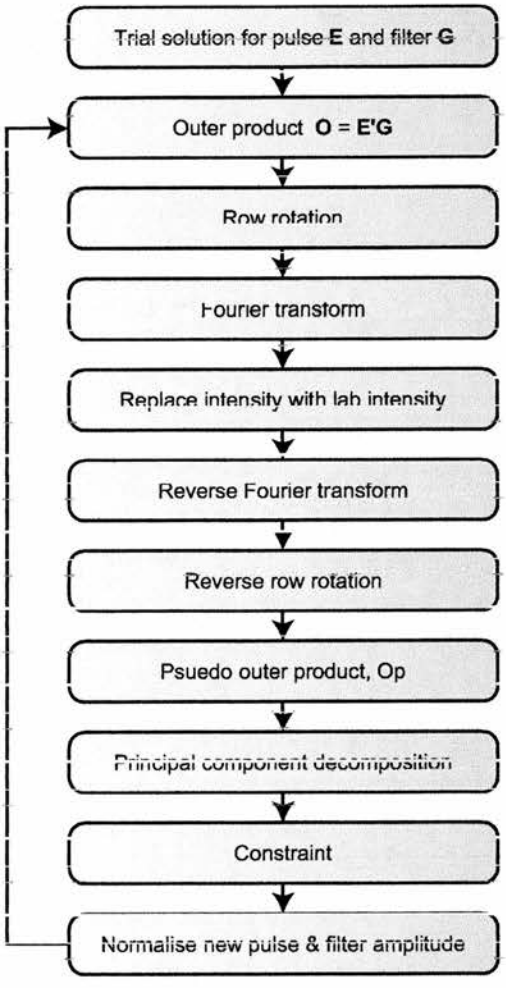

Figure 3-10 Schematic representation of pulse retrieval from a sonogram measurement

There is in principal, potential for an ambiguity to arise because more than one pulse-filter pair is able to generate a sonogram that matches the experimentally measured signal. However, in practice it is possible to avoid this ambiguity by choosing a gate much narrower than the signal spectrum or by using some additional constraint on the retrieved data. The simplest constraint is to set the filter phase to zero. This is justifiable for the typical sonogram filter, which consists of a spatially dispersive prism followed by a slit. No wavelength-independent phase errors will be added by this system and therefore has no intrinsic spectral phase. It is worth noting that this constraint is not directly possible in FROG algorithms because the pulse is retrieved in the time domain.

Full details of an experimental sonogram measurement described here are discussed in the next chapter.

3.4 Conclusions

In this chapter, several techniques were discussed for the measurement of ultrashort pulses. The relevant concepts behind intensity and interferometric SHG autocorrelation were introduced along with their limitations for measuring femtosecond pulses. Autocorrelators utilising two-photon were presented and their experimental simplicity and ability to measure femtosecond pulses highlighted.

The limitation of $\chi^{(2)}$-based autocorrelators to provide complete phase information about the femtosecond pulses has lead to alternate measurement techniques. The FROG and sonogram time-frequency domain techniques were introduced as powerful tools to supersede autocorrelators. The concepts of these techniques were presented as a background for the experimental work presented in subsequent chapters.

Finally, just as FROG and sonogram measurement techniques are becoming commonplace for the femtosecond experimentalist, very new developments by Trebino *et al.* [28] could do away with both of them! The new measurement technique, coined Grating-Eliminated No-nonsense Observation of Ultrafast Incident Laser Light E-fields (GRENOUILLE, which is the French for "frog") has greatly simplified the experimental procedure for producing a time-frequency domain measurement. See Figure 3-11.

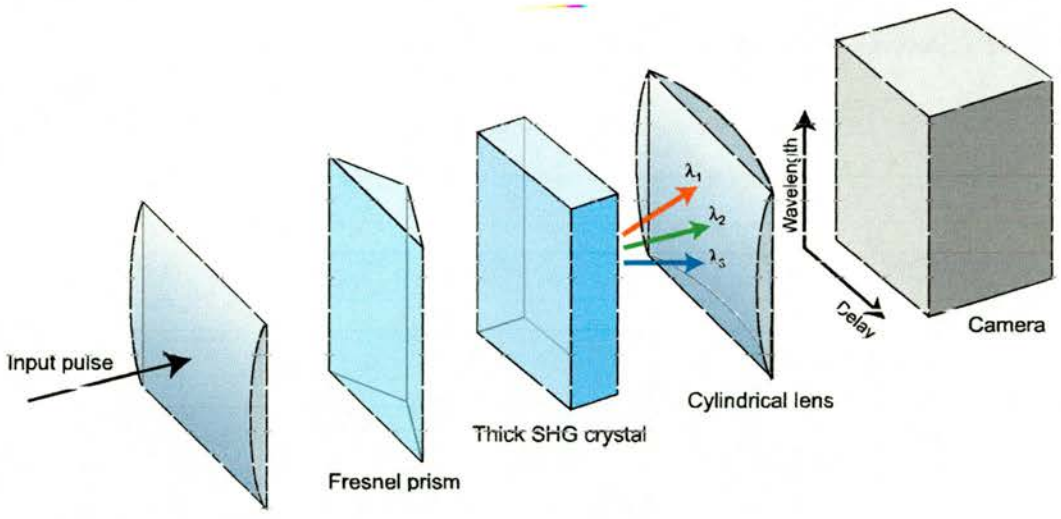

Figure 3-11 The simplicity of the GRENOUILLE system

The GRENOUILLE system uses a Fresnel biprism to replace the beam splitter, delay line, and beam-recombining optics. It maps delay to position at the crystal. GRENOUILLE also uses a thick SHG crystal acting as both the nonlinear-optical time-gating element and the spectrometer producing a complete single-shot SHG FROG trace. However, most importantly GRENOUILLE has no sensitive alignment parameters making the experimentalist's life much easier!

3.5 References

1 D. G. Parker, P. G. Say, A. M. Hansom, and W. Sibbett, "*110ghz High-Efficiency Photodiodes Fabricated From Indium Tin Oxide-Gaas*", Electronics Letters **23,** 527-528 (1987).

2 A. Finch, Y. Liu, H. Niu, W. Sibbett *et al.*, (Springer-Verlag, New York, 1988).

3 Rees Instruments Ltd, (Thornbrook, Weyside Park, Cattleshall Lane, Godalming, Surrey, GU7 1XE).

4 A. Yariv, 3rd ed. ed. (Wiley, New York, 1989), p. 64.

5 D. T. Reid, M. Padgett, C. McGowan, W. E. Sleat *et al.*, "*Light-emitting diodes as measurement devices for femtosecond laser pulses*", Optics Letters **22,** 233-235 (1997).

6 L. P. Barry, B. C. Thomsen, J. M. Dudley, and J. D. Harvey, "*Autocorrelation and ultrafast optical thresholding at 1.5 mu m using a commercial InGaAsP 1.3 mu m laser diode*", Electronics Letters **34,** 358-360 (1998).

7 D. T. Reid, C. McGowan, M. Ebrahimzadeh, and W. Sibbett, "*Characterization and modeling of a noncollinearly phase-matched femtosecond optical parametric oscillator based on KTA and operating to beyond 4 mu m*", IEEE Journal of Quantum Electronics **33,** 1-9 (1997).

8 J. K. Ranka, A. L. Gaeta, A. Baltuska, M. S. Pshenichnikov *et al.*, "*Autocorrelation measurement of 6-fs pulses based on the two- photon-induced photocurrent in a GaAsP photodiode*", Optics Letters **22,** 1344-1346 (1997).

9 A. Baltuska and e. al., "*All solid state cavity dumped sub-5-fs laser*", Applied Physics B **65,** 175 (1997).

10 W. Rudolph, M. SheikBahae, A. Bernstein, and L. F. Lester, "*Femtosecond autocorrelation measurements based on two-photon photoconductivity in ZnSe*", Optics Letters **22,** 313-315 (1997).

11 M. M. Karkhanehchi, C. J. Hamilton, and J. H. Marsh, "*Autocorrelation measurements of modelocked Nd:YLF laser pulses using two-photon absorption waveguide autocorrelator*", IEEE Photonics Technology Letters **9,** 645-647 (1997).

12 Z. Zheng, A. M. Weiner, J. H. Marsh, and M. M. Karkhanehchi, "*Ultrafast optical thresholding based on two-photon absorption GaAs waveguide photodetectors*", IEEE Photonics Technology Letters **9,** 493-495 (1997).

13 Z. E. Penman, T. Schittkowski, W. Sleat, D. T. Reid *et al.*, "*Experimental comparison of conventional pulse characterisation techniques and second-harmonic-generation frequency-resolved optical gating*", Optics Communications **155,** 297-300 (1998).

14 K. C. Chu, J. P. Heritage, R. S. Grant, K. X. Liu *et al.*, "*Direct Measurement of the Spectral Phase of Femtosecond Pulses*", Optics Letters **20,** 904-906 (1995).

15 B. S. Prade, J. M. Schins, E. T. J. Nibbering, M. A. Franco *et al.*, "*A Simple Method For the Determination of the Intensity and Phase of Ultrashort Optical Pulses*", Optics Communications **113,** 79-84 (1994).

16 J. L. A. Chilla and O. E. Martinez, "*Direct Determination of the Amplitude and the Phase of Femtosecond Light-Pulses*", Optics Letters **16,** 39-41 (1991).

17 D. J. Kane, G. Rodriguez, A. J. Taylor, and T. S. Clement, "*Simultaneous measurement of two ultrashort laser pulses from a single spectrogram in a single shot*", Journal of the Optical Society of America B-Optical Physics **14,** 935-943 (1997).

18 D. T. Reid, "*Algorithm for complete and rapid retrieval of ultrashort pulse amplitude and phase from a sonogram*", IEEE Journal of Quantum Electronics **35,** 1584-1589 (1999).

19 R. Trebino and D. J. Kane, "*Using Phase Retrieval to Measure the Intensity and Phase of Ultrashort Pulses - Frequency-Resolved Optical Gating*", Journal of the Optical Society of America a-Optics Image Science and Vision **10,** 1101-1111 (1993).

20 K. W. Delong and R. Trebino, "*Improved Ultrashort Pulse-Retrieval Algorithm for Frequency- Resolved Optical Gating*", Journal of the Optical Society of America a-Optics Image Science and Vision **11,** 2429-2437 (1994).

21 A. Levi and H. Stark, in *Image Recovery* (Academic, San Diego, Calif., 1987), p. 277-320.

22 K. W. Delong, D. N. Fittinghoff, R. Trebino, B. Kohler *et al.*, "*Pulse Retrieval in Frequency-Resolved Optical Gating Based On the Method of Generalized Projections*", Optics Letters **19,** 2152-2154 (1994).

23 V. Wong and I. A. Walmsley, "*Ultrashort-pulse characterization from dynamic spectrograms by iterative phase retrieval*", Journal of the Optical Society of America B-Optical Physics **14,** 944-949 (1997).

24 D. J. Kane, "*Real-time measurement of ultrashort laser pulses using principal component generalized projections*", IEEE Journal of Selected Topics in Quantum Electronics **4,** 278-284 (1998).

25 B. C. McCallum and J. M. Rodenburg, "*Simultaneous Reconstruction of Object and Aperture Functions From Multiple Far-Field Intensity Measurements*", Journal of the Optical Society of America a-Optics Image Science and Vision **10,** 231-239 (1993).

26 A. M. Weiner, J. P. Heritage, and E. M. Kirschner, "*High-Resolution Femtosecond Pulse Shaping*", Journal of the Optical Society of America B-Optical Physics **5,** 1563-1572 (1988).

27 G. Taft, A. Rundquist, M. M. Murnane, I. P. Christov *et al.*, "*Measurement of 10-fs laser pulses*", IEEE Journal of Selected Topics in Quantum Electronics **2,** 575-585 (1996).

28 R. Tribino, P. O'Shea, M. Kimmel, and G. Xun, in *Optics & Photonics News*; *Vol. 12* (2001).

Chapter 4

Ti:sapphire Ring Laser and PPLN-OPO

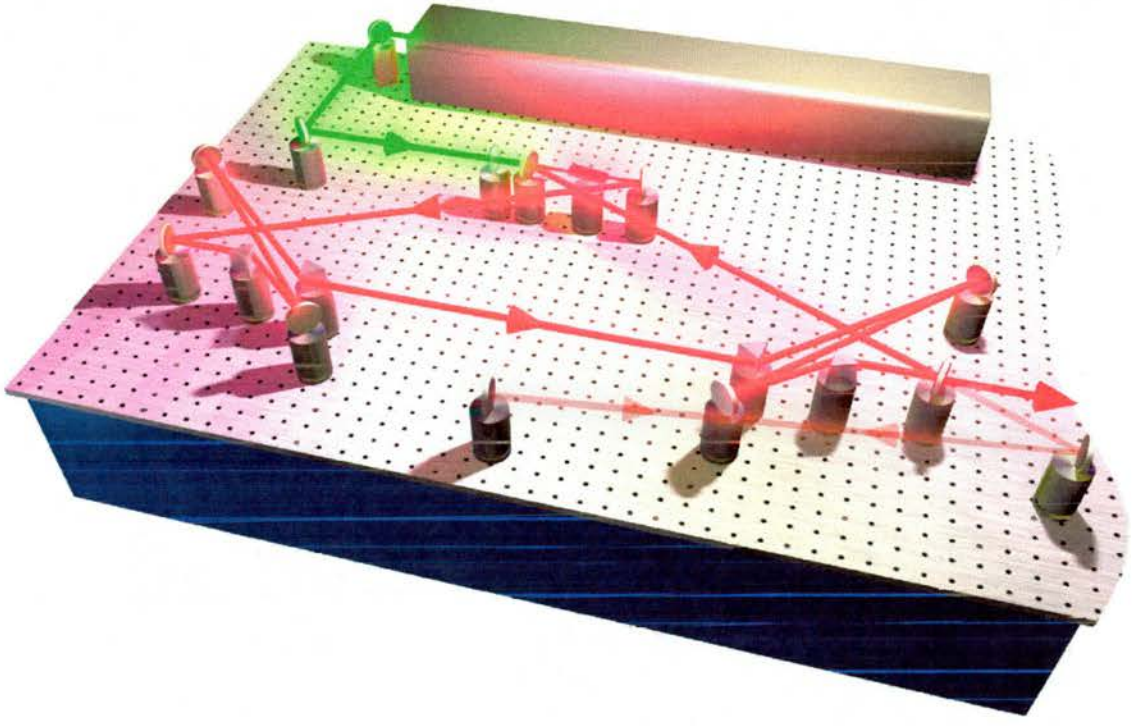

Artistic visualisation of the Ti:sapphire ring laser

In recent years there has been great interest in passively mode-locked lasers with high average output powers. The need for such lasers is driven by many applications, particularly those involving nonlinear wavelength conversion, which require the high peak powers these lasers provide. Ti:sapphire lasers producing sub-20-fs pulses have been available for a number of years, but the systems demonstrated to date, in contrast with their ~100-fs counterparts, have not generally been capable of producing more than a few hundred milliwatts of average output power. Reasons for this include thermal management problems arising as a result of using thin, highly absorbing crystals to minimize intracavity group-velocity dispersion and chaotic in-stabilities caused by excessively high intracavity peak powers. At present, the frontiers in the picosecond regime are just below 30 W, [1-3] whereas in the femtosecond regime average output powers of a few watts have been demonstrated. [2,4-7]

In this Chapter descriptions are given for the design and operation of a high-energy sub-20-fs Ti:sapphire laser oscillator capable of producing 1-MW peak power pulses with an average power of 1.5 W. The application of this laser as a pump source for a PPLN OPO in a first attempt to generate few optical cycle pulses in the mid-infrared is then described.

4 The Ti:sapphire ring laser

The laser cavity is shown schematically in Figure 4-1 was based on a Spectra-Physics Millennia X (diode-pumped frequency-doubled Nd:YVO_4) pump laser and a 10-mm-long Brewster-cut Ti:sapphire crystal. The Millennia X provided up to 10 W of green light at 532 nm. The vertically polarised light from the Millennia had to be rotated using a multiple-order half-wave plate so as to enter the Ti:sapphire crystal as horizontally polarised light. The crystal had a pump absorption coefficient of 2.3 cm^{-1}. It was wrapped in a sheet of gold foil to make good thermal contact with the crystal mount which was cooled using low-pressure water. A Peltier-effect cooler was used to maintain the crystal at a constant temperature of 15 °C.

The Ti:sapphire laser was configured as a folded, self-modelocked, unidirectional ring oscillator [8]. The two curved mirrors at the gain crystal both had radius of curvature of -100 mm. With the exception of the output coupler, which was 5% transmitting at 850 nm (LaserOptik GmbH, Germany), the plane cavity mirrors used were standard commercially available broadband high reflectors coated from 710 nm to 890 nm (Newport UF.20). Second and third-order group-velocity dispersion compensation was provided by two pairs of intracavity fused-silica prisms (apex angle 69°), each with a separation distance of 590 mm. Extracavity dispersion compensation was included in the form of a sequence of another two pairs of fused-silica prisms, each with a separation distance of 350 mm. This compensation was necessary to remove chirp acquired by the pulse after passing through the 7-mm-thick BK7 substrate of the output coupler.

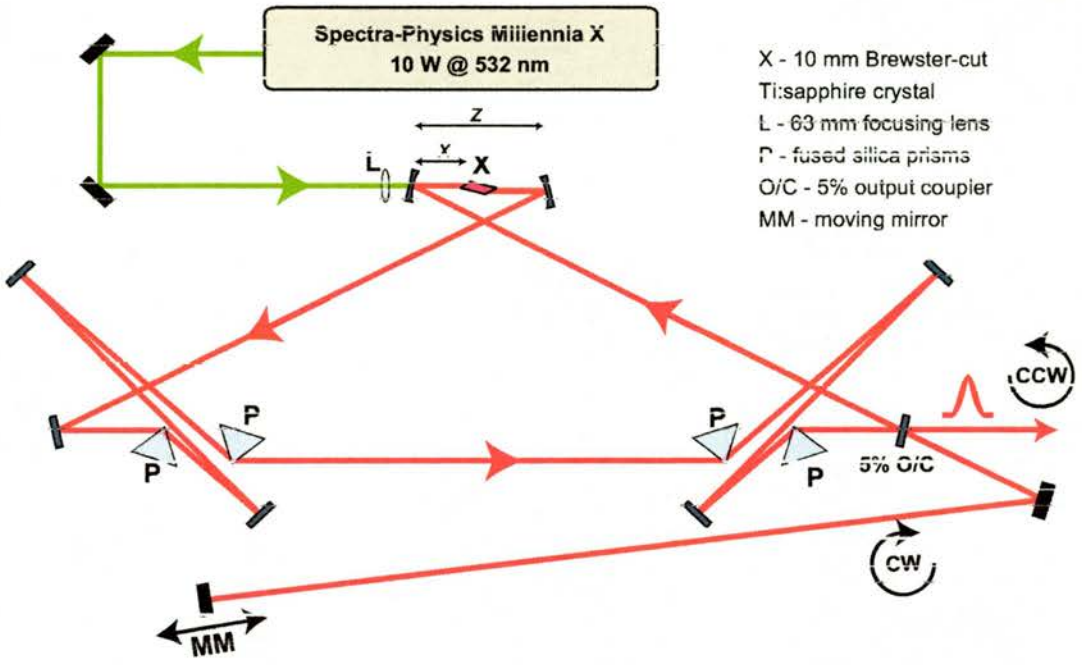

Figure 4-1 Schematic of the folded Ti:sapphire ring-cavity configuration

There are several advantages to using the self-modelocked ring configuration. First, the symmetric cavity design allows mode-locking at the centre of the resonator stability range and therefore maximizes the output power from the laser. Second, the pulse has travelled through the crystal only once per round trip and therefore crystal dispersion is minimized. This is a significant feature because it permits the use of a crystal double the length of that which could be included in a linear resonator. Using a longer crystal allows a lower doping level, more-uniform heat extraction, and more-stable intracavity focusing.

A further advantage of the ring design is its insensitivity to optical feedback. The ring cavity was relatively tolerant to a optical feedback into the laser cavity. This is most likely due to the fact that the retroreflected light is injected into the cavity in the direction opposite to the unidirectional lasing. Small intracavity levels of optical feedback into a linear cavity design generally destroy the modelocking, such that an optical isolator must be inserted after the output coupler. This has

the detrimental effect of adding excessive pulse broadening dispersion to the output pulses.

The final advantage of the ring cavity design is the ability to include a self-starting mechanism in the form of an extracavity moving mirror. This was implemented with an aluminium mirror mounted upon a small audio loudspeaker running at approximately 10 Hz [8].

Before modelocking, the laser operated with continuous-wave (CW) outputs in both clockwise and anticlockwise directions independent of cavity alignment. The modelocked operation occurred in one direction, which was dependent on cavity alignment. The dominant modelocking orientation was optimised for counter-clockwise pulse propagation by maximising the CW power in that direction. Counter-clockwise modelocking operation was preferred so that the pulses would experience gain soon after entering the crystal. These pulses would then be of highest intensity during their propagation through the crystal inducing greater self-phase modulation (SPM) which increased spectral broadening thus enabling support of shorter pulse durations.

The clockwise output of the laser is retroreflected back into the cavity in the counter-clockwise direction by the moving mirror, MM. The distance from the output coupler to the moving mirror is set to interfere a clockwise pulse with a corresponding counter-clockwise pulse in the Ti:sapphire crystal. In other words, this distance is approximately equal to one half the differences in optical path length between the counter-clockwise path from the crystal to the output coupler (through the prism sequence) and the clockwise path from the crystal to the output coupler. The moving mirror initiates the modelocking and subsequently forces unidirectional output in the counter-clockwise direction. The

modelocking is completely unperturbed by the moving mirror; the external cavity only initiates modelocking and can be blocked during continuous modelocked operation with no effect.

In collaboration with the Mohebi group at CICESE in Mexico, the laser resonator was modelled using the nonlinear ABCD matrix method [9]. We considered the nonlinear propagation of the pump beam in the gain medium due to the non-uniformly distributed thermal lens, in addition to the nonlinear propagation of the laser beam caused by the Kerr effect. The stable regions of the laser were mapped for the two parameters (denoted in Figure 4-1) x, the position of the front face of the rod with respect to the input curved mirror, and z, the separation between curved mirrors. The intracavity power of the laser was varied from cw to modelocked level, and for all stable points the value of the Kerr-lens modelocking parameter (KLMP) as defined in [9] was calculated. Figure 4-2 shows an x-z stability map for the conditions of this laser. The grey scale represents the values of the KLMP in the range of 10^{-6} to 10^{-9} W^{-1}. The maximum value of the KLMP (6.0×10^{-27} W^{-1}) occurs at x = 47.0 mm and z = 109.0 mm.

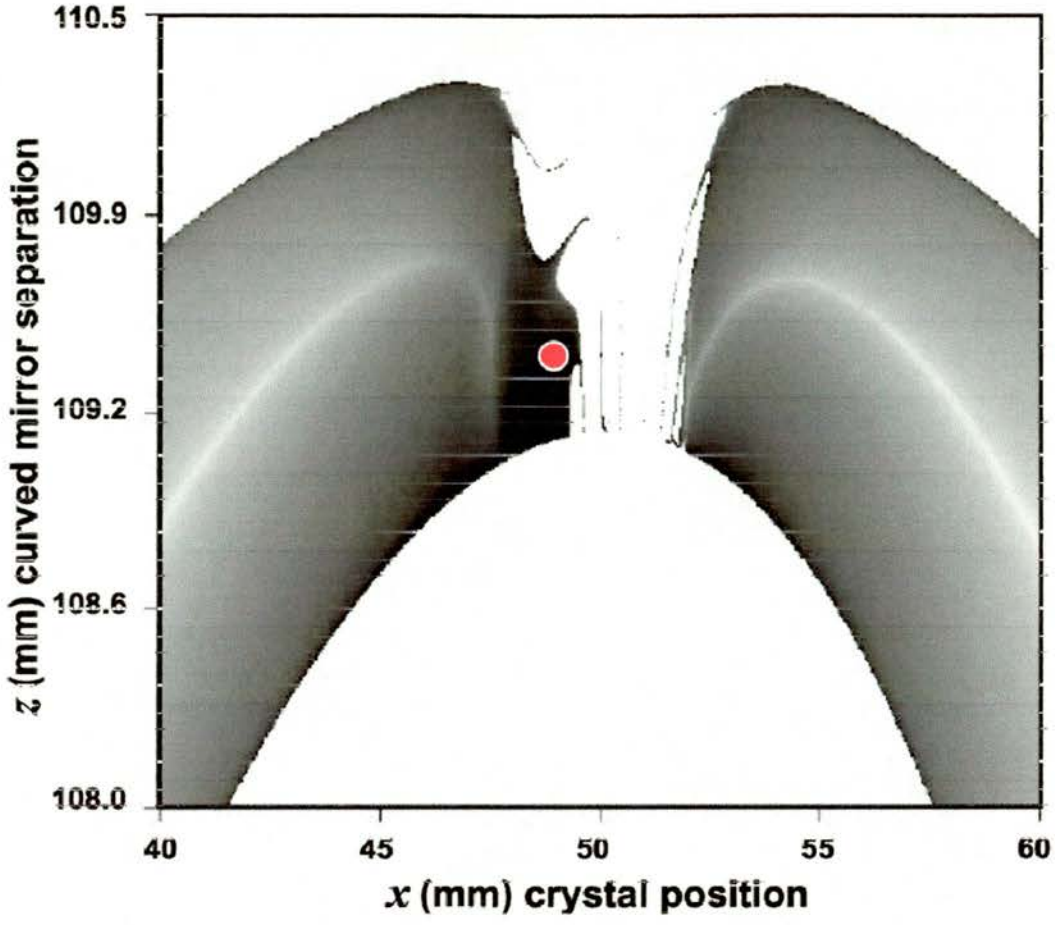

Figure 4-2 Stability map of the laser for the crystal position, (x), and the curved mirror separation, (z). The grey scale is a logarithmic representation of the KLMP values, where darker means higher Kerr-lens modelocking sensitivity. The white areas are unstable for a mode-locked pulse. The left-hand stability region is most sensitive to thermal effects. (In conjunction with J. Garduno-Mejia, N. Jamasbi & M. Mohebi, C.I.C.E.S.E, Mexico)

The percent volume overlap of the pump and laser beams over the entire rod length was calculated to be 70% for the conditions in which the laser operated. Laser operation was in the parameter space of the map marked by an open circle.

4.1 Results from the Ti:sapphire ring laser

Autocorrelation profiles of the output pulses were measured with a low-dispersion Michelson autocorrelator composed of a 100-μm-thick beam splitter, gold coated reflective and focusing optics, and a GaAsP photodiode (Hamamatsu G1115) used in its two-photon absorption regime [10]. A fringe-resolved autocorrelation measurement of pulses from the laser configured with a 5% output coupler is shown in Figure 4-3, and the pulse duration that was determined from this measurement, by assuming a $\text{sech}^2(t)$ intensity profile, was 13 fs. The corresponding spectrum was smooth, with a bandwidth of 55 nm centred on a wavelength of 815 nm. Taken together, these data imply a time–bandwidth product of 0.33, indicating that the pulses were close to the transform limit (assuming a $\text{sech}^2(t)$ pulse shape in which the ideal transform limit is 0.315). The average output power of the laser in this measurement exceeded 1.4 W, corresponding to an impressive pulse peak power of 1 MW and a pulse energy of 13 nJ.

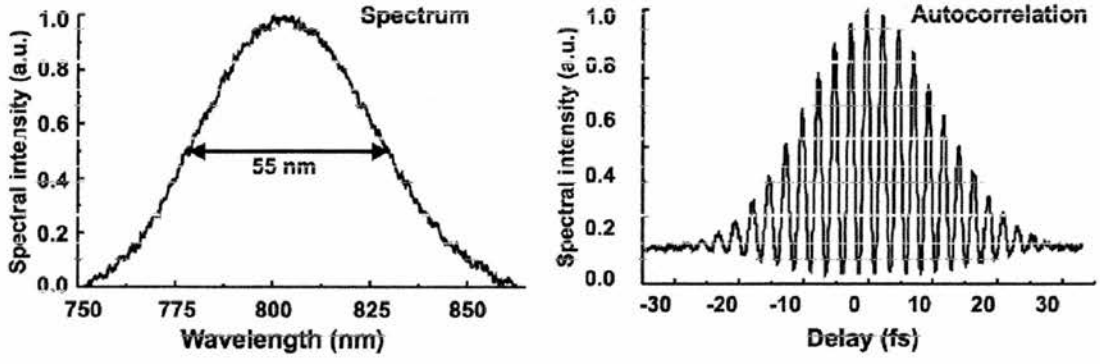

Figure 4-3 Spectrum with a FWHM bandwidth of 55 nm and interferometric autocorrelation of output pulses from the laser running at a centre wavelength of 815 nm

Operating in this configuration, the laser remained mode locked for several hours, indicating that either the laser was stably supporting multiple pulses or that the intracavity pulse peak powers must be close to the critical power for catastrophic self-focusing. Measurements of the rf spectrum of the laser output confirmed that no widely spaced multiple pulsing occurred, and autocorrelation measurements showed only occasional evidence of very small satellite pulses. It was concluded therefore, that a single high-peak-power intracavity pulse was circulating. With such high intracavity peak-powers catastrophic self-focusing effects would be expected. This effect occurs with circulating pulses have an intensity great enough to cause a splitting in the pulses. First, the pulse broadens due to group velocity dispersion. As the pulse starts to focus, the region neat the pulse centre undergoes the most self-phase modulation. Dispersion causes the modulated portion of the signal to flow away from the pulse centre, resulting in a splitting of the initial pulse. There are a couple of explanations why this was not observed; firstly the intracavity dispersion reduced the peak power of the pulse to a value lower than the critical power for catastrophic self-focusing. Secondly, the pulse entering the crystal may have had sufficient peak power to cause catastrophic self-focusing after some critical distance, but as it propagated it was dispersion broadened such that the conditions for catastrophic self-focusing lapsed before the pulse had covered this distance. For our system, the critical power corresponds to a critical focal distance of 10 mm, and group-velocity dispersion broadens the pulse by a factor of 6 across this length.

4.2 Sonogram measurement

By increasing the output coupling to 10%, an average power of 1.7 W was obtained, but the pulse duration increased to 20 fs. The output pulses generated with the latter configuration were monitored by measuring their sonogram trace [11,12]. (The sonogram is the signal obtained by mapping the arrival time and the intensity of each spectral component within the pulse as described in Chapter 3).

Measurement of the sonogram trace is easy to implement by acquisition of a series of cross correlations between the pulse and its frequency-filtered replica for a range of filter centre frequencies. If the filtered pulse is at least a few times longer than the unfiltered pulse, then the measured signal is the sonogram trace described above. In practice, a digital storage oscilloscope was used (Tektronix TDS 210), together with a cross-correlator based on a GaAsP photodiode (Hamamatsu G1116). The reference arm was designed to have minimum dispersion and consisted of a 100 μm thick broad-band dielectric beam splitter with a 50:50 splitting ratio and a silver mirror mounted on a loudspeaker cone. In the other arm a dispersive frequency filter was configured using an SF14 prism followed by a 200 mm focal length collimating lens and terminated with a silver mirror. A slit was placed directly in front of the mirror which could be translated across the dispersed beam to select different wavelength components, see Figure 4-4.

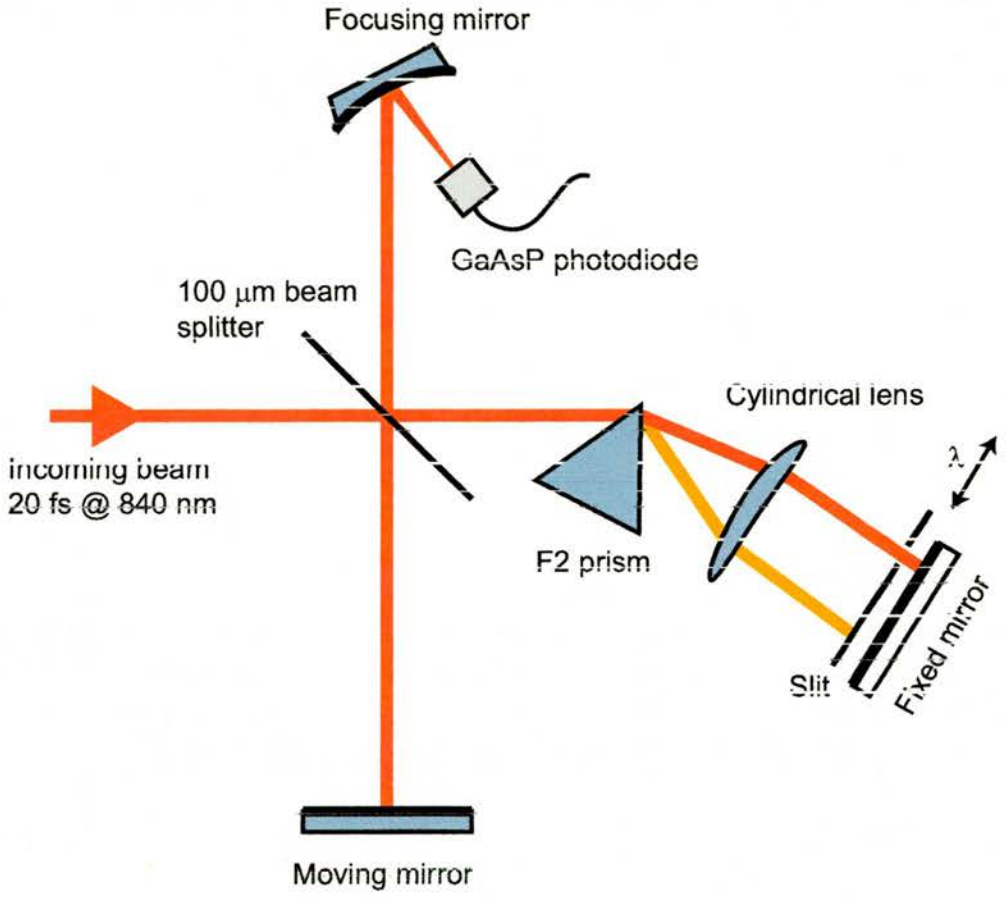

Figure 4-4 Schematic of the optical system used to acquire the experimental sonogram trace.

Unlike second-harmonic frequency resolved optical gating (FROG), the sonogram measurement can be carried out with a two-photon absorption photodiode as the nonlinear mixer and therefore avoids the bandpass filtering inherent in using a phase-matched frequency-doubling crystal for very broad-bandwidth pulses.

Acquisition of the data was achieved by recording 30 cross correlations, each corresponding to a different filter centre wavelength and separated by 3.3 nm wavelength intervals. After acquisition the data were resampled to a 64 x 64 array for processing and retrieval of the pulse with a matrix-based retrieval algorithm, as described in Chapter 3, operating without any spectral constraint.

The measured sonogram trace is shown as Figure 4-5(a), and the trace produced by the retrieved pulse is given for comparison in Figure 4-5(b).

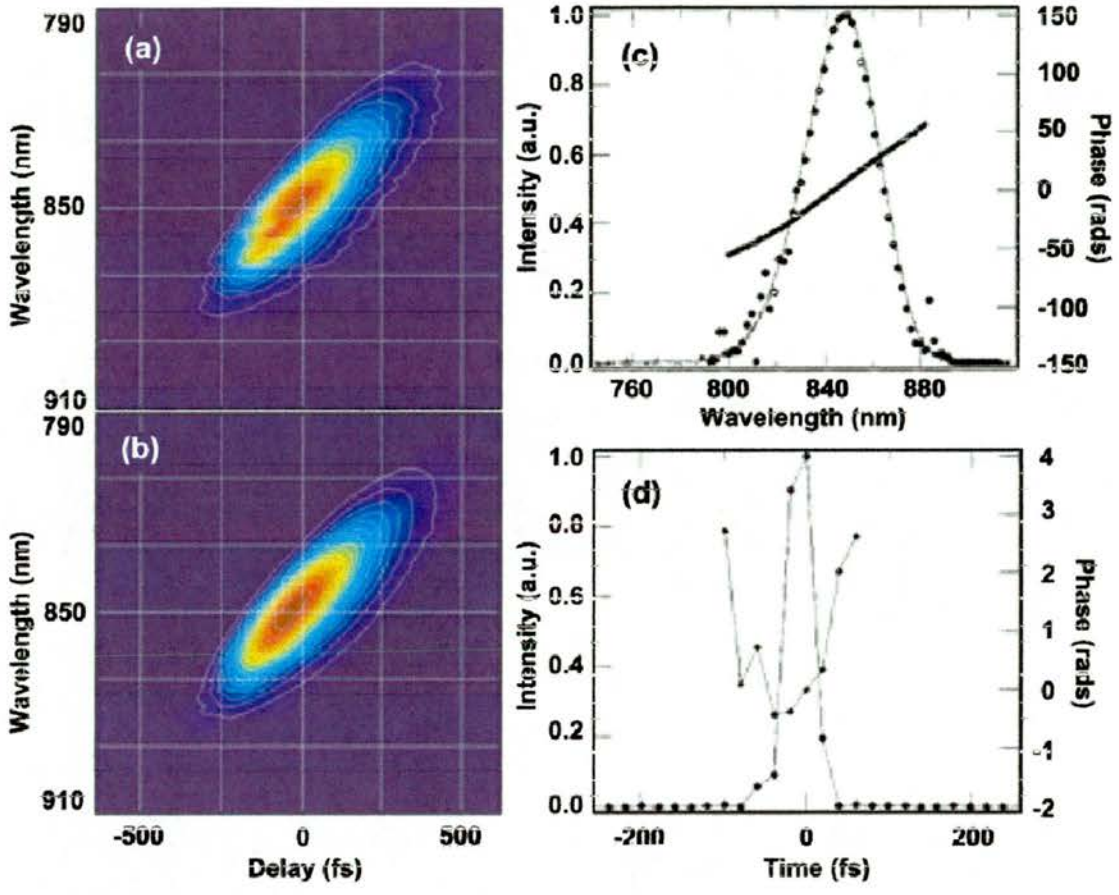

Figure 4-5 (a) Measured sonogram trace and, (b) sonogram trace reconstructed from the retrieved pulse data. (c) Retrieved spectral intensity and phase plotted with the independently measured pulse spectrum (d) Retrieved temporal intensity and phase.

The sonogram gives an intuitive representation of the chirp on the filtered pulse, showing that the longer-wavelength components are contained in the leading edge of the pulse. By numerically back-propagating the retrieved pulse through the filter we generated the incident pulse. The retrieved spectral data (filled circles) and the measured spectrum presented together in Figure 4-5(c), show very good agreement. The temporal pulse data are given in Figure 4-5(d).

Although the sampling step of this data of 20 fs is insufficient to describe the pulse accurately in time, this data was in agreement with an independent autocorrelation measurement, which suggested durations of ~20 fs. The pulses entering the sonogram apparatus are therefore characterised by a small amount of negative linear chirp that we attribute to the extracavity prism sequence described above [6].

Although the laser generated pulses as short as 13 fs when using a 5% output coupler, there was an issue with its long term stability. Because of the very nature of the ring design, a slight misalignment of one component required a re-alignment of all the other components in the ring. The laser required extensive adjustment on a daily basis for optimum operation, which in turn meant the experiments down the line required slight realignment to complement the slight laser reconfigurations. This could be a time consuming task and so, as we will see in Chapter 5, a new approach was taken.

4.3 The Femtosecond PPLN OPO

Research by previous members of the Ultrashort Laser Research Group in St Andrews produced the first femtosecond optical parametric oscillator based on a periodically-poled lithium niobate crystal [13]. The signal and idler outputs, almost continuously tunable from 975 nm to 4.55 μm, were generated by a combination of grating tuning and cavity-length tuning. This posed the question of what would happen if the group velocity dispersion within the cavity were reduced to a near zero value. Would the cavity then support all wavelengths producing very broad-bandwidth pulses and if the pulse duration of the pump pulse could be maintained as it is down-converted to idler wavelengths, then would it be possible to generate few optical cycle pulses? Testing this hypothesis was the motivation for the following research study.

4.4 Optical properties of periodically poled lithium niobate

Lithium niobate ($LiNbO_3$) has a very large transparency range and high nonlinearity making it a key player in the development of new nonlinear sources. It is a negative uniaxial crystal belonging to the crystallographic point group 3m with a rhombohedral space group R3c [14]. The crystal is composed of distorted oxygen octahedra that are slightly rotated one above the others and have one face in common. The oxygen ions are arranged in a hexagonally close-packed fashion in planes perpendicular to the z-axis. Those planes are separated by lithium and niobium ions at interstitial sites and the sequence Nb, vacancy, Li, Nb, vacancy, Li, ... is situated along the crystallographic c axis [15]. See Figure 4-6.

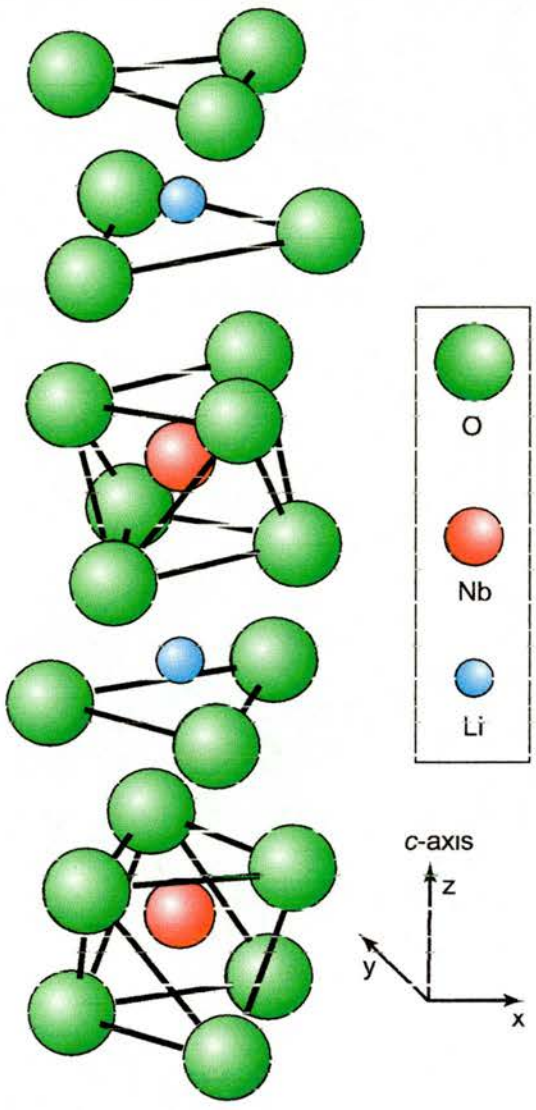

Figure 4-6 The structure of $LiNbO_3$

$LiNbO_3$ is ferroelectric and thus possesses a domain structure where the permanent spontaneous electric field of the domain can be reversed under the influence of an externally applied electric field. The spontaneous polarisation that is present within the crystalline structure means that each ion can take up more than one equilibrium position. In $LiNbO_3$, the displacement of the metal ions from the oxygen layers determines the polarity of a ferroelectric domain. Inversion of the poling direction occurs when the lithium ions are induced to move through the triangular plane of oxygen ions into the adjacent space [15]

as shown in Figure 4-7. A periodically poled crystal of $LiNbO_3$ has a grating period of Λ, comprised of two consecutively inverted domain periods of width $\Lambda/2$.

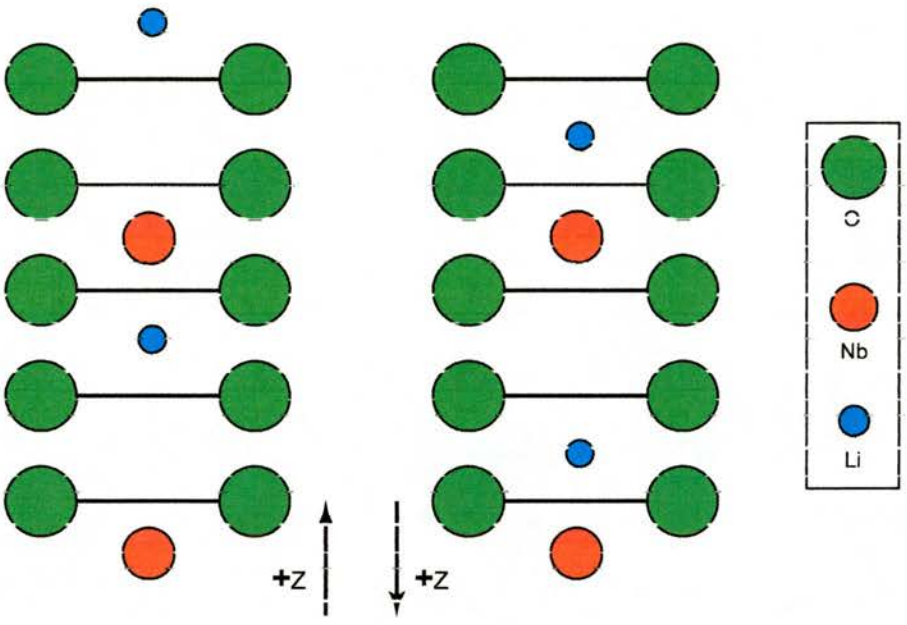

Figure 4-7 Schematic diagram showing the position of the lithium and niobium ions relative to the planes of the oxygen ions for the two different domain polarities in PPLN.

The main optical properties of lithium niobate that are relevant to this work are transparency, refractive index, and optical nonlinearity.

PPLN has a large transparency range, which can be seen from Figure 4-8. It is also clear that PPLN has an extra transmission window that extends to over 7 μm. The transmission characteristics of RTA and KTP are shown for comparison.

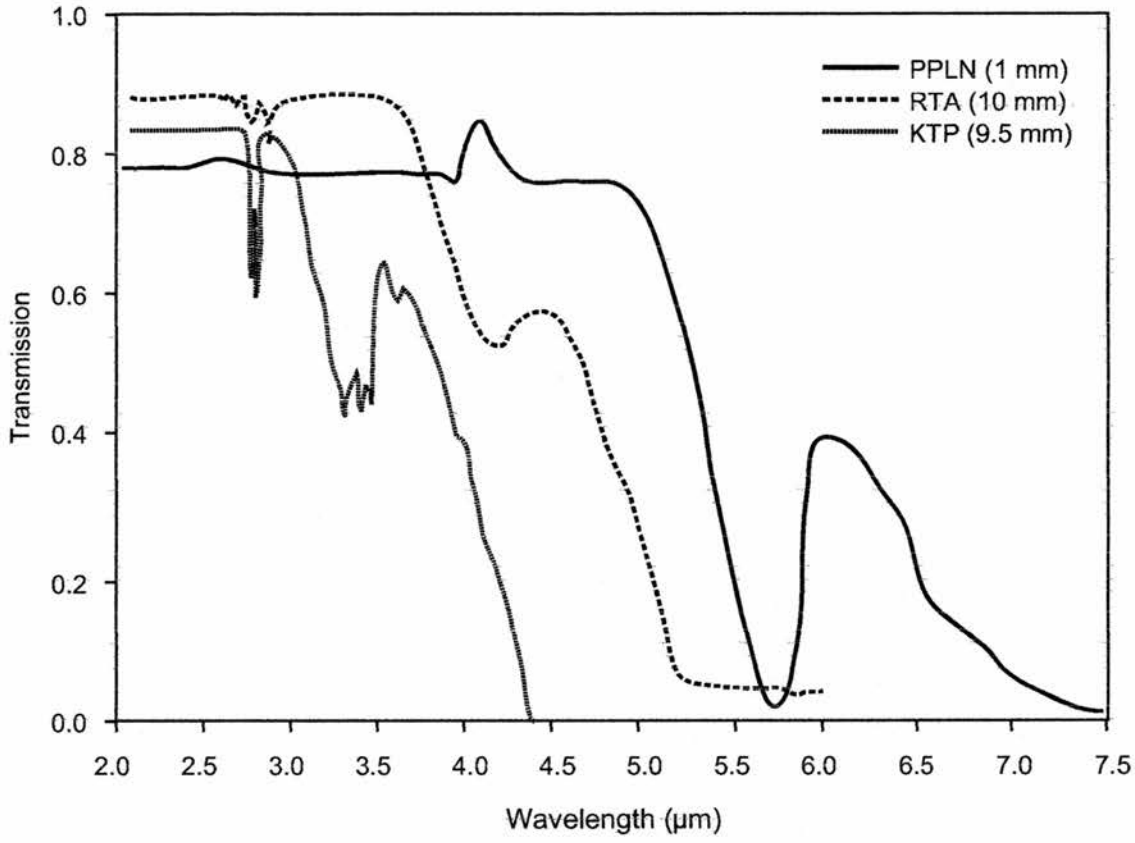

Figure 4-8 Optical transmission characteristics for an extraordinary wave propagating along the x-axis through 1 mm of PPLN. RTA and KTP are shown as comparison. The optical properties of RTA are discussed in more detail in Chapter 5.

Due to the large transparency range, no single set of Sellmeier coefficients can give good agreement of refractive index for all wavelengths. Table 1 shows two sets of Sellmeier coefficients for LiNbO3, the first of which gives better agreement for shorter (visible) wavelengths, while the second is better suited for mid-infrared wavelengths [16-20]. The dispersion data is related by the Sellmeier equation:

$$n_e(\lambda,T)=\sqrt{a_1+b_1T^2+\frac{a_2+b_2T^2}{\lambda^2-\left(a_3+b_3T^2\right)^2}+\frac{a_4+b_4T^2}{\lambda^2-a_5^2}-a_6\lambda^2} \qquad (4.1)$$

where λ is in μm and T is in K.

Sellmeier Coefficient	Visible [19]	Mid-Infrared [18]
a_1	4.5567	5.35583
a_2	0.097	0.100473
a_3	0.201	0.20692
a_4	0	100
a_5	0	11.34927
a_6	2.24×10^{-2}	1.5334×10^{-2}
b_1	2.605×10^{-7}	4.629×10^{-7}
b_2	2.7×10^{-8}	3.862×10^{-8}
b_3	5.4×10^{-8}	-0.89×10^{-8}
b_4	0	2.657×10^{-5}

Table 1 Sellmeier data for lithium niobate

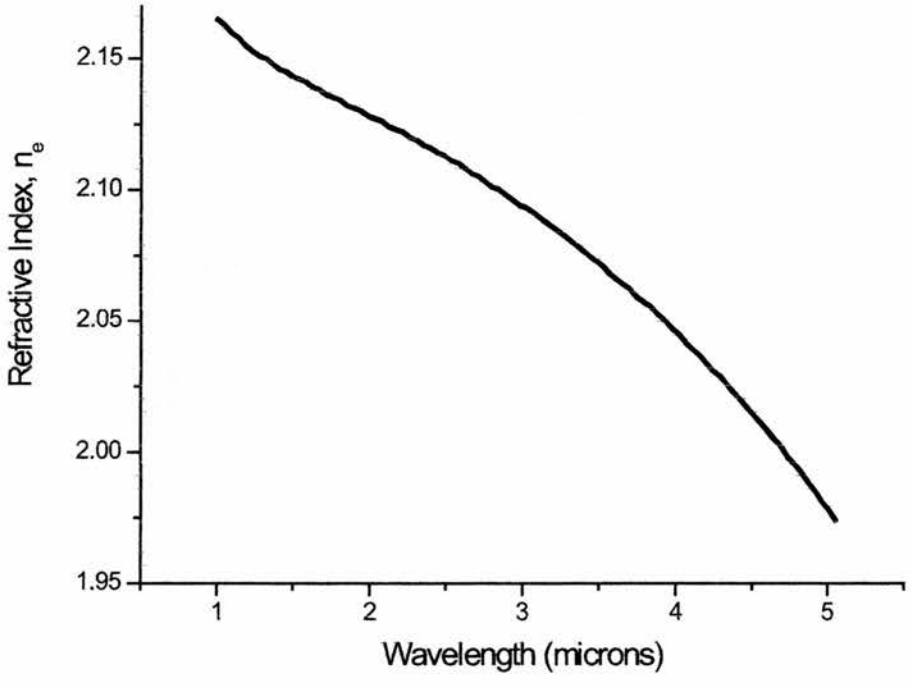

Figure 4-9 Variation of the extraordinary wave refractive index with wavelength in $LiNbO_3$ at a crystal temperature of 100 °C

The crystal symmetry of $LiNbO_3$ results in the following nonlinear optical tensor d_{ij} [14]

$$d_{i,m} = \begin{bmatrix} 0 & 0 & 0 & 0 & d_{31} & -d_{31} \\ -d_{22} & d_{22} & 0 & d_{31} & 0 & 0 \\ d_{31} & d_{31} & d_{33} & 0 & 0 & 0 \end{bmatrix} \quad (4.2)$$

and the nonlinear coefficients are given as:

d_{22}	d_{31}	d_{33}	$d_{eff} = (2/\pi)d_{33}$
2.1	4.3	27	17

Table 2 Birefringent and effective QPM (m=1) nonlinear coefficients shown in pm/V for PPLN [21]

When a QPM process is chosen, the interaction of any combination of polarisations along any crystal is allowed. With PPLN, the poling direction is chosen such that all interacting waves are extraordinary so the largest nonlinear coefficient, d_{33}, will be accessed.

One of the biggest drawbacks of $LiNbO_3$ is a destructive process called photorefractive damage [22]. In a photorefractive material, an incident light beam can cause photo-ionisation. These optically excited free charges scatter through the material towards lower light intensities (outside the beam) which sets up an internal field across the material. This electric field disruption causes localised changes in the material's refractive index that in turn acts to distort the input pulse.

The short pulse, high power work described in this thesis made the PPLN crystals particularly susceptible to photorefractive damage. However, photorefractive effects can be minimised by maintaining the crystal temperature at 100 °C for mid-infrared applications [21].

With the PPLN crystal held at an elevated temperature, its dimensions will expand slightly. The thermal expansion can be described by:

$$l_T = l_{25}\left[1+\alpha(T-25)+\beta(T-25)^2\right] \qquad (4.3)$$

where the thermal expansion coefficients $\alpha = 1.54\times10^{-5}\ \mathrm{K}^{-1}$ and $\beta = 5.3\times10^{-5}\ \mathrm{K}^{-1}$. l_T is the crystal length at temperature T, normalised to the length at 25 °C [23].

4.5 The OPO cavity

Devices based on nonlinear frequency conversion in periodically-poled lithium niobate (PPLN) have become very popular in the past few years. As explained in Chapter 2, PPLN offers particular versatility because of the periodic reversal of the polarity of the nonlinear coefficient which provides the quasi-phasematching. This allows all waves to propagate collinearly along a crystal axis, thus avoiding the drawbacks of Poynting vector walk-off and the associated problems of noncollinear phase matching. In addition to its high gain, PPLN has a relatively large transparency range, which extends from 0.35 μm to ~5 μm. Hence, it can be used for conversion from visible to mid-infrared wavelengths.

The PPLN crystal used in this experiment was supplied by Crystal Technology [24] from a 15 mm long x 0.5 mm thick x 1 mm wide sample of congruent $LiNbO_3$, by patterning 8 photoresist gratings, with periods 20.5 to 22.0 μm onto the +z face, Figure 4-10. It was also coated for anti-reflection (AR) at a

wavelength of 1.1 μm. These gratings were chosen to maximise the range of wavelengths available from the PPLN-OPO when pumped with the Ti:sapphire laser. Grating tuning is implemented by simply translating the grating across the pump beam. Pulse propagation was along the 1 mm wide of the crystal and this was sufficient for optical parametric oscillation to be possible within the limit of the temporal walk away of the interacting pulses.

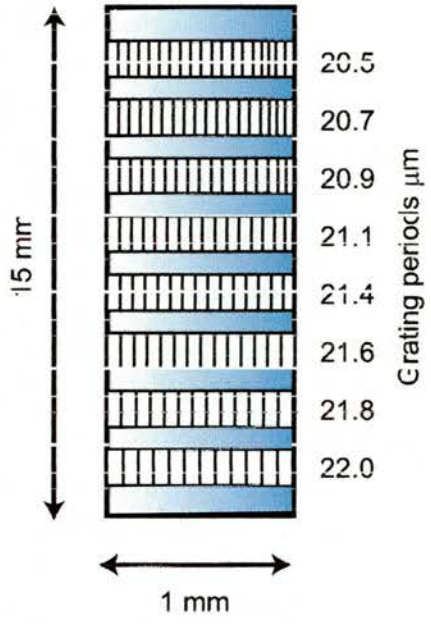

Figure 4-10 Diagram of the PPLN crystal with 8 gratings of periods 20.5 – 22.0 μm

The OPO was configured as a three-mirror cavity. It was period matched to the modelocked Ti:sapphire laser to allow synchronous pumping, giving a round trip period length of 9.2 ns. A diagram of the cavity is illustrated in Figure 4-11.

Unlike previous OPO experiments there was no need for an optical isolator to prevent feedback into the Ti:sapphire laser because any light that is fed back will enter the laser in a direction opposite to that of unidirectional lasing. However, we did find that feedback via the moving mirror could compromise the modelocking, so once modelocked the moving mirror was covered.

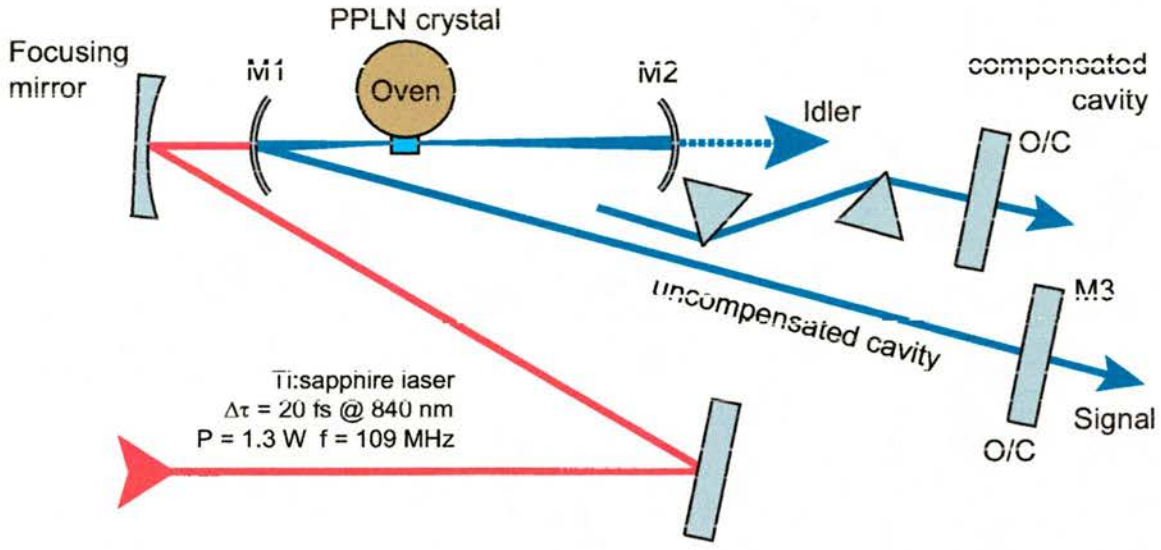

Figure 4-11 Cavity configuration for the PPLN-OPO

Conventionally a lens is used to focus the pump beam into the OPO crystal. However, a design aim for this OPO cavity was to minimise pulse broadening due to material dispersion and so a gold coated curved mirror with 150 mm radius of curvature was used to focus the pump beam. The cavity mirrors, M1 and M2 had 99.98 % reflectivity coatings, centred at 1.115 μm with a bandwidth of ~220 nm, on a 0.5 mm thick CaF_2 substrate with a radius of curvature of 100 mm. Mirror M3, was a 1 % output coupler centred at 1.115 μm on a 0.5 mm thick fused silica substrate. The introduction of material dispersion effects was minimised by using the thinnest possible substrates. CaF_2 substrates were used for the cavity head mirrors (M1 & M2) as CaF_2 is highly transmitting at the idler wavelengths. A fused silica substrate was used for the output coupler M3 as it introduces a minimum amount of third-order dispersion at the signal wavelength.

Previous work [13] had shown that there was significant improvement in performance of a PPLN-OPO if the crystal was heated to around 100°C. This

prevents photorefractive damage and improves the stability of operation [21]. A copper oven mounted on a torlon base was implemented to heat the PPLN crystal, (Figure 4-12), where the heating element was a 150 Ω resistor. This was placed inside the copper block with a good thermal contact. The PPLN crystal was held to the oven by means of a spring-loaded lever that allowed for thermal expansion. The temperature was monitored by a thermocouple mounted within the copper block, and connected to a Marlow Industries [25] temperature controller. It was found that to maintain the crystal temperature at 100°C, the temperature controller had to be set at 150°C. The slight temperature gradient across the crystal was not sufficient to impair the performance of the OPO.

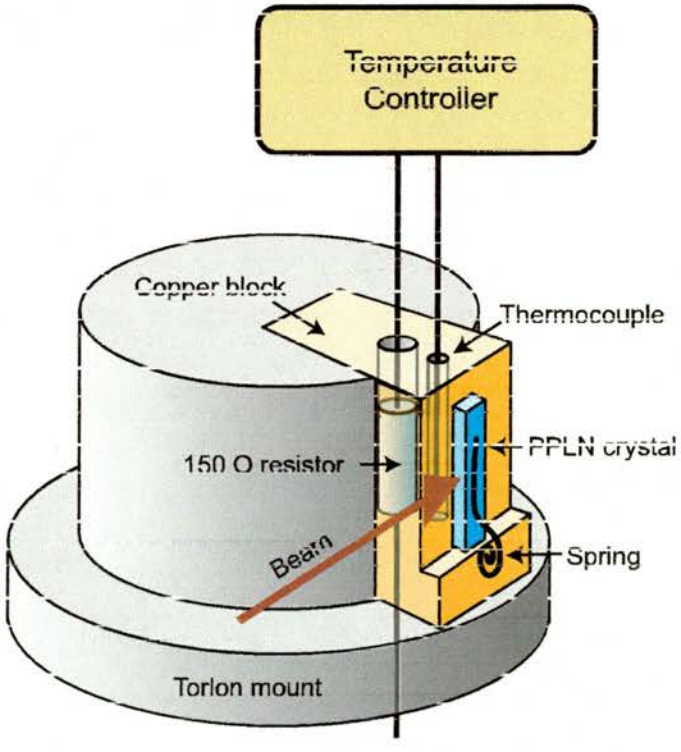

Figure 4-12 Diagram of the oven used to mount the PPLN crystal and maintain it at 100°C

The crystal oven was mounted on an XYZ-translation stage to allow optimum positioning within the stability region between the two curved mirrors. Rotational movement was also provided to align the crystal normal to the incident pump beam. Grating selection was achieved by translating the crystal in the vertical direction. The polarisations of the pump, signal and idler waves were horizontal and were parallel to the poling direction of the crystal.

Alignment of the OPO was achieved by retroreflection of the blue light generated by non-phasematched frequency doubling of the pump beam from the end mirror. The PPLN crystal generated considerable amounts of blue light, which enabled this technique to be implemented easily. Oscillation was then achieved by translation of the end mirror to match the cavity length, and hence the repetition rate, of the Ti:sapphire laser.

Once the OPO was oscillating, it was necessary to compensate for dispersion effects. This was done by inserting a pair of F2 prisms into the long arm of the cavity. The ideal prism apex separation, calculated using appropriate Sellmeier equations [18], was 44.9 cm. The prism material, F2, was chosen because it was suitable for second-order dispersion compensation since it introduced minimum third-order dispersion at the operating wavelength of 1.115 μm [14]. These prisms were configured as shown in the inset of Figure 4-11. Firstly, they were placed beyond the end mirror and the blue frequency-doubled light, which escapes the cavity, was used to find the Brewster angle of the prisms with respect to the bench. The first prism was then placed in the long arm of the cavity at its Brewster angle so that some of the OPO light was redirected by the prism. The second prism was placed at Brewster angle in the path of the redirected OPO light from the first prism. A second end mirror was added at the

correct compensated cavity length and the OPO light from this mirror was sent through a pinhole back along the path it came. The first prism was then moved fully into the beam and oscillation of the uncompensated cavity stops. Oscillation of the compensated cavity was achieved in a similar manner as before by translating the new end mirror.

4.6 PPLN-OPO Results

Changing the cavity length of the PPLN OPO provided a tuning range that extended continuously from 1.045 to 1.190 μm for the signal wave and 2.57 to 3.67 μm for the idler wave. Typical spectra recorded over this range are shown in Figure 4-13 & Figure 4-14. The signal spectra were measured using a Rees Instruments Laser Spectrum Analyser [26] and the idler spectra were measured using a Monolight Spectrum Analyser [27]. It was found that if the average pump power fell below ~1 W the OPO would cease to operate. The most stable operation of the OPO occurred with the 21.57 μm grating, and all of the results included here were taken using this grating.

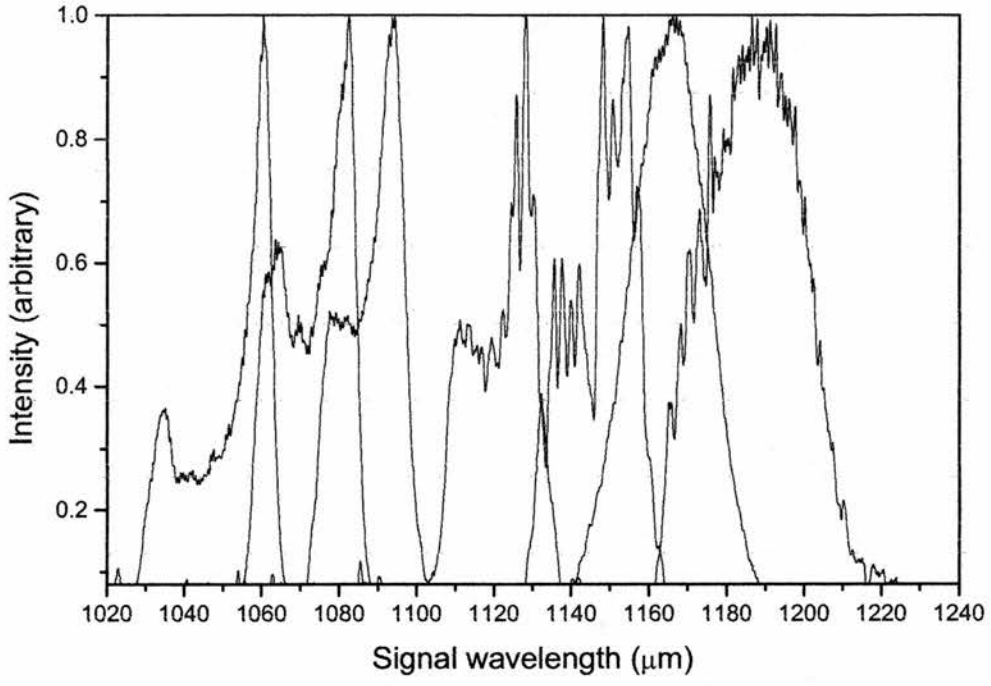

Figure 4-13 Signal spectra illustrating the tuning range of the PPLN OPO. The complete tuning range covered by the signal was 1045 – 1190 nm

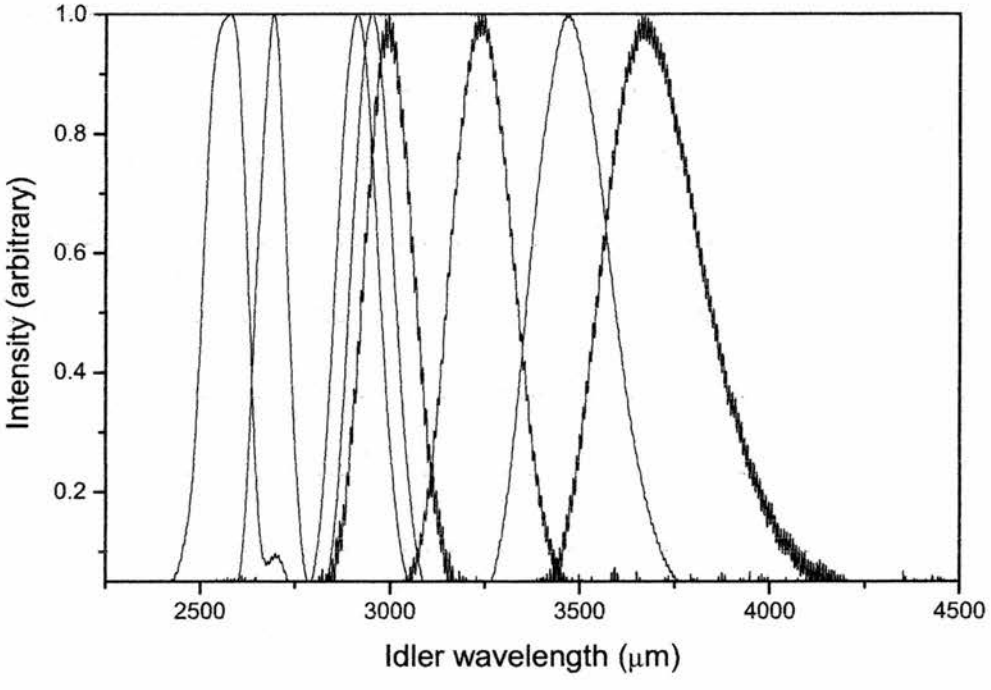

Figure 4-14 Idler spectra illustrating the tuning range of the PPLN OPO. The complete tuning ranges covered by the idler was 2.57 - 3.67 μm.

The F2 prism pair separation was chosen so that the prism glass insertion could be adjusted through the point of minimum intracavity dispersion. This will occur when the second-order dispersion is zero and the third-order is a minimum. The single-pass dispersion can be obtained for the cavity with:

$$\frac{\mathrm{d}^2\phi}{\mathrm{d}\omega^2} = \frac{\lambda^2}{2\pi c^2}\left(\frac{\mathrm{d}\lambda}{\mathrm{d}L}\right)^{-1} \tag{4.4}$$

The tuning rate, $\mathrm{d}\lambda/\mathrm{d}L$, derived experimentally was 0.0073, where L is the length of the standing wave cavity. This implied a single-pass dispersion value of +270 fs^2. The contributed material dispersion of the crystal itself can be calculated from the Sellmeier equations for PPLN, as described in Chapter 2, and was found to be +250 fs^2. This implied some residual cavity dispersion associated with the air and mirrors of +20 fs^2. On approaching the point of minimum intracavity dispersion, the tuning range of the OPO decreased to such an extent that a 20 μm translation of mirror M3 was sufficient to tune through all signal wavelengths. This could be easily observed because the cavity length tuning generated a corresponding variation in the visible light produced by the sum-frequency mixing of the pump and signal waves. While in this configuration the OPO cavity was particularly susceptible to cavity length changes caused by variations in the air density. At times this was sufficient to cause the OPO to drop below threshold.

The maximum idler output power was measured as 6.8 mW at 2.7 μm after mirror M2. The power decreased to less than 1 mW at 3.67 μm. This value includes the unknown loss of power from transmission through the mirror M2. The maximum signal output measured after the 1 % output coupler M3 was 28 mW.

Pulse characterisation was only possible with intracavity dispersion compensation as this offered the most stable operation. A two-photon based autocorrelator using an ultra-bright AlGaAs LED (E_g = 660 nm) detector was used for temporal analysis. An intensity autocorrelation of the signal pulses generated at 1.09 μm is shown in Figure 4-15 with the corresponding spectrum. Unfortunately, the idler power was insufficient to enable successful temporal analysis of these idler pulses.

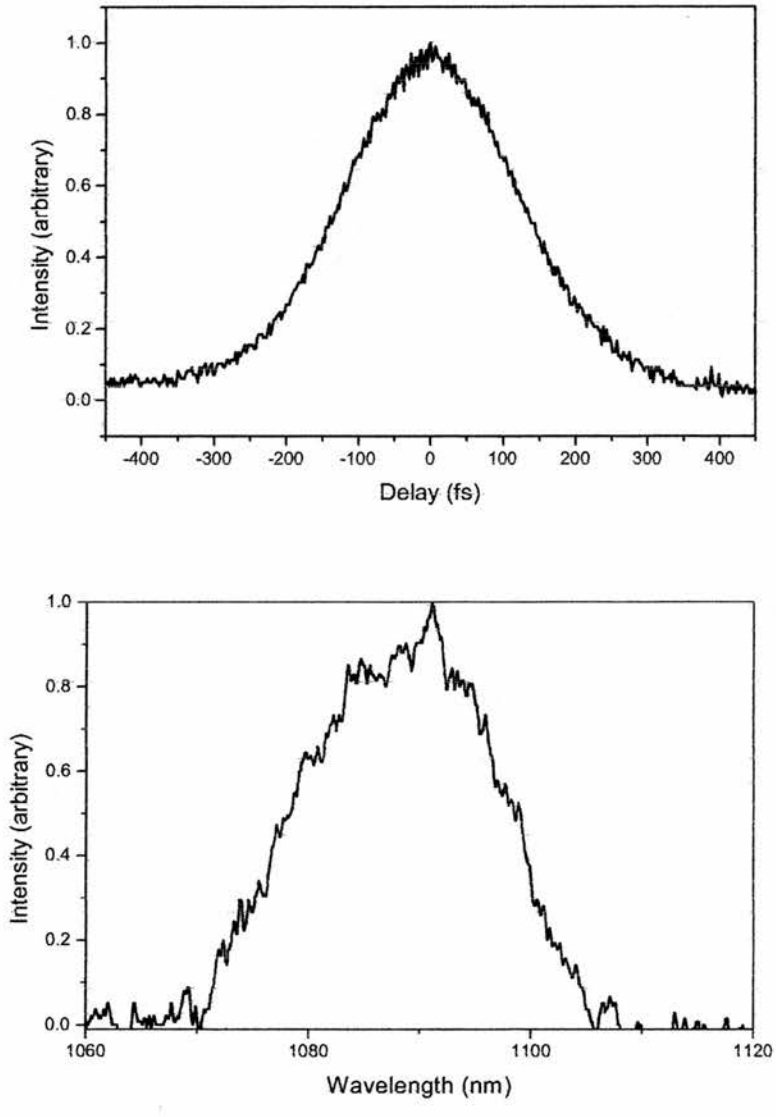

Figure 4-15. Intensity autocorrelation and corresponding spectrum of the signal pulses from the intracavity dispersion-compensated OPO.

The pulse durations inferred from the autocorrelation profile are 175 fs, and the duration-bandwidth product of $\Delta\tau\Delta\nu = 0.95$. This is around three times the transform limit for $sech^2(t)$ pulse-shape pulses . The reason for this is due to the double peaked nature of the signal spectrum of Figure 4-15 which is characteristic of self-phase modulation (SPM) on the output pulse. It is clear that the dispersion compensation within the OPO cavity was insufficient to eliminate SPM effects at around 1.09 μm. However, it can be seen from Figure 4-13, that at the long wavelength limit of the signal tuning range the spectra are of a more characteristic "bell-shape" with a broader bandwidth. This suggests that there may have been shorter or less chirped pulses at these longer signal wavelengths, had there been sufficient output power to characterise them.

The low power demonstrated by this OPO can be attributed to two main causes. The most significant cause is a fundamental limitation experienced by the OPO due to a considerable temporal walk-away effect between the pump, signal and idler pulses. Calculations revealed that the walk-away of typical signal and idler pulses from the pump pulse was as much as +160 fs/mm for the signal and -140 fs/mm for the idler. Pump pulses of ~20 fs duration meant there was a very small length over which the pulses could interact, hence the low gain.

For the other gratings the reason for the low gain of this PPLN-OPO can be found by looking at the theoretical phasematching curve for a 1 mm PPLN crystal at 100 °C, as shown in Figure 4-16. The greyscale shows the variation of the normalised gain coefficient, $sinc^2(\Delta kL/2)$, across the OPO tuning range. Perfect phasematching ($\Delta k = 0$), where the normalised gain is unity, is shown in

black whereas, a gain of zero (ΔkL equals an integer multiple of 2π) is shown in white. The plot was generated for a pump wavelength of 840 nm.

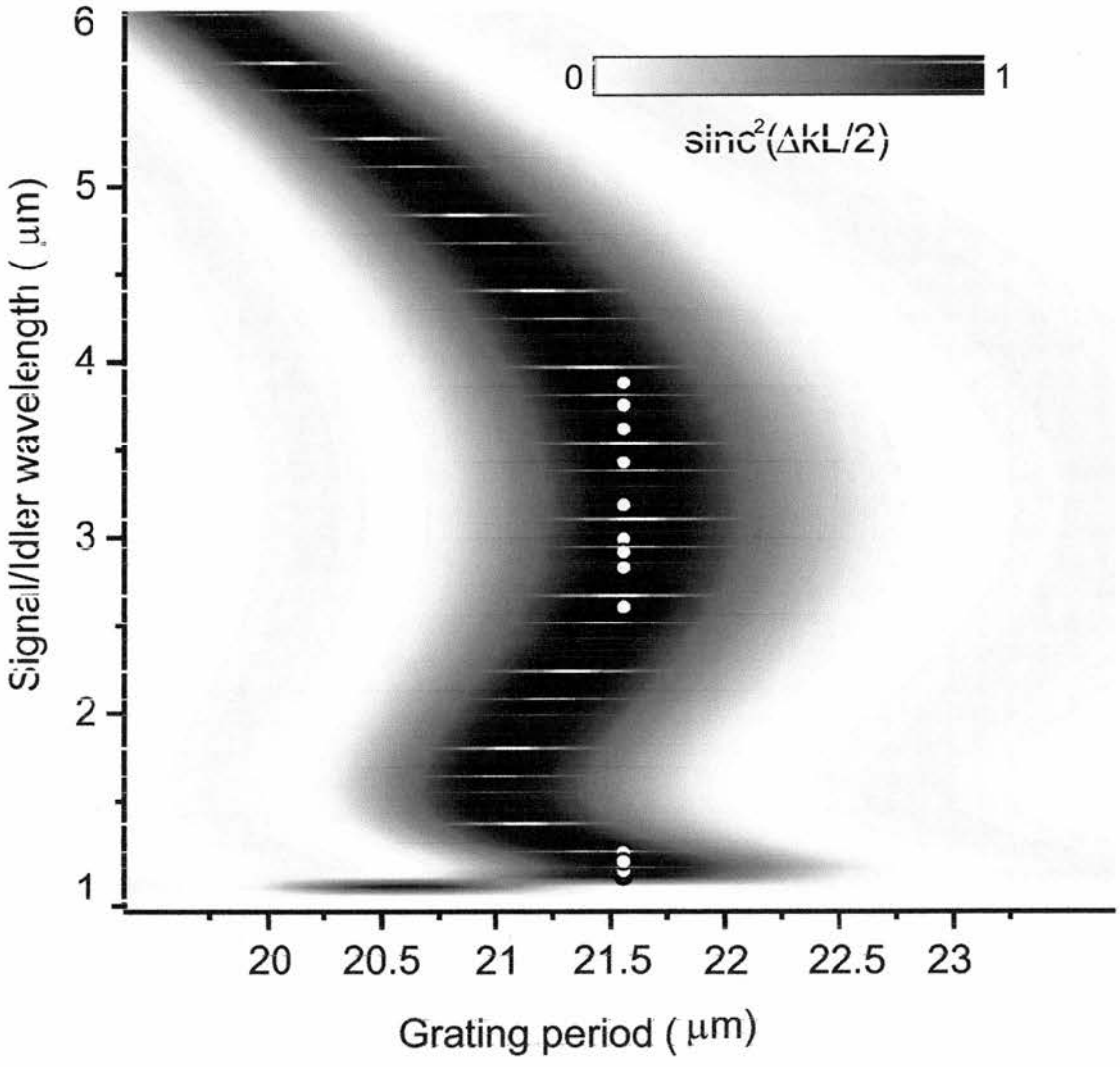

Figure 4-16 Theoretical phasematching curve for a 1 mm PPLN crystal at 100°C and pumped at 840 nm. The points show the tuning range measured on the 21.57 μm grating

The signal and idler results taken on the 21.57 μm grating are superimposed over the phasematching curve and it can be seen that the OPO operated within the highest gain region of the phasematching curve. However, the other crystal gratings (not shown here) would lie away from the region of highest gain.

4.7 Conclusion

Conventional measurements have shown that the Ti:sapphire ring laser produces transform-limited 13-fs pulses with peak powers up to 1 MW. The laser system described here will be suitable as a high-intensity pump source for nonlinear optics and for other applications in which an amplified or a cavity-dumped system was previously necessary.

The relatively new technique of measuring the pulse sonogram provides a simple method for carrying out a complete measurement of the amplitude and phase of any ultrashort pulse, and we have demonstrated its particular suitability to measurement of broad-bandwidth sub-15-fs pulses. The sonogram characterisation technique as described in this thesis has formed the basis for a subsequent PhD project aiming at the development of a 'femtosecond scope' [28].

Although the ring laser could produce excellent results this was at the expense of extensive re-optimisation, often on a daily basis. The very nature of the ring configuration means that it is highly sensitive to misalignment compared to a typical linear cavity, which can be split into two halves either side of the laser head, each of which can be adjusted fairly independently. Although the ring laser was very capable as a pump source and produced results that were interesting in their own right, it was decided that a pump source that produced more predictable and consistent results was necessary for future OPO experiments. In Chapter 5 such a Ti:sapphire laser is described and how it was used as a more reliable pump source for further OPO systems.

In this chapter a PPLN-based OPO has been discussed with modifications to the cavity elements to minimise pulse duration broadening of the pump pulses

during their frequency down-conversion to idler pulses in the mid infrared. It was believed that if the extremely short pump pulse duration could be maintained during its conversion to an idler pulse, then the number of optical cycles within the pulse envelope would be reduced. The results didn't show this. The high peak powers associated with the pump pulse increased the effects of self-phase modulation on the output pulses from the OPO and the extent of the temporal walk-away severely limited the gain of the OPO. A new crystal design which will overcome the problems that arose in this experiment will be described in Chapter 6.

4.8 References

1 G. J. Spuhler, T. Sudmeyer, R. Paschotta, M. Moser *et al.*, "*Passively mode-locked high-power Nd : YAG lasers with multiple laser heads*", Applied Physics B-Lasers and Optics **71,** 19-25 (2000).

2 J. A. der Au, G. J. Spuhler, T. Sudmeyer, R. Paschotta *et al.*, "*16.2-W average power from a diode-pumped femtosecond Yb : YAG thin disk laser*", Optics Letters **25,** 859-861 (2000).

3 J. Aus der Au, S. F. Schaer, R. Paschotta, C. Honninger *et al.*, "*High-power diode-pumped passively mode-locked Yb : YAG lasers*", Optics Letters **24,** 1281-1283 (1999).

4 J. D. Kafka, M. L. Watts, and J. W. Pieterse, "*Synchronously Pumped Optical Parametric Oscillators With Lib3o5*", Journal of the Optical Society of America B-Optical Physics **12,** 2147-2157 (1995).

5 L. Xu, G. Tempea, C. Spielmann, F. Krausz *et al.*, "*Continuous-wave mode-locked Ti : sapphire laser focusable to 5 x 10(13) W/cm(2)*", Optics Letters **23,** 789-791 (1998).

6 T. Beddard, W. Sibbett, D. T. Reid, J. Garduno-Mejia *et al.*, "*High-average-power, 1-MW peak-power self-mode-locked Ti : sapphire oscillator*", Optics Letters **24,** 163-165 (1999).

7 J. Jiang, T. Hasama, Z. G. Zhang, T. Sugaya *et al.*, "*1.25-MW peak-power Kerr-lens mode-locked Ti : sapphire laser with a broadband semiconductor saturable-absorber mirror*", Optics Communications **183,** 159-163 (2000).

8 W. S. Pelouch, P. E. Powers, and C. L. Tang, "*Self-Starting Mode-Locked Ring-Cavity Ti-Sapphire Laser*", Optics Letters **17,** 1581-1583 (1992).

9 D. Georgiev, J. Herrmann, and U. Stamm, "*Cavity Design For Optimum Nonlinear Absorption in Kerr-Lens Mode-Locked Solid-State Lasers*", Optics Communications **92,** 368-375 (1992).

10 D. T. Reid, W. Sibbett, J. M. Dudley, L. P. Barry *et al.*, "*Commercial semiconductor devices for two photon absorption autocorrelation of ultrashort light pulses*", Applied Optics **37,** 8142-8144 (1998).

11 J. L. A. Chilla and O. E. Martinez, "*Direct Determination of the Amplitude and the Phase of Femtosecond Light-Pulses*", Optics Letters **16,** 39-41 (1991).

12 V. Wong and I. A. Walmsley, "*Ultrashort-pulse characterization from dynamic spectrograms by iterative phase retrieval*", Journal of the Optical Society of America B-Optical Physics **14,** 944-949 (1997).

13 C. McGowan, D. T. Reid, Z. E. Penman, M. Ebrahimzadeh *et al.*, "*Femtosecond optical parametric oscillator based on periodically poled lithium niobate*", Journal of the Optical Society of America B-Optical Physics **15,** 694-701 (1998).

14 V. G. Dmitriev, G. G. Gurzadyan, and D. N. Nikogosyan, *Handbook of Nonlinear Optical Crystals*, Second Ed. ed. (Springer-Verlag, Belrin, 1997).

15 M. Houe and P. D. Townsend, "*An Introduction to Methods of Periodic Poling For 2nd-Harmonic Generation*", Journal of Physics D-Applied Physics **28,** 1747-1763 (1995).

16 R. W. Boyd, *Nonlinear Optics* (Academic Press Inc. (California, USA), 1992).

17 G. J. Edwards and M. Lawrence, "*A Temperature-Dependent Dispersion-Equation For Congruently Grown Lithium-Niobate*", Optical and Quantum Electronics **16,** 373-375 (1984).

18 D. H. Jundt, "*Temperature-dependent Sellmeier equation for the index of refraction, n(e), in congruent lithium niobate*", Optics Letters **22,** 1553-1555 (1997).

19 M. V. Hobden and J. Warner, Physics Letters **22,** 243 (1966).

20 R. A. Andrews, IEEE Journal of Quantum Electronics **6,** 68 (1970).

21 L. E. Myers, R. C. Eckardt, M. M. Fejer, R. L. Byer *et al.*, "*Quasi-Phase-Matched Optical Parametric Oscillators in Bulk Periodically Poled Linbo3*", Journal of the Optical Society of America B-Optical Physics **12,** 2102-2116 (1995).

22 G. E. Peterson, A. M. Glass, and T. J. Negran, "*Control of the susceptability of lithium niobate to laser induced refractive index changing*", Applied Physics Letters **19,** 130 (1971).

23 Y. S. Kim and R. T. Smith, Journal of Applied Physics **40,** 4637 (1969).

24 Crystal Technology Inc, (1040 E. Meadow Cir., Palo Alto, CA 94303, USA).

25 Marlow Industries, (7 Laura House, Jengers Mead, Billinghurst, West Sussex, RH14 9NZ).

26 Rees Instruments Ltd, (Thornbrook, Weyside Park, Cattleshall Lane, Godalming, Surrey, GU7 1XE).

27 Macam Photometrics Ltd, (10 Kelvin Square, Livingstonm, EH54 5PF).

28 I. G. Cormack, W. Sibbett, and D. T. Reid, "*Practical measurement of femtosecond optical pulses using time- resolved optical gating*", Optics Communications **194,** 415-424 (2001).

Chapter 5

Standing-wave Ti:sapphire Laser and RTA-OPO

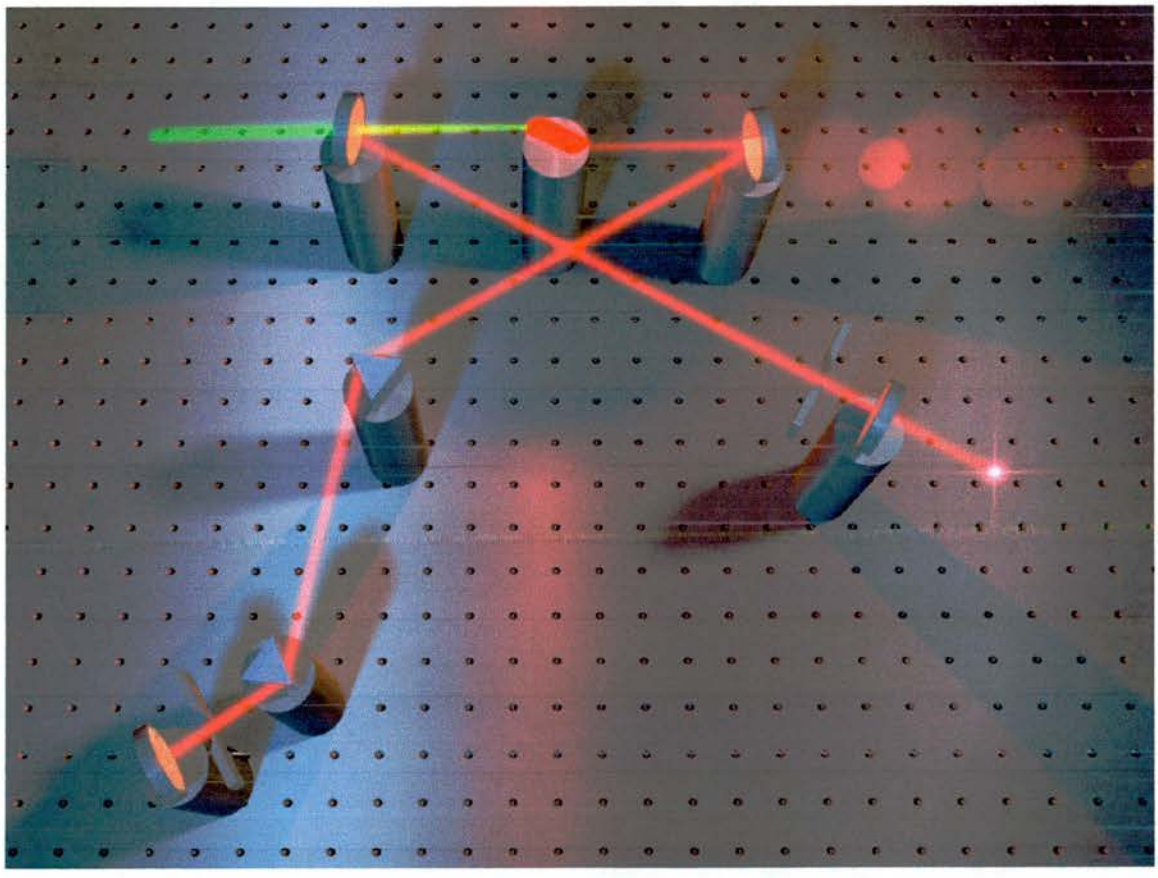

Artistic visualisation of a linear Ti:sapphire cavity

In Chapter 4 a number of problems where identified when trying to produce few-optical-cycle pulses in the mid-infrared using a PPLN-OPO pumped by a megawatt femtosecond Ti:sapphire ring laser. The combination of laser stability problems and temporal walk-away effects posed a serious restriction on the duration and quality of the pulses obtained. It was decided that a new approach was needed and the Ti:sapphire ring laser was rebuilt as a standing-wave (linear) cavity design and the PPLN based OPO was replaced by a periodically-poled rubidium titanyl arsenate (PPRTA) based OPO.

As will be seen, changing to a linear cavity design for the pump laser gave it much greater stability, at the cost of doubling the duration of the shortest achievable pulse, and the PPRTA OPO enabled the generation of mid-infrared pulse bandwidths exceeding 500 nm!

5 Linear cavity Ti:sapphire laser

Although the ring laser described previously generated 13 fs pulses, the shortest so far reported for a laser using only standard 'off-the-shelf' components, and at megawatt peak powers, its Achilles heel was the lack of long-term stability. Because of the very nature of the ring design, a slight misalignment of one component required re-alignment of all the other components in the ring. The ring laser required extensive tweaking on a daily basis for optimum operation, which in turn meant that the OPO then required slight realignment to complement the slight laser reconfigurations. This could sometimes take the majority of the day, and so it was decided that a new approach was needed.

5.1 The linear cavity design

The linear cavity is a proven design and is widely use in femtosecond-laser laboratories, Figure 5-1. The cavity head remained the same as that for the ring laser with the 10 mm Ti:sapphire crystal placed between two curved mirrors with radius of curvature of -100 mm placed ~49 mm from each crystal end. As before, the 10 W Millennia X pump beam at 532 nm was focused into the laser head with a 100 mm focal length lens. The full fold angle of the two arms of the cavity was 22°, the longest of which was 100 cm while the other was 60 cm. The long arm was also folded so that it could fit in the bench space and it contained two fused silica prisms separated by 85 cm for dispersion compensation. The shorter arm lead to a 10% output coupler and contained a horizontal slit which acted as a 'hard aperture' to favour modelocked operation.

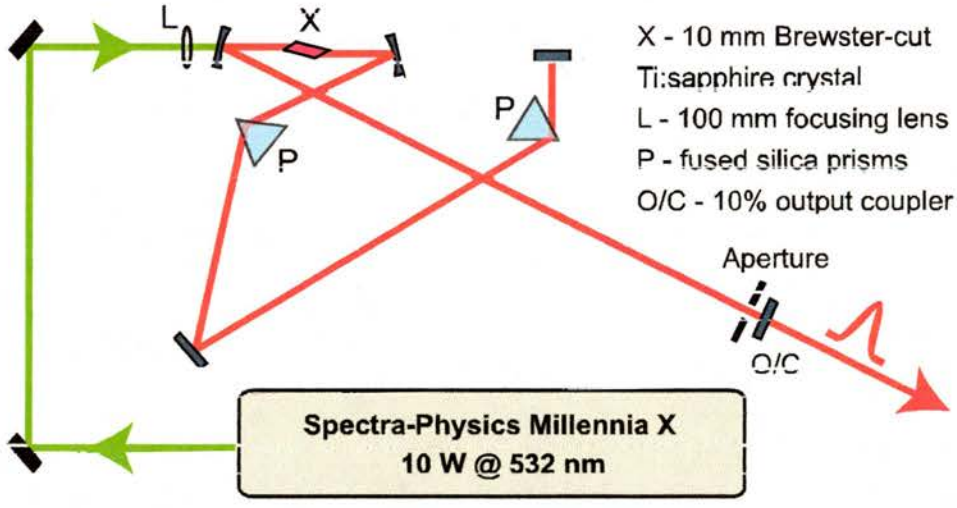

Figure 5-1 Femtosecond Ti:sapphire laser with linear cavity

Extra-cavity dispersion compensation was included in the form of two pairs of fused silica prisms (with an apex separation of 64 cm) which were necessary to remove the frequency chirp acquired by the pump pulse after passing through

the 7 mm thick BK7 output coupler. Variation of these prism insertions also provided a way of pre-chirping the pump pulses, which formed an important feature for the experiments described in Chapter 6.

A typical spectrum and interferometric autocorrelation of this laser are shown in Figure 5-2. The centre wavelength of the output could be tuned from 810 – 850 nm. For this experiment the PPRTA OPO required pulses centred at 830 nm, which corresponded to 25 fs in duration with an average power ~1.1 W. While running in CW operation, the laser could produce output powers of up to 1.5 W. The repetition rate of the cavity was measured with a RF spectrum analyser to be 84.5 MHz, which corresponds to a cavity length of 1.775 m.

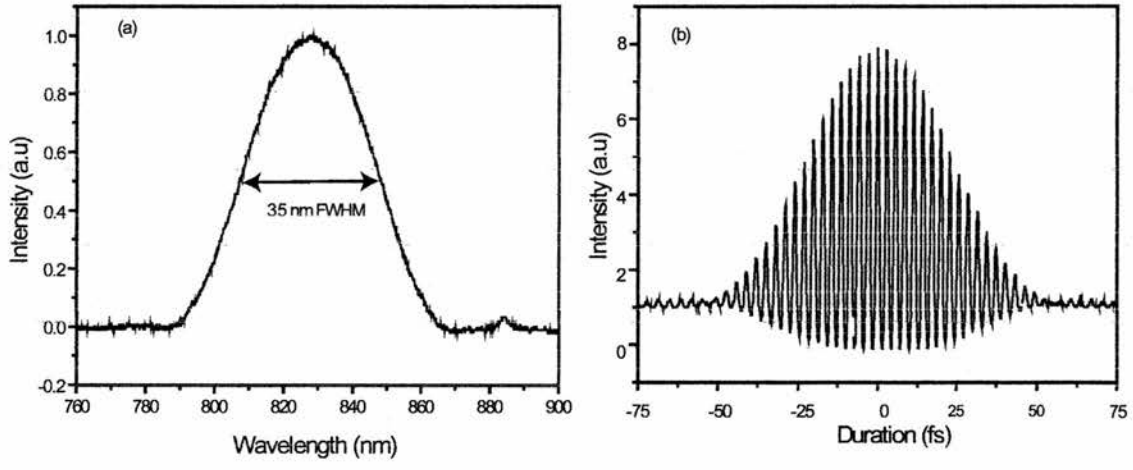

Figure 5-2 Typical wavelength spectrum (a), and interferometric autocorrelation (b), of the output from the linear Ti:sapphire laser cavity. The inferred pulse duration is ~25 fs.

The time-bandwidth product of 0.34 for these pulses is close to the transform limit of 0.315 for a $sech^2(t)$ pulse profile. Pulse bandwidths of up to 50 nm were obtainable; but at these enlarged bandwidths the output pulses were highly chirped.

This laser provided a much greater operating stability than the ring design and would need hardly any optimisation on a day-to-day basis. One of the initial

concerns with the linear cavity was optical feedback from the OPO. The common solution to prevent feedback into the laser cavity is use an optical isolator, but when dealing with femtosecond pulses such isolators produce significant dispersion which broaden the pulses. Fortunately, it was found that with very careful alignment it was possible to prevent optical feedback without needing an isolator.

5.2 The mid-infrared periodically poled RTA OPO

The titanyl arsenates, $RbTiOAsO_4$ (RTA) in particular, have been used widely in bulk crystal form for Ti:sapphire pumped femtosecond OPOs [1-4] because of their good crystal quality, high nonlinear coefficients, and broad phase-matching ranges. The first periodically poled RTA based OPO was demonstrated in 1997 by Reid *et al.* [3] where previously quasi-phasematched OPOs had relied exclusively on PPLN crystals.

PPLN suffers from a number of issues such as large thermal effects, photorefraction, and limited aperture size. In contrast to PPLN the PPRTA crystal is not prone to photorefractive effects or thermal damage unlike PPLN so can operate at room temperature, thereby eliminating the inconvenience of having an oven in the cavity. RTA is characterised by a relatively low coercive field, highly anisotropic structure and low temperature dependence, which permits it to be fabricated by periodic poling into large-aperture devices suitable for higher-power applications.

5.2.1 Optical properties of PPRTA

The titanyl arsenates are an isomorphic family of compounds characterised by the formula unit **M**TiO**X**O_4, where **M** can be K, Rb or Cs and **X** can be P or As [5]. From this, the available family members are KTP, RTP, KTA, RTA and CTA. All of these crystals are positively birefringent, orthorhombic and belong to the crystallographic point group *mm2*. The structure of a titanyl arsenate (Figure 5-3) is noncentrosymmetric and is characterised by chains of TiO_6 octahedra, linked at two corners and separated by XO_4 tetrahedra [6].

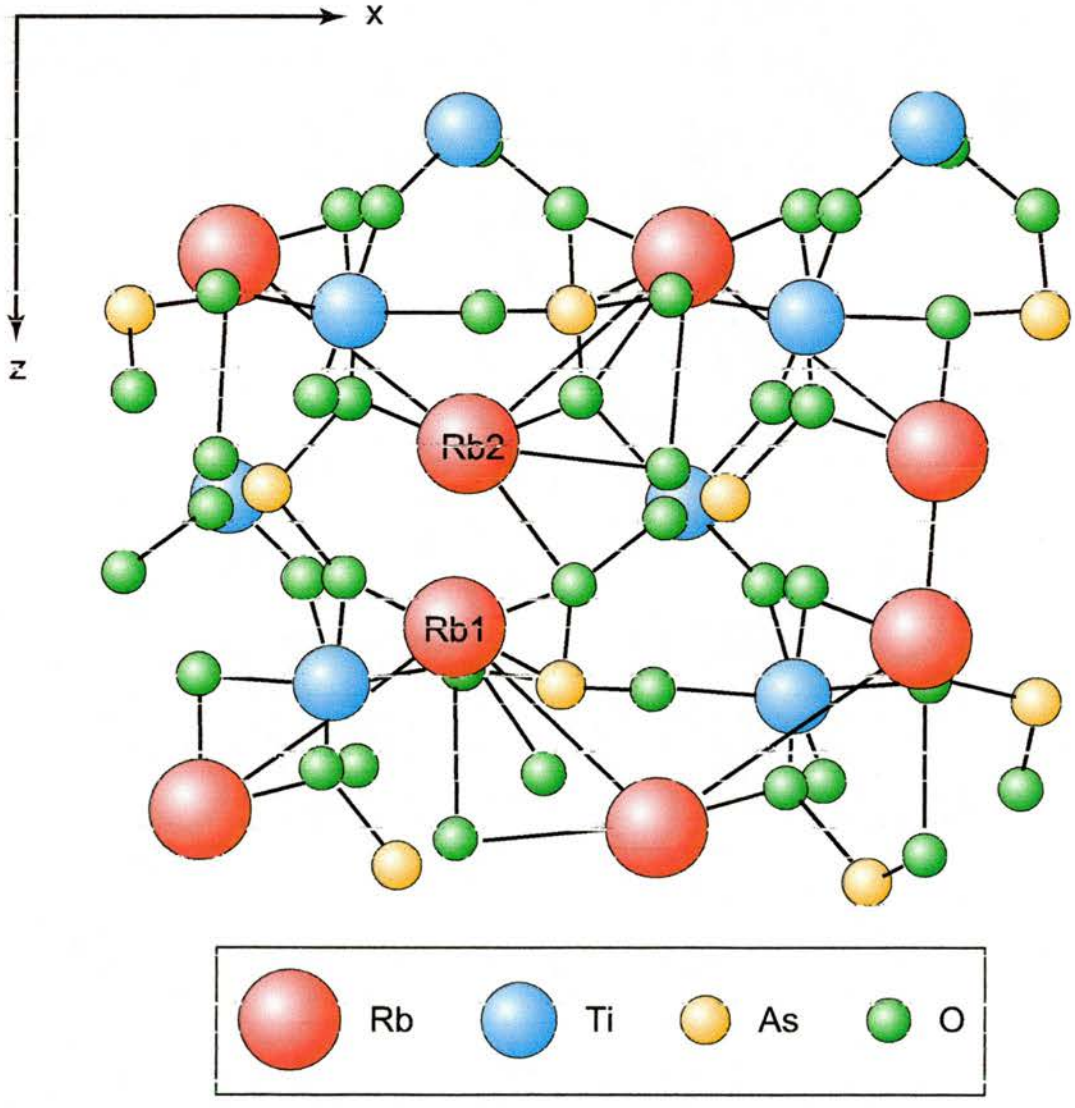

Figure 5-3 The $RbTiOAsO_4$ crystal structure viewed along [010]

A net z-directed polarisation results from the alternating long and short Ti-O bonds on the octahedral chains. These bonds contribute to the materials nonlinear and electro-optic coefficients and are responsible for the ferroelectric properties.

The optical transmission data for RTA, KTP and for comparison, PPLN, are shown in Figure 5-4. The absorption bands in the RTA and KTP traces at 2.8 μm most likely represent OH stretching bands.

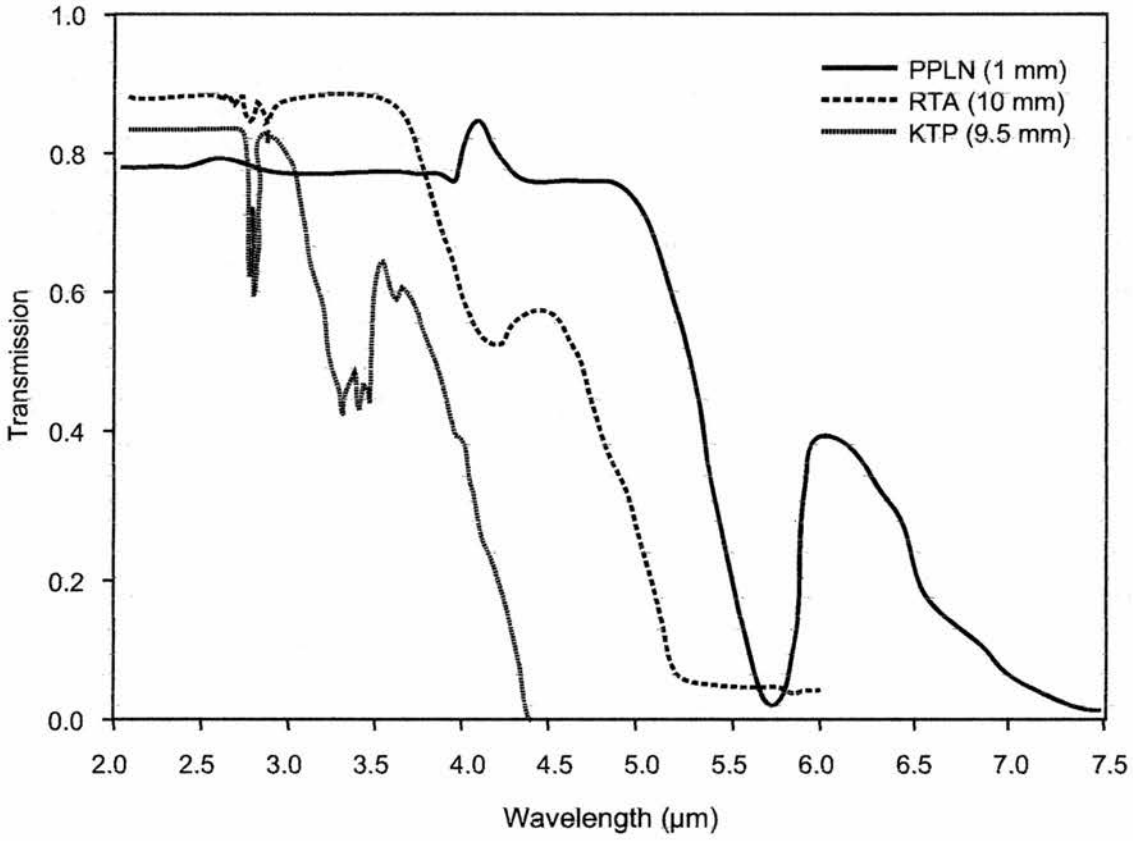

Figure 5-4 Infrared transmission of uncoated KTP, RTA and PPLN crystals [7].

The variation of the ordinary and extraordinary refractive indices with wavelength for RTA is shown in Figure 5-5.

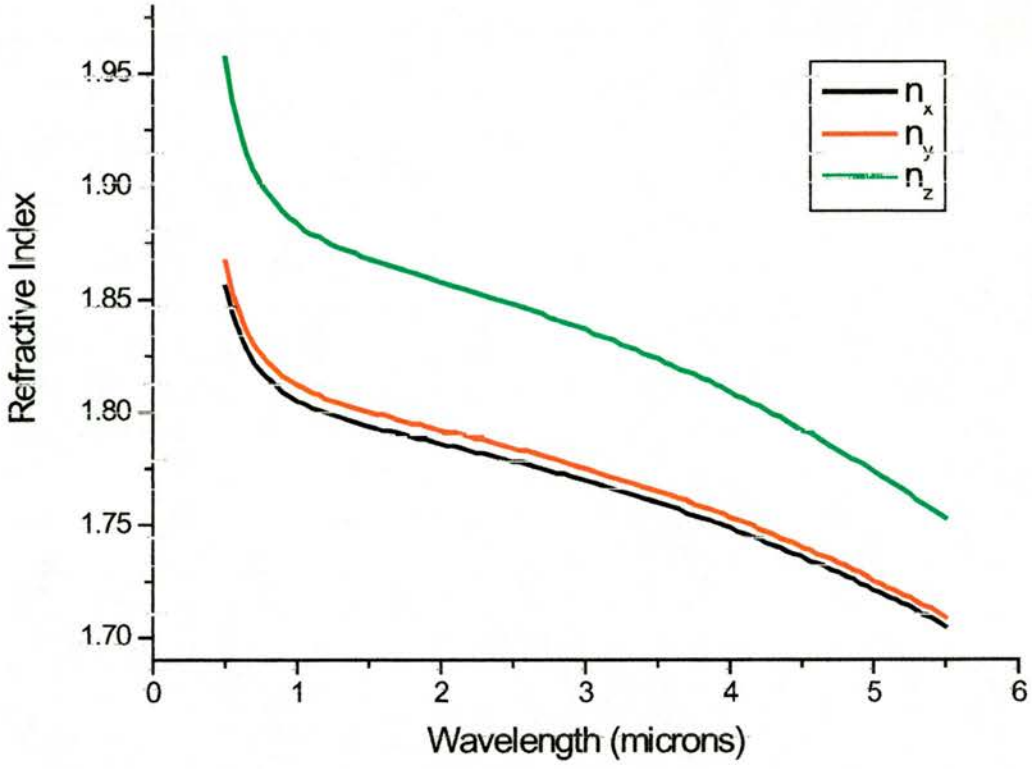

Figure 5-5 The variation of refractive index with wavelength in RTA.

The Sellmeier equation (5.1) used to derive the refractive indices of RTA is given below. The Sellmeier coefficients are taken from the results of Fenimore et al. [7] and are shown in Table 1.

$$n(\lambda) = \sqrt{A + \frac{B}{1 - \left(\frac{C}{\lambda}\right)^2} - D\lambda^2} \qquad (5.1)$$

Sellmeier Coefficient	A	B	C	D
n_x	2.04207	1.17785	0.20157	0.01035
n_y	2.14941	1.09267	0.21462	0.01067
$n_z(n_e)$	2.18962	1.30103	0.22809	0.01390

Table 1 Sellmeier coefficients of RTA [7]

The crystal symmetry of RTA results in the following nonlinear matrix:

$$d_{i,m} = \begin{pmatrix} 0 & 0 & 0 & 0 & d_{15} & 0 \\ 0 & 0 & 0 & d_{24} & 0 & 0 \\ d_{31} & d_{32} & d_{33} & 0 & 0 & 0 \end{pmatrix} \quad (5.2)$$

and the coefficient values are shown in Table 2.

d_{31}	d_{32}	d_{33}	d_{24}	d_{15}	$d_{eff} = (2/\pi)d_{33}$
2.3	3.8	15.8	0	0	~10.0

Table 2 Birefringent and effective QPM (m=1) nonlinear coefficients shown in pm/V for RTA [8]

In RTA, the d_{33} nonlinear coefficient is much greater than the other coefficients and can only be accessed by a quasi-phasematching process, for which a relatively large effective nonlinear coefficient of d_{eff} ~ 10 pm/V is obtained.

5.2.2 The PPRTA-OPO experimental setup

The PPRTA crystal used in this experiment was fabricated by the Institute of Optical Research [9] from a 8 x 1 mm sample by patterning a photoresist grating with a period of 30 μm on to the c+ face. The sample was then cut down to obtain a 2 mm long crystal, the end faces were polished and antireflection coated for a centre wavelength of 1.1 μm. An illustration of the crystal orientation is shown in Figure 5-6.

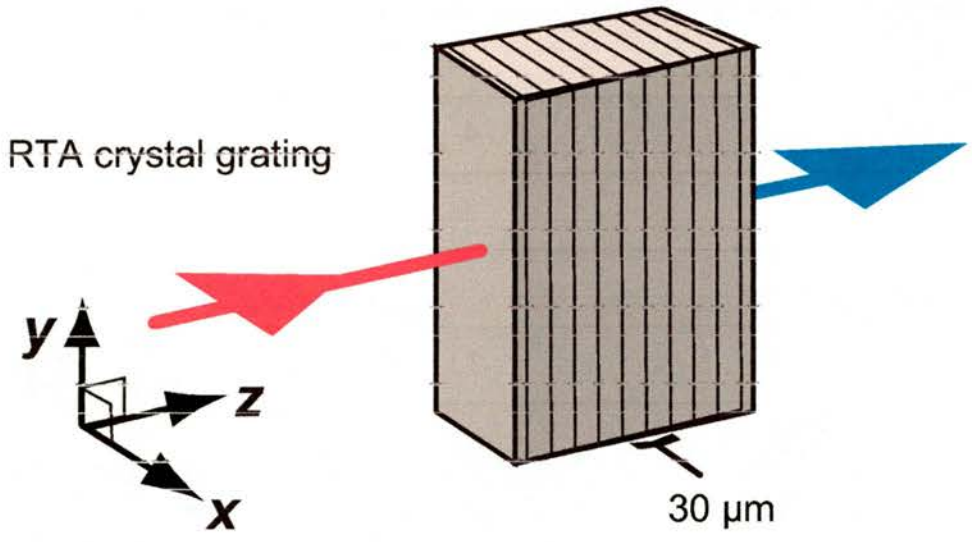

Figure 5-6 Illustration of the PPRTA structure with a 30 μm grating period.

The PPRTA crystal was configured in a singly-resonant four-mirror standing-wave X-cavity femtosecond OPO (Figure 5-7), pumped by the Ti:sapphire laser described in Section 5.1. Because PPRTA is not subject to photorefractive damage at room temperature, the crystal was mounted without need for temperature regulation.

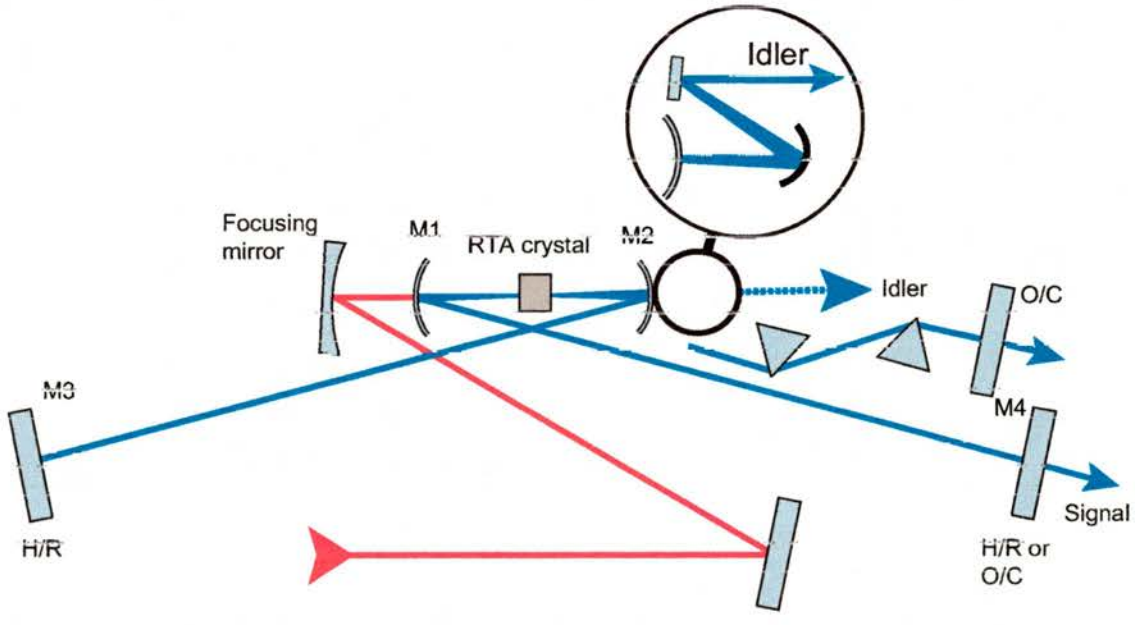

Figure 5-7 Cavity configuration of the PPRTA OPO. The F2 prism sequence is also shown for the configuration when the OPO operated with dispersion compensation. The inset at the idler output illustrates the use of a curved mirror (instead of a lens) to collimate the output beam.

As described in Chapter 4, a gold-coated curved mirror with 150 mm radius of curvature was used to focus the pump beam. All cavity mirrors had 99.98% reflectivity coatings centred at 1.115 μm with a bandwidth of ~220 nm, on a 0.5 mm thick CaF_2 substrate. The cavity head mirrors, M1 & M2, had a 100 mm radius of curvature and because of their CaF_2 substrate; they were highly transmitting at idler wavelengths. The 1% output coupler (mirror M4) had the same reflectivity characteristics as the other mirrors but used a 0.5 mm fused silica substrate as this introduced minimum third-order dispersion at the signal wavelength.

5.2.3 PPRTA-OPO results

The first configuration of the OPO that was assessed did not include any intra-cavity dispersion compensation. The pump threshold was measured as ~340 mW when including losses at the pump focussing mirror and cavity mirror M1. The pump depletion in the PPRTA crystal was calculated by measuring the ratio of idler output power after mirror M2 with and without OPO oscillation. This corresponded to a 4% pump depletion. The crystal loss was calculated by measuring the ratio of the pump power after mirror M2 with and without passage through the crystal. The crystal loss was measured as 13%.

Changing the cavity length produced a tuning range that extended continuously from 1.08 to 1.21 μm for the signal pulses and over a micron for the idler pulses from 2.71 to 3.78 μm. Typical spectra recorded over this range are shown in Figure 5-8 & Figure 5-9. The signal spectra were measured using a Rees Instruments Laser Spectrum Analyser [10] and the idler spectra were measured with a Monolight Spectrum Analyser [11].

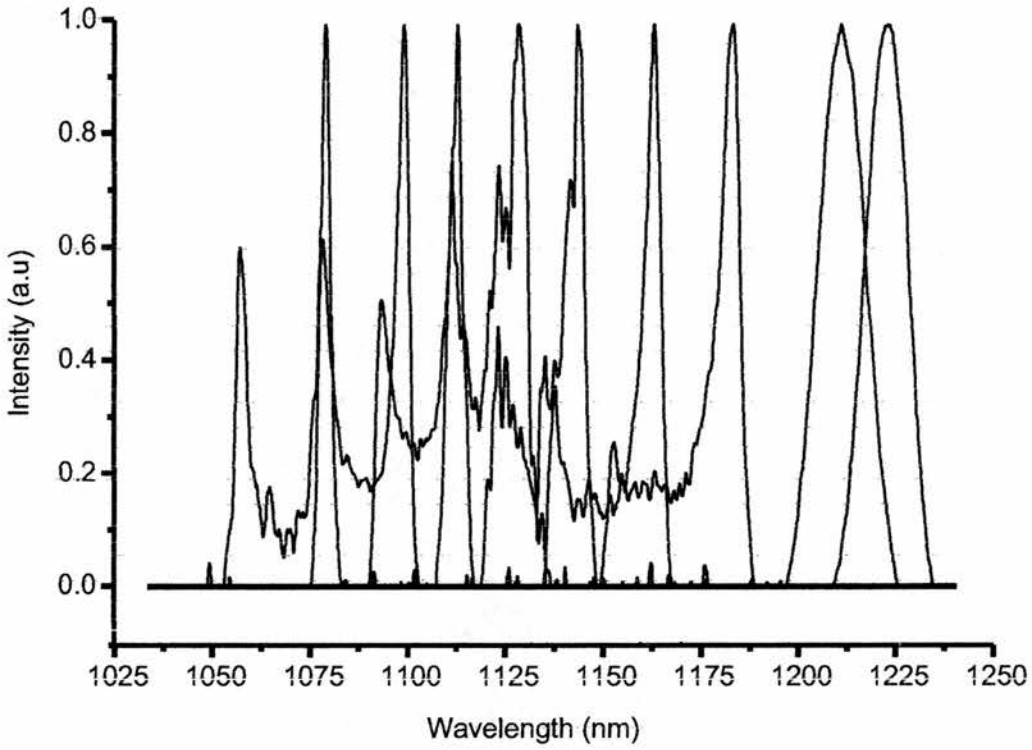

Figure 5-8 Sample of signal spectra across the tuning range of the non dispersion-compensated PPRTA cavity. The complete wavelength range of the signal was 1.08 - 1.21 μm

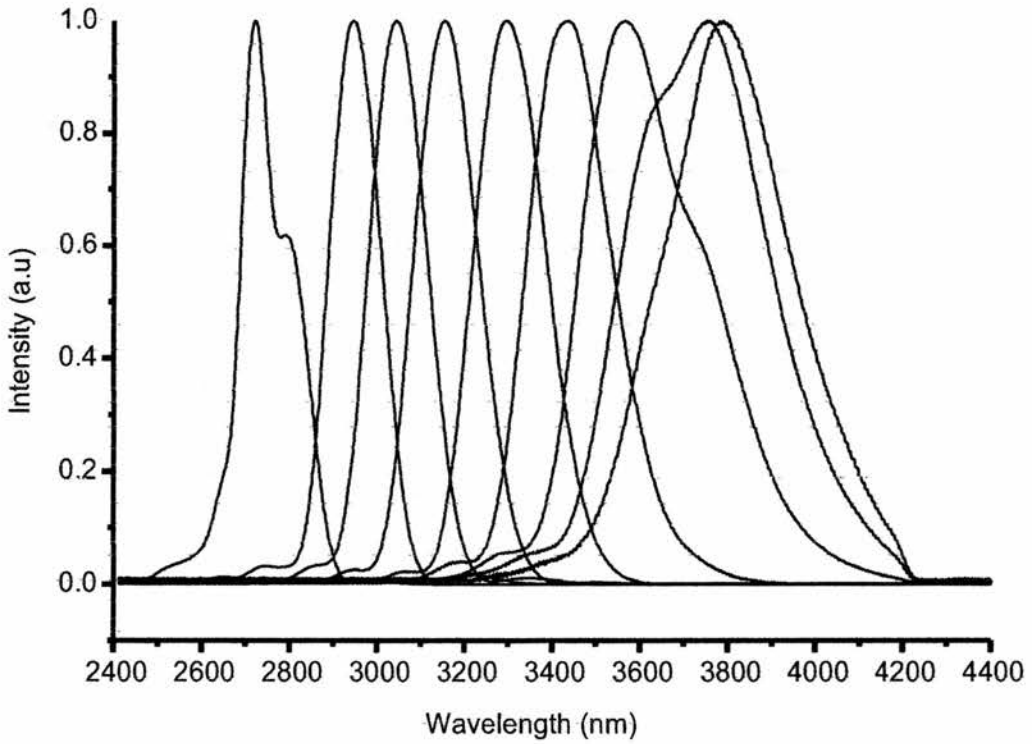

Figure 5-9 Sample of idler spectra across the tuning range of the non dispersion-compensated PPRTA cavity. The complete wavelength range of the idler was 2.71 – 3.78 μm

The idler output power, as measured after the collimating optics beyond mirror M2, dropped from 3.5 mW for the shortest idler (longest signal wavelengths) down to 0.5 mW for the longest idler wavelengths.

Temporal measurement of the signal pulses was achieved with a two-photon based autocorrelator using an ultra-bright AlGaAs LED (E_g = 660 nm) detector. Silver-coated mirrors were used in the autocorrelator for optimum reflectivity at the signal wavelengths and a -50 mm radius of curvature mirror was used to focus the autocorrelator output onto the LED detector. The 50% beam splitter of the autocorrelator was 0.5 mm thick with a fused silica substrate to minimise dispersion. Another autocorrelator was setup for the temporal analysis of the idler pulses. This was based on an InGaAs photodiode (Hamamatsu G5852-01) and used gold-coated mirrors for minimum loss at mid-infrared wavelengths. The 50% beam splitter was on a 1 mm thick CaF_2 substrate and an -80 mm radius of curvature mirror was used to focus the idler beam onto the detector. Alignment of the idler autocorrelator proved to be a very difficult task as there was no easy way to trace the beam path (unlike the signal autocorrelator where an IR detector card was used) and the because power was so low. A lead selenide detector was used in conjunction with a beam chopper to provide rough alignment of the two idler beams at the output of the autocorrelator, after that a great deal of time was spent tweaking to find the optimum focus and beam overlap until eventually a two-photon signal could be recorded.

Signal autocorrelation measurements were only possible for signal wavelengths of 1.2 μm. If the OPO was tuned to shorter signal wavelengths then disruptive instabilities in the signal wavelength arose. Examination of the spectra in Figure 5-8 indicates that at shorter wavelengths the spectra splits into two peaks,

which is characteristic of substantial self-phase modulation (SPM) within the signal wave. This caused random fluctuations in the centre wavelength of up to 50 nm, which made signal autocorrelation of these pulses impossible.

The signal SPM did not perturb the idler, and autocorrelations up to 3.4 μm were possible. A representative idler spectrum and corresponding autocorrelation for the shortest idler pulses produced from the uncompensated PPRTA OPO are shown in Figure 5-10. These pulses were centred at 3.19 μm with 175 nm FWHM bandwidth and from the autocorrelation, and assuming a Gaussian intensity profile, had a duration of 110 fs or ~10 optical cycles. The time-bandwidth-product of these pulses was 0.57, almost 30% greater than the Gaussian ideal of 0.44. This suggests the presence of chirp, which was most likely introduced by the 1.5 mm of CaF_2 substrate in mirror M2, and the autocorrelators beam splitter as well as a contribution by the germanium filter used to prevent non-idler wavelengths entering the autocorrelator.

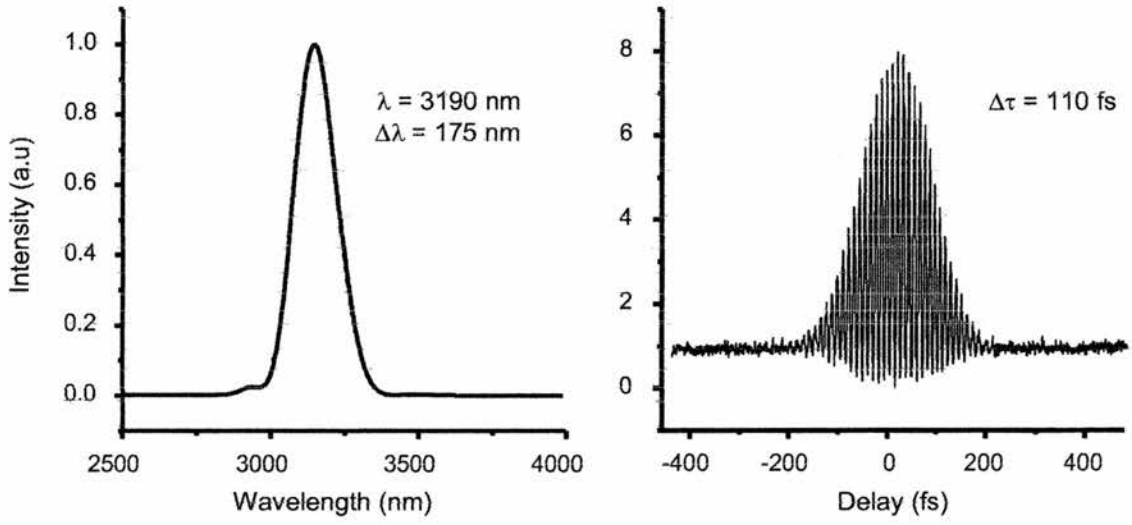

Figure 5-10 Idler spectra and interferometric autocorrelation of the shortest mid-infrared pulses generated from the uncompensated PPRTA OPO.

When measuring the idler pulses having wavelengths centred at greater than 3.4 μm, the power was so low (less than 0.5 mW) and the upper limit in the optical response of the InGaAs photodiode was reached such that no further idler autocorrelations could be recorded. This was frustrating as the pulses centred around 3.8 μm had much larger bandwidths of up to 400 nm FWHM (Figure 5-9). Assuming a transform limited Gaussian pulse profile, the bandwidth of these pulses was broad enough to support ~55 fs pulses which would correspond to just ~4 optical cycles!

Once the uncompensated PPRTA OPO had been characterised, dispersion compensation was introduced in the form of two intra-cavity F2 prisms with an apex separation of 26 cm, (see Figure 5-7). This immediately improved the wavelength stability of the signal pulse thus enabling a full set of autocorrelations to be obtained for the complete tuning range of both the signal and idler waves. The tuning range was similar to before; 1.08 to 1.21 μm for the signal (Figure 5-11) and 2.70 to 3.67 μm for the idler (Figure 5-12).

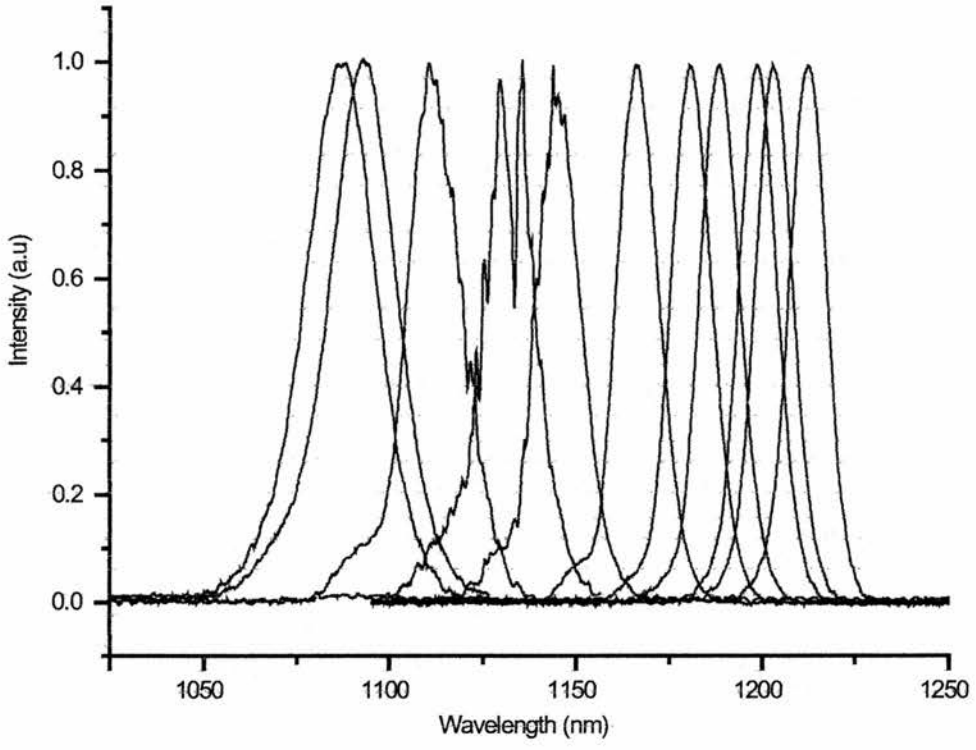

Figure 5-11 Sample of signal spectra across the tuning range of the dispersion-compensated PPRTA cavity. The wavelength range of the signal was 1.08 - 1.21 μm

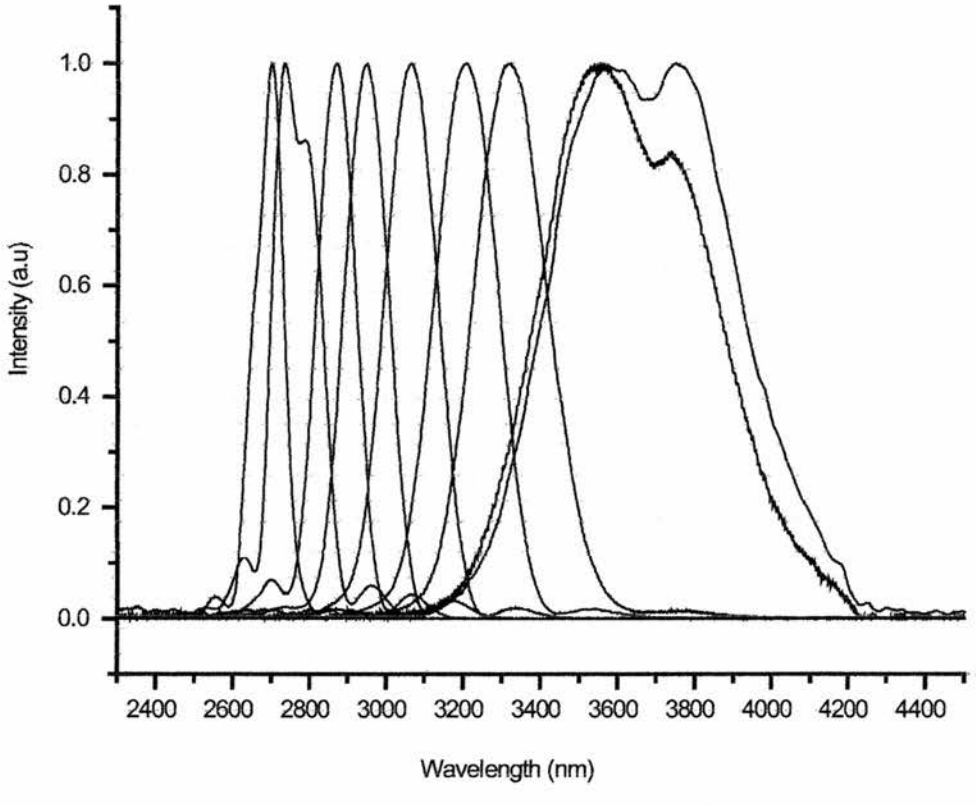

Figure 5-12 Sample of idler spectra across the tuning range of the dispersion-compensated PPRTA cavity. The complete wavelength range of the idler was 2.70 – 3.67 μm

It is clear from Figure 5-11 that the dispersion compensation has essentially eliminated the SPM in the signal pulses resulting in clean bell-shaped spectra. The signal autocorrelator measured pulse durations of 220 fs at the 1.21 μm end of the tuning range, which decreased continuously to 96 fs at the 1.08 μm end. An example spectrum and interferometric autocorrelation of the shortest signal pulses are shown in Figure 5-13.

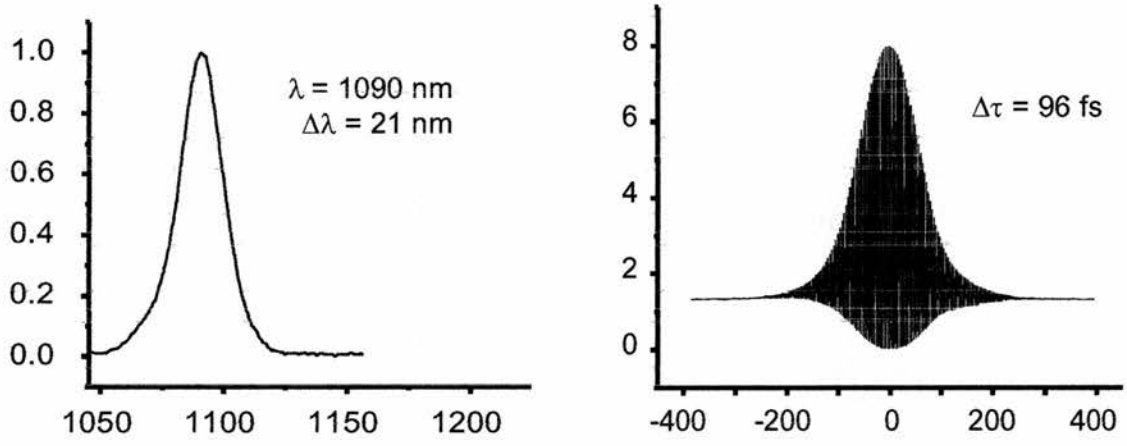

Figure 5-13 Wavelength spectra and interferometric autocorrelation of the shortest signal pulses from the dispersion compensated PPRTA OPO cavity.

The signal stability brought by the intra-cavity prism pair created a more stable idler output of similar output power, which was easier to autocorrelate than the previous configuration. However, the biggest change in the idler output was the very broad bandwidths created beyond 3.5 μm. A wavelength spectrum and autocorrelation of these broad bandwidth pulses can be seen in Figure 5-14.

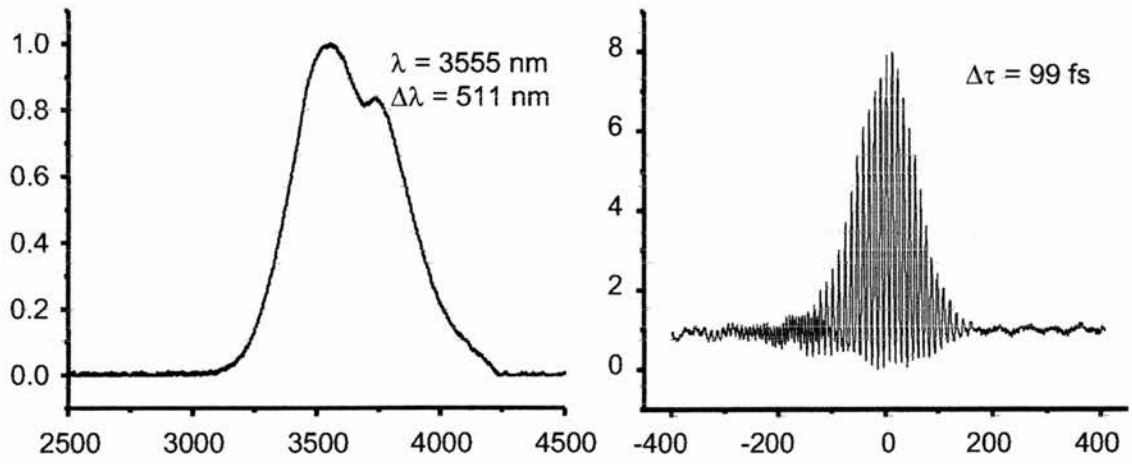

Figure 5-14 Wavelength spectra and interferometric autocorrelation of the broadest bandwidth pulses obtained from the dispersion compensated PPRTA OPO.

The FWHM bandwidth of these pulses was over 500 nm and the wavelength span of the pulse over 1000nm! Such a bandwidth would be sufficient to support pulses containing as few as three optical cycles (36 fs in duration). However, it is obvious from Figure 5-14 that the pulses were not transform limited (the transform limit is 1.2, far greater than the 0.44 ideal for Gaussian pulses) and also the results show the presence of multiple modes, characterised by the notch in the wavelength spectrum and the double fringing on the left side of the autocorrelation. This multi-mode idler output is present in the longest spectrum included in Figure 5-12 where two peaks are present. Unfortunately, the power of these longest pulses was too low to make a reasonable autocorrelation measurement as it dropped below 0.5 mW and was at the upper limit of response for the InGaAs photodiode detector.

5.3 Conclusion

For the work described in this chapter, a linear Ti:sapphire laser was used as the pump source for a periodically poled RTA based optical parametric oscillator. This laser produced transform limited pulses of 25 fs at 830 nm with an average power of 1.1 W. The pulse durations of ~ 25 fs from this laser were around twice that of pulses from the ring cavity design described in Chapter 4, but the greatly improved stability of the linear cavity proved to be more important than minimising pulse duration.

A PPRTA-based OPO was demonstrated as an alternative to the PPLN OPO as described in Chapter 4. Idler pulse durations of around 100 fs at 3.1 μm were obtained, although the time-bandwidth product of these pulses suggested the presence of frequency chirp. When the signal wave of the OPO was dispersion compensated, very broadband idler pulses were generated around 3.6 μm. These pulses had a FWHM bandwidth up to 550 nm and a base bandwidth of over a micron. However, the spectra and autocorrelation results showed signs of multiple modes or double pulsing within the idler wave and subtle changes in the cavity configuration were ineffective in removing this effect.

The results of the experiments so far have shown the generation of very broad bandwidth mid-infrared pulses which are in theory capable of supporting as few as three optical cycle pulses if correctly dispersion compensated. Idler dispersion compensation has, so far been unavailable, but in the next chapter the generation of even broader bandwidth pulses will be demonstrated along with an implementation to provide dispersion compensation.

5.4 References

1 P. E. Powers, C. L. Tang, and L. K. Cheng, "*High-Repetition-Rate Femtosecond Optical Parametric Oscillator Based on Rbtioaso4*", Optics Letters **19,** 1439-1441 (1994).

2 D. T. Reid, M. Ebrahimzadeh, and W. Sibbett, "*Noncritically Phase-Matched Ti-Sapphire-Pumped Femtosecond Optical Parametric Oscillator Based On Rbtioaso4*", Optics Letters **20,** 55-57 (1995).

3 D. T. Reid, Z. Penman, M. Ebrahimzadeh, W. Sibbett *et al.*, "*Broadly tunable infrared femtosecond optical parametric oscillator based on periodically poled RbTiOAsO4*", Optics Letters **22,** 1397-1399 (1997).

4 D. T. Reid, C. McGowan, M. Ebrahimzadeh, and W. Sibbett, "*Characterization and modeling of a noncollinearly phase-matched femtosecond optical parametric oscillator based on KTA and operating to beyond 4 mu m*", IEEE Journal of Quantum Electronics **33,** 1-9 (1997).

5 J. D. Bierlein and H. Vanherzeele, "*Potassium titanyl phosphate - properties and new applications*", Journal of the Optical Society of America B **6,** 622-633 (1989).

6 Z. W. Hu, P. A. Thomas, J. Webjorn, and G. M. Loiacono, "*Domain inversion in RbTiOAsO4 using electric field poling*", Journal of Physics D-Applied Physics **29,** 1681-1684 (1996).

7 D. L. Fenimore, K. L. Schepler, D. Zelmon, S. Kuck *et al.*, "*Rubidium titanyl arsenate difference-frequency generation and validation of new Sellmeier coefficients*", Journal of the Optical Society of America B-Optical Physics **13,** 1935-1940 (1996).

8 H. Karlsson, M. Olson, G. Arvidsson, F. Laurell *et al.*, "*Nanosecond optical parametric oscillator based on large- aperture periodically poled RbTiOAsO4*", Optics Letters **24,** 330-332 (1999).

9 H. Karlsson, *Institute of Optical Research, Royal Institute of Technology* (Lindstedtsgen 24, 100 44 Stockholm, Sweden).

10 Rees Instruments Ltd, (Thornbrook, Weyside Park, Cattleshall Lane, Godalming, Surrey, GU7 1XE).

11 M. M.-i. O. S. Analyser, *Macam Photometrics Ltd. , 10 Kelvin Square, Livingston, EH45 5PF.*

Chapter 6

Aperiodically Poled Lithium Niobate Femtosecond OPO

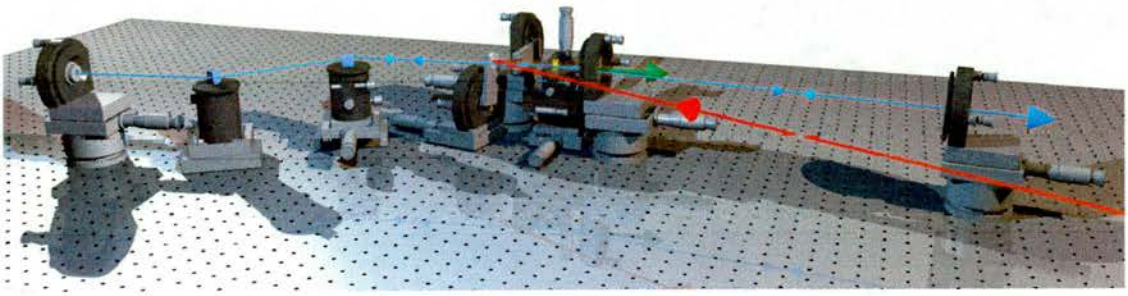

Artistic visualisation of the APPLN-OPO

In recent years there have been numerous advances in the generation of few optical cycle pulses. Careful control of 2nd and 3rd order dispersion using intracavity pairs of fused-silica prisms allowed the generation of visible pulses as short as 4 optical cycles within the intensity full width half maximum (FWHM) from a laser oscillator [1,2]. Dispersion engineered mirrors now allow laser cavities to be built with exactly the required phase characteristics [3], and have produced pulses containing 2.5 optical cycles [4]. Pulse compression techniques exploiting the spectral broadening due to self-phase modulation of a short pulse in a suitable nonlinear medium, such as a single-mode optical fibre, have generated pulses containing as few as 1.8 cycles [5]. Recently optical parametric amplifiers (OPA's) have generated sub-3 cycle pulses in the visible [6] and near infrared [7].

This chapter describes a new approach to the generation of few optical cycle mid-infrared pulses using an optical parametric oscillator (OPO) based on a chirped grating PPLN crystal. The results this produced show great potential for chirped grating OPOs for few cycle pulse generation in the mid-infrared.

6 Aperiodically poled crystals

The application of nonlinear crystals with novel phase matching characteristics based on quasi-phase matching (QPM) has enabled the parametric generation of a wide range of infrared wavelengths from ~1 to 7 μm at high conversion efficiencies within the femtosecond regime [8,9]. Femtosecond QPM OPO's that use crystals with a uniform grating are subject to bandwidth limiting effects such

as temporal walk-away, restricted acceptance bandwidth and back conversion, which become increasingly more significant for shorter pump pulses. These effects can be avoided by using a suitably designed crystal with a linearly-chirped grating period.

The use of quasi-phasematched crystals with a linearly varying grating period was first discussed for second harmonic generation (SHG) and compression [10]. When a dispersion-broadened chirped pulse of known frequency chirp is incident on such a crystal, the variation of the grating period with crystal length can be arranged so that all the frequency doubled components leave the crystal simultaneously, effectively resulting in pulse compression at the SHG wavelength. Second harmonic generation using aperiodically poled lithium niobate (APPLN) was first demonstrated to recompress artificially stretched picosecond pulses from an erbium-doped fibre laser [11], and a theoretical model of the compression process for quadratic phase chirped pulses has been proposed [10].

This technique can be implemented for optical parametric generation with simultaneous idler pulse compression. Figure 6-1 illustrates the idler pulse compression process in APPLN. The longer wavelength component of the chirped pump, λ_r, enters first and travels almost entirely through the crystal before being converted to signal and idler components by the longer grating periods, (A). The shorter wavelength component, λ_b, enters later but is converted nearer the front of the crystal, (B). The faster group velocity of the shorter wavelength idler wave allows it to catch up with the longer wavelength component that has spent more time travelling at the slower pump group velocity.

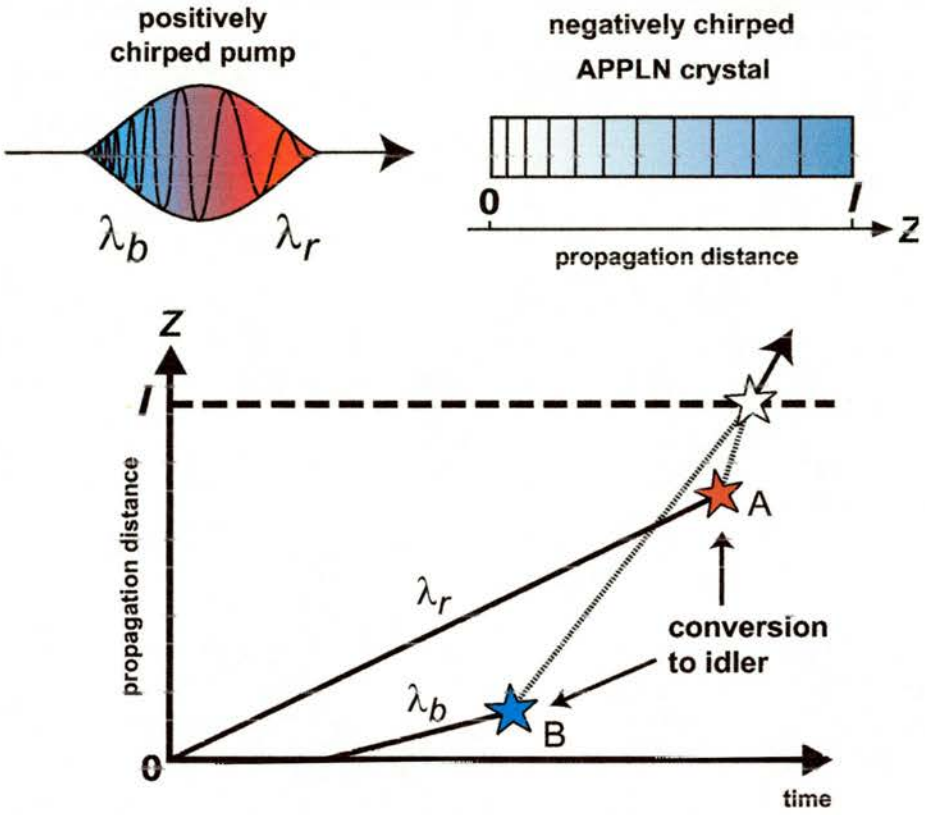

Figure 6-1 Schematic representation of optical parametric generation with idler pulse compression in APPLN

The grating period required for optical parametric generation, Λ, is a function of the pump and signal wavelength and is defined as

$$\Lambda = \left[\frac{n_p - n_i}{\lambda_p} + \frac{n_i - n_s}{\lambda_s} \right]^{-1} \tag{6.1}$$

where $n_{p,s,i}$ are the pump, signal and idler refractive indices and $\lambda_{p,s}$ the pump and signal wavelengths. The point at which the pump and signal are phasematched within the crystal is defined as

$$z = \frac{l(\Lambda - \Lambda_i)}{\Lambda_f - \Lambda_i} \tag{6.2}$$

where Λ_i, is the initial (or input) period and, Λ_f, the final (or output) period of the grating and l is the crystal length. The exit time for any one idler wavelength component is:

$$t_i = t(\lambda_p) + \frac{z}{v_g(\lambda_p)} + \frac{(l-z)}{v_g(\lambda_i)} \tag{6.3}$$

where $v_g(\lambda_{p,i})$ is the group velocity of the corresponding pump and idler wavelengths, z is the pump propagation distance through the crystal before conversion and $t(\lambda_p)$ is the launch time of the pump wavelength component λ_p, which depends on the pump chirp. If the signal wave is assumed narrowband, with respect to the pump pulse, then an appropriately chirped pump pulse can be arranged to combine with the resonant signal wave at differing positions throughout the crystal such that all idler components will leave simultaneously as a transform limited pulse. In this model we also assume that the durations of the pump and signal pulses are such that they overlap temporally throughout the crystal.

The APPLN crystal, manufactured by Deltronic [12], was 1 mm long with eight different linearly chirped gratings distributed equally across a 10 mm aperture, Figure 6-2. In each chirped grating Λ_i and Λ_f were different while the average grating period, $\Lambda_{av} = (\Lambda_i + \Lambda_f)/2$, was within ~0.1 μm of 22.86 μm. The most chirped grating had periods ranging from 21.89 μm to 23.55 μm while the least chirped had a uniform period of 22.96 μm. The crystal was AR coated at 1.115 μm and held at 150 °C to prevent photo-refractive damage.

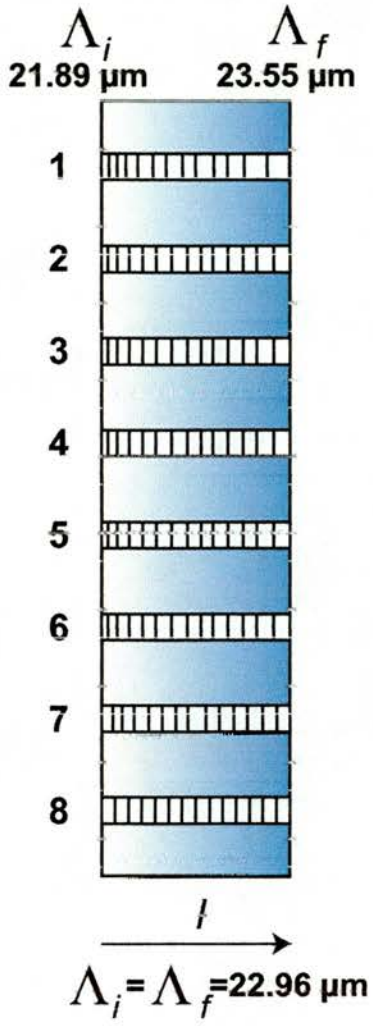

Figure 6-2 Illustration of the APPLN crystal gratings. Grating 1 has the greatest aperiodicity while subsequent gratings have decreasing aperiodicity to grating 8, which is uniform.

6.1 Pump characterisation

The pump laser used for these experiments was the same as that described in Chapter 5. However, this time the pump pulses were chirped before entering the OPO to match the grating chirp on the PPLN crystal grating. Interferometric autocorrelation doesn't give any quantitive information about the chirp of a pulse so a FROG measurement technique was used.

The FROG system, as described in Chapter 3, used a KDP crystal as the nonlinear component. The phasematching angle of the crystal was calculated as $\theta = 66.9^{\circ}$ for type II SHG at 840 nm. The optimum thickness of the crystal to maximise phasematching over the broad 40+ nm FWHM bandwidth of the pump pulse was determined from the term:

$$X(\lambda) = \left[\frac{\sin\left(\frac{\Delta k l}{2}\right)}{\frac{\Delta k l}{2}} \right]^2 \tag{6.4}$$

which comes from Equation 2.21 for parametric gain. Figure 6-3 shows the phasematching percentage over the pump laser bandwidth for a KDP crystal thickness of l = 50 μm. This very thin crystal was mounted on a 4 x 5 x 0.5 mm fused silica substrate which was manufactured by Ingcrys Laser Systems [13].

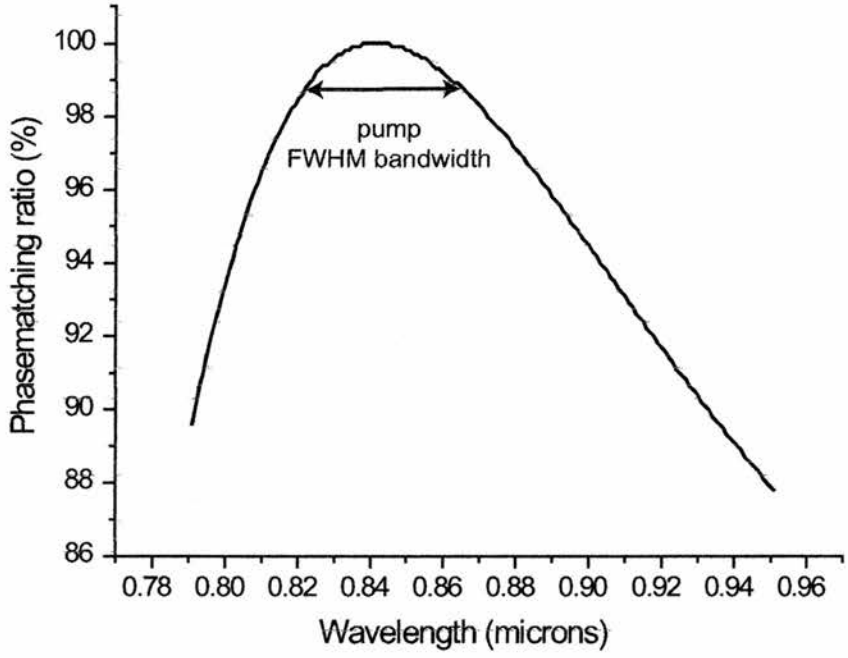

Figure 6-3 With a 50 μm thick KDP crystal the minimum phasematching percentage is ~99 % across the pump pulse FWHM bandwidth.
This would drop to 90 % if a 100 μm crystal were used.

The experimental setup of the FROG system is shown in Figure 6-4. The design was optimised for femtosecond pulse measurement with a two part 0.5 mm thick beam splitter (so that each beam experiences the same losses) and a parabolic mirror to focus the beams into the crystal. Since the KDP crystal required type II phasematching the two pump beam components had to have orthogonal polarisations. This was achieved with by a half wave plate in each arm of the interferometer to rotate the two beams +45° and -45° to the horizontal. The KDP crystal was also rotated at an angle of 45° to the horizontal.

The moving corner cube was mounted on a piezo translation stage. This had a maximum movement range of 400 μm in 150 steps. The piezo stage was controlled by a counter box, which in turn was synchronised to the control box of the diode array. The detector array (Hamamatsu C4350, Si scanning CCD) had 512 pixel elements and was placed at the output of the monochromator.

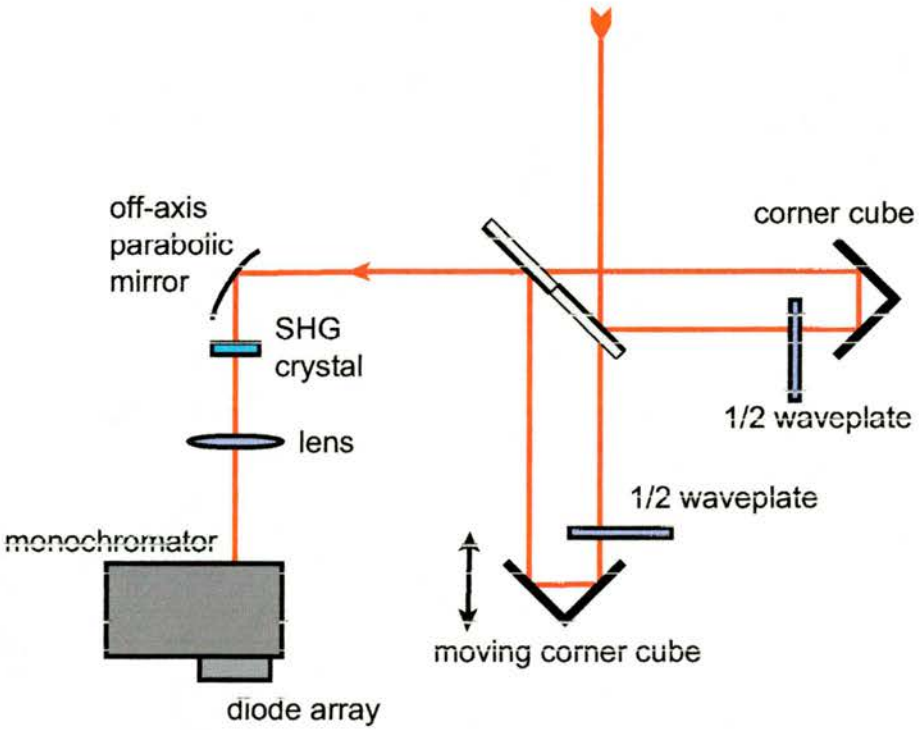

Figure 6-4 Experimental FROG setup.

The diode array control box and piezo-stage driver, were linked to a computer which recorded each acquisition of the array and synchronised the whole instrument. Before any measurements could be made the delay line was calibrated in time and the diode array in wavelength.

The maximum delay was determined from the product of the maximum piezo translation (400 μm) with the percentage of the piezo stage translation required to scan across the pulse. This is doubled as it is a round trip and resulted in a maximum delay of 1.33 ps.

With the piezo stage stationary and set at an equal length to the other arm in the interferometer, a maximum SHG signal is generated. The peak of the trace recorded by the diode array from the maximum SHG signal corresponds to the centre wavelength of the laser pulse which was measured with a Rees E200 Series laser spectrum analyser [14]. This determined the centre wavelength pixel on the array. The monochromator was then tuned by 10 nm either side of the centre wavelength and the pixel position of the peak of the resulting trace was recorded. From this, the wavelength span of one pixel was calculated, and so the wavelength range of the array was found.

Due to inadequacies in the drivers used to interface the computer with the diode array control box, a maximum acquisition rate of only 2.7 Hz was achieved, such that a typical measurement involving 128 samples required ~48 seconds.

As briefly mentioned in Chapter 5, the Ti:sapphire pump laser required an extra-cavity four-prism sequence to dispersion compensate the laser output, Figure 6-7. Fine control of the pulse chirp was possible by translating the middle two prisms in or out of the beam path to change the optical path length through the

fused silica material. This mechanism provided a way of chirping the pump pulse before it entered the chirped-PPLN OPO.

In order to find the best match of pump chirp to crystal grating chirp, eight different prism insertions were used with a path length through each of the middle two prisms ranging 1.4 mm to 16.5 mm per prism. FROG measurements of the pump laser were then acquired for each of the eight prism insertions. A typical output from the FROG is shown in Figure 6-5. The rms error for this measurement was small at 0.0044, and retrieval was implemented by the use of a 128 x 128 array. It was found that 30 iterations of the FROG retrieval algorithm (as described in Chapter 3) were sufficient to obtain convergence. The results are of pulses that have passed through a total of 16 mm of prism glass which was the fourth position for chirping the pump pulses. As we will see later, pump pulses of this particular chirp produced the shortest duration mid-infrared idler pulses.

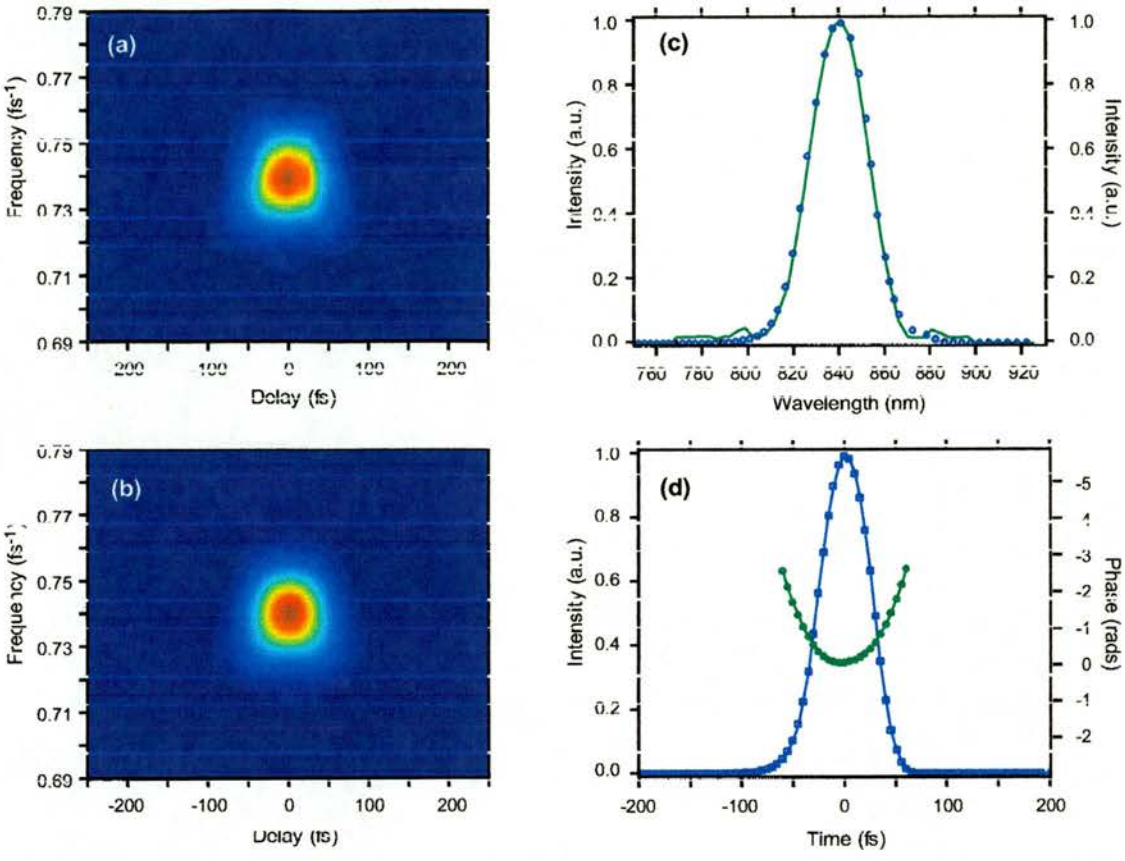

Figure 6-5 (a) Measured and (b) retrieved FROG traces for the pump pulses at 840 nm. The measured spectrum is shown in (c) with the retrieved spectral data overlaid (circles). Retrieved temporal intensity with phase is shown in (d). This pump pulse had a relative second-order dispersion of 140 fs^2 and produced the shortest idler pulses.

FROG measurements for all eight pump chirps were acquired and a plot of pulse duration verses relative second-order dispersion was obtained, see Figure 6-6.

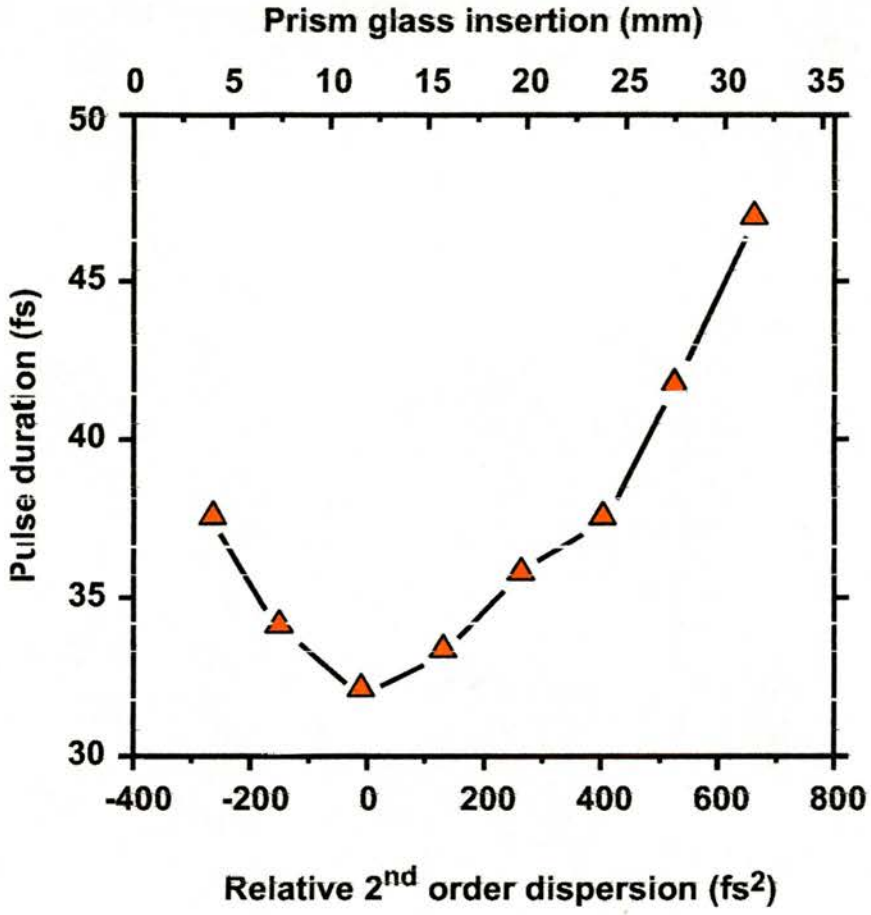

Figure 6-6 Pump pulse duration versus relative second-order dispersion.

Figure 6-6 shows optimum dispersion compensation for ~14 mm of prism glass insertion. As expected the pump pulse becomes more chirped and the duration increases as more prism glass is included.

6.2 APPLN OPO

The OPO was configured as a symmetric four mirror X-cavity, Figure 6-7, with mirrors comprising a CaF2 substrate of 0.5 mm thickness with a high reflectivity (R > 99.8%) coating at the signal wavelength of 1.115 μm. The cavity head mirrors had a radius of curvature of 100 mm and were placed 50 mm either side of the crystal. The signal wave was output-coupled through a plane cavity end

mirror with 0.8% transmittance. The introduction of unwanted dispersion to the incident pump and generated idler pulses was minimised by using these thin mirrors, allowing the pump pulse duration to be maintained while down-converting to idler wavelengths. A curved dielectric mirror with radius of curvature 150 mm was used to focus the pump light into the crystal through one of the curved cavity mirrors and the generated idler beam transmitted through the opposite curved cavity mirror was collected and collimated using a gold mirror with radius of curvature of 200 mm.

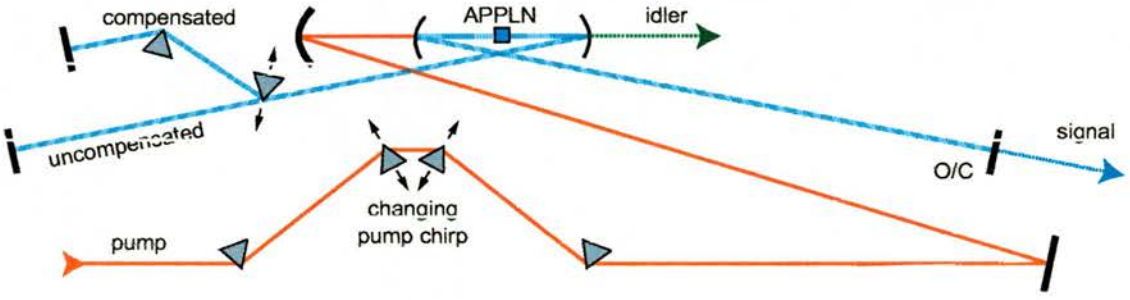

Figure 6-7 Cavity design of the APPLN OPO

The OPO was pumped collinearly by a Ti:sapphire laser which produced pulses of around 45 fs in duration centred at 840 nm with 1 W average power and a repetition rate of 84.5 MHz. Extracavity dispersion compensation was included in the form of two pairs of fused silica prisms (apex separation 640 mm) which were necessary to remove chirp acquired by the pump pulse after passing through the 7 mm thick BK7 output coupler. Variation of the prism insertions was used as a means of pre-chirping the pump pulses before entering the OPO. A pair of F2 prisms were used for intracavity dispersion compensation of the signal pulses and provided additional control over the signal wavelength. The dispersion was adjusted so that the signal was chirp free and of duration comparable to the temporal walk-away between the pump and signal pulses.

These conditions were necessary for the signal to be relatively monochromatic and available for interaction with the pump at all positions in the crystal. Without intra-cavity dispersion compensation the idler centre wavelength would fluctuate by up to ± 50nm. Even with prisms inserted, air currents in the lab limited the stability by causing slight changes in the air density thus changing the optical path length. The only way to minimise this effect would be to encase the OPO within a box. Unfortunately, the layout of the OPO on the optical bench made this impractical.

6.3 Results

Initially to obtain maximum parametric generation the crystal was oriented for negative crystal chirp defined as $\Lambda_i < \Lambda_f$. A low dispersion two-photon autocorrelator based on an InGaAs photodiode was used to measure the idler pulse durations and a Macam scanning optical spectrum analyser [15] was used to measure the idler spectrum. Changing the cavity length by 25 μm resulted in an idler tuning range of 2.7 – 3.7 μm. Although the bandwidth of the pulses at 3.7 μm was in excess of 500 nm the power was relatively low (few-mW). The low idler power was most likely due to the fact the APPLN has lower gain compared to its PPLN counterpart. A set of measurements were taken with the OPO wavelength tuned to 3 μm where a maximum idler power of approximately 5-10 mW was measured. The pump threshold of the OPO was measured as approximately 450 mW.

For each of the eight gratings the pump was pre-chirped by eight varying amounts and the idler spectrum and autocorrelation at 3 μm were measured.

Figure 6-8 shows the pulse durations for all grating and pump chirp combinations. The plot has been illustrated with discreet cells as the grating chirp is non-continuous.

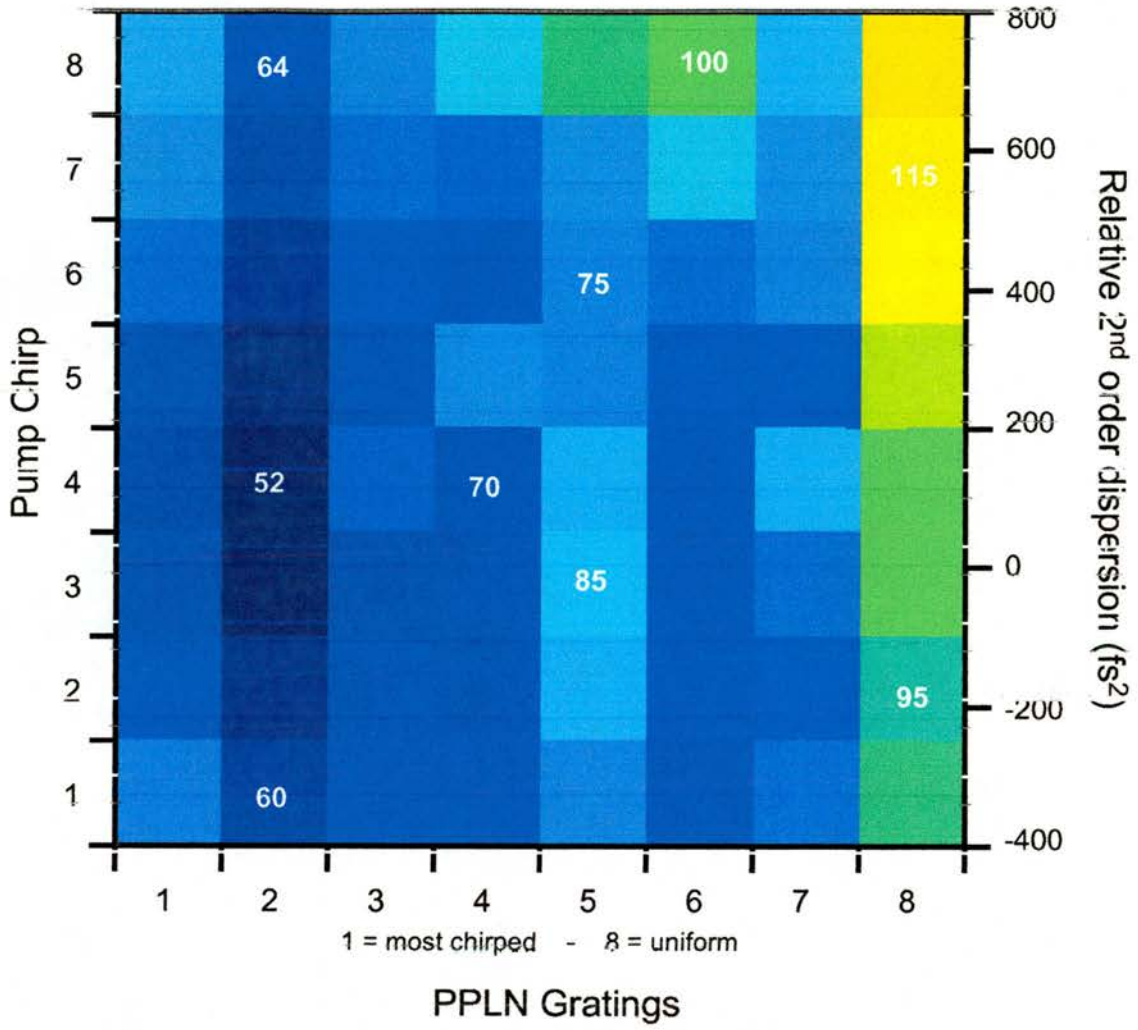

Figure 6-8 Idler pulse durations at 3 μm for eight different gratings and pump chirps for a negatively chirped crystal orientation. Idler pulse durations in fs are overlaid for selected cells.

The crystal was then reversed for positive chirp, $\Lambda_i > \Lambda_f$, and the idler pulse measurements repeated. Figure 6-9 shows the idler pulse durations for a positively chirped grating orientation. As expected, grating 8 (uniform grating period) shows the same range of pulse durations for each crystal orientation.

Grating 2 produced the shortest pulses with the crystal orientated for negative grating chirp, while grating 1 (the most chirped) produced the longest pulses when the crystal was orientated for positive grating chirp.

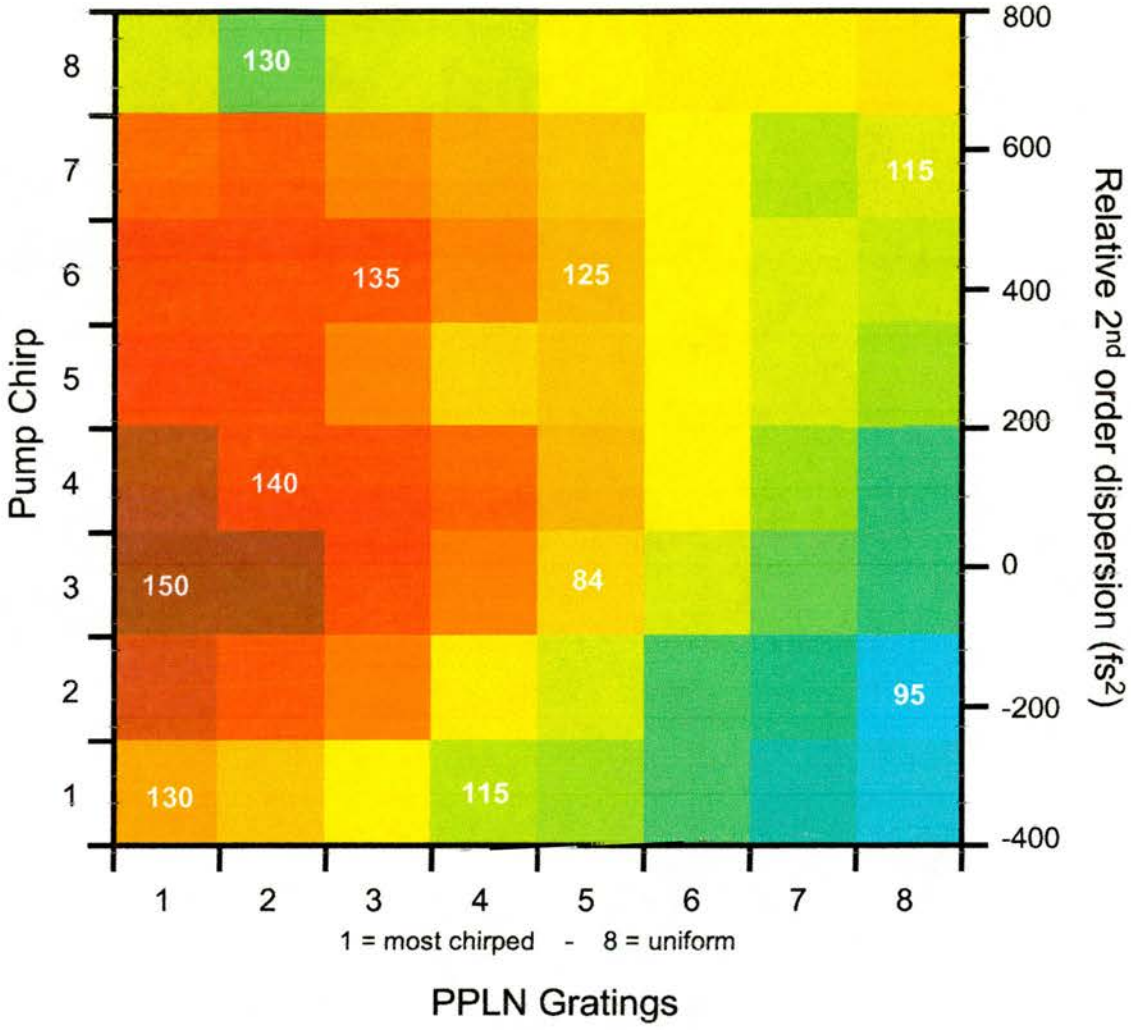

Figure 6-9 Idler pulse durations at 3 μm for eight different gratings and pump chirps for a positively chirped crystal orientation. Idler pulse durations in fs are overlaid for selected cells.

Figure 6-10 shows the variation of idler pulse duration with pump chirp for a negatively chirped grating, the unchirped grating and a positively chirped grating.

The shortest idler pulses were recorded using a negatively chirped grating with periods from 22.00 - 23.54 μm (7% chirp) and a positively chirped pump. With 140 fs^2 of positive 2nd order dispersion added to the pump pulse, optimum

conversion occurred generating idler pulses as short as 53 fs. These pulses had a time-bandwidth product of 0.48, which is within 10% of the time-bandwidth product calculated from the experimental spectrum assuming constant spectral phase. This result implies that the idler pulses will contain around five optical cycles within the intensity FWHM.

It can be seen from Figure 6-10 that the negatively chirped grating offers a significant advantage over a conventional uniform grating for generating ultrashort idler pulses. With the crystal in a positively chirped orientation, the pulses are much broader because the idler components generated from different parts of the chirped pump pulse leave the crystal at different times.

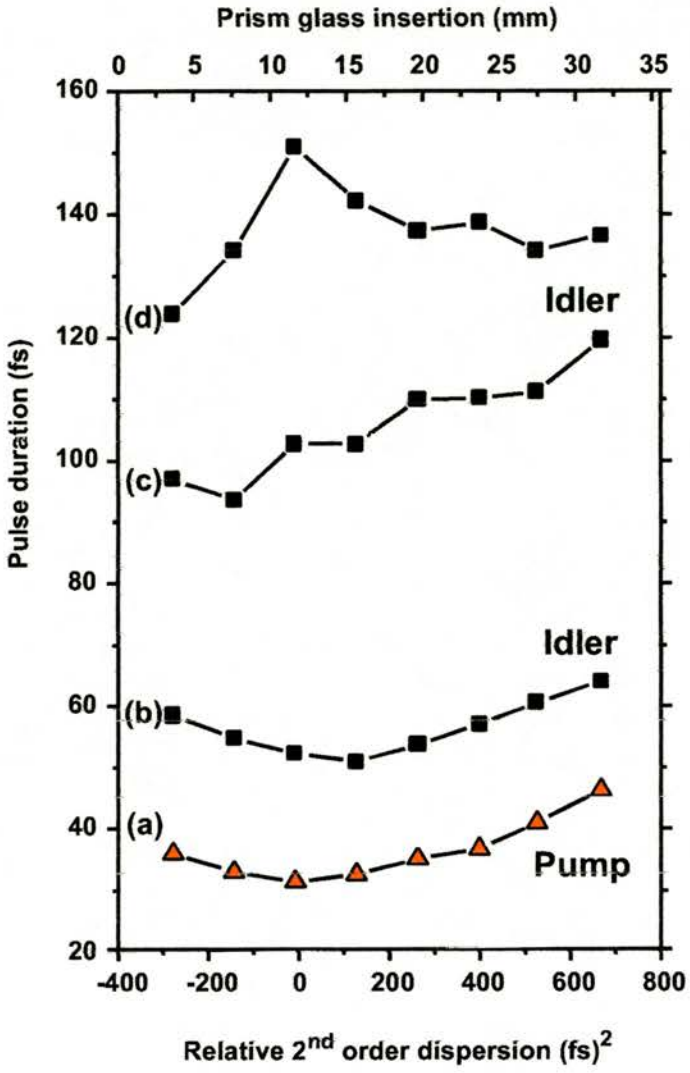

Figure 6-10 Measured idler pulse duration at 3 μm as the 2nd order dispersion of the pump is increased. (a) Pump duration variation as the pulse is chirped. (b) Idler pulse duration with varying pump chirp for the negatively chirped 22.00 - 23.54 μm grating. (c) Idler pulse duration with the uniform grating of 22.96 μm. (d) Idler pulse duration for the positively chirped grating, 23.54 – 22.00 μm

Figure 6-11 shows the spectrum and interferometric autocorrelation of the shortest idler pulses with a best-fit autocorrelation profile.

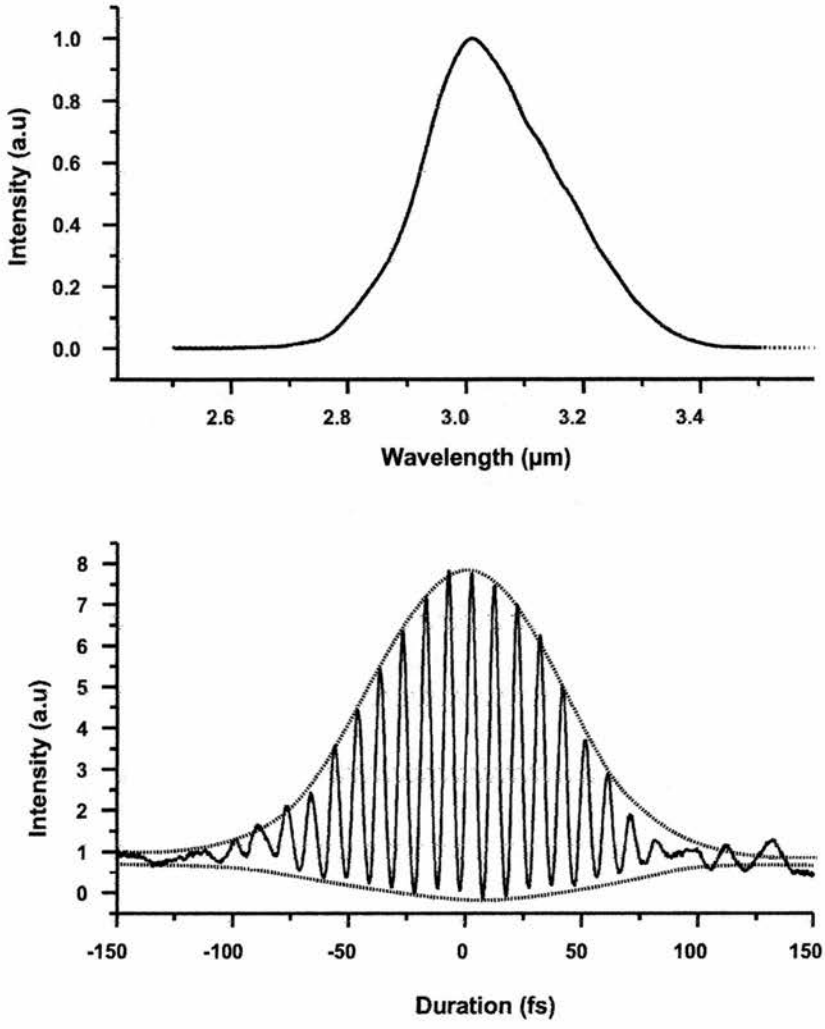

Figure 6-11 Idler spectrum and interferometric autocorrelation. The spectral bandwidth is 270 nm centred at 3.02 μm and the duration inferred from the best-fit autocorrelation profile is 53 fs. The duration bandwidth product is 0.48

The best-fit envelope of the interferometric autocorrelation was obtained from the Fourier transform of the frequency spectrum with 510 fs^2 of spectral quadratic phase. The spectrum is centred at 3.02 μm with a bandwidth of 270 nm. The inferred duration is 53 fs with a duration bandwidth product of 0.48. Such pulses contained 5 optical cycles and at the time were the first to be generated using an OPO based on an APPLN crystal.

6.4 Broad bandwidth mid-infrared pulse generation

Dispersion compensation of the OPO greatly improved the oscillator stability and allowed continuous tuning of the idler spectra. However, in an uncompensated configuration with the crystal in a positively chirped orientation it was possible to produce very broad bandwidth pulses centred around 3.5 - 3.7 μm. These broad bandwidth pulses were created with gratings 2, 3 & 4 while the other gratings, up to grating 8 (unchirped), produced pulses too unstable to adequately measure. One of the broadest bandwidth spectra was obtained from the 3rd grating (23.52 - 22.12 μm) and is shown in Figure 6-12 with its interferometric autocorrelation. Centred at 3.7 μm with a bandwidth of 720 nm, the typical output power of these pulses was around 1.5 mW. The autocorrelation shown was one of the best acquired, but even then was only just resolved above the background noise. It is slightly asymmetric and noisy, so the pulse duration could not be determined from a best-fit autocorrelation profile. However, the results do tell us that the idler pulses were highly chirped as the bandwidth is broad enough to support ~20 fs pulses which would correspond to less than 2 optical cycles centred at 3.7 μm, but the autocorrelation suggest actual pulse durations of at least 3.5 times this.

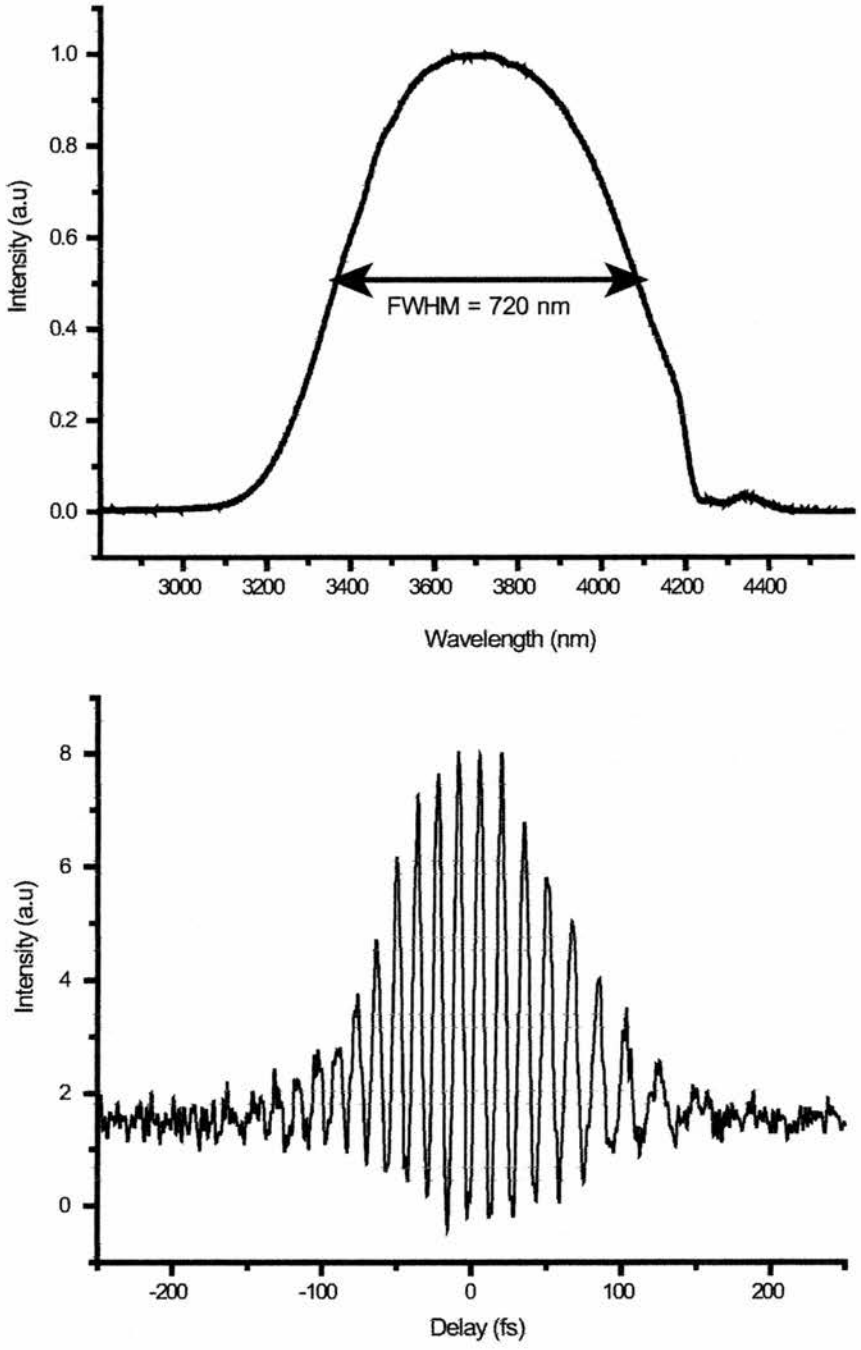

Figure 6-12 Broad bandwidth idler pulse spectra and interferometric autocorrelation. The autocorrelation shown was only just resolved above the background noise and is slightly asymmetric so the pulse duration could not be determined using a best-fit autocorrelation profile.

Since the idler pulses were shown to be highly chirped, a method of mid-infrared dispersion compensation was created. A system in which a double pass through a germanium prism was built [16] in an attempt to control the idler dispersion, Figure 6-13.

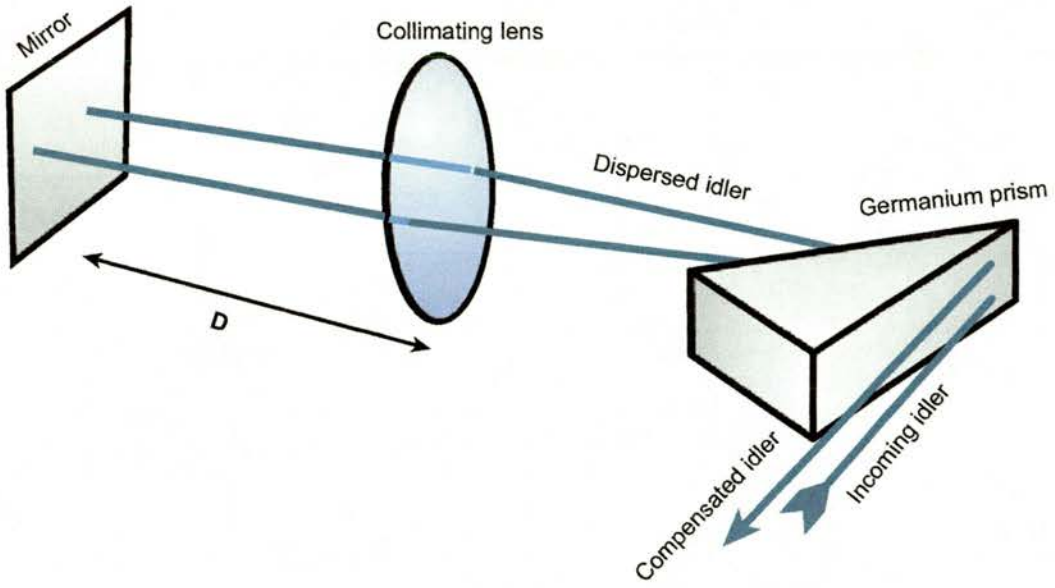

Figure 6-13 Dispersion compensation system for mid-infrared pulses.

The incoming idler beam passes through the bottom half of the germanium prism. The dispersed beam is then collimated by a CaF_2 lens and retro-reflected back slightly higher through the prism. The compensated return beam leaves the prism for the second time slightly higher so that it could be picked off by another mirror and sent to the autocorrelator. Small changes in the distance D provides a way of finely controlling the dispersion compensation. The mirror-prism separation was set at 40 cm. The lens will introduce pulse broadening dispersion so would ideally be replaced with a curved mirror.

Unfortunately, the double pass through the CaF2 lens and germanium prism proved too great a loss to the idler beam and there was too little power to autocorrelate the resulting pulses. A considerable amount of time (almost four months) was spent trying to measure these pulses using a variety of InGaAs and InGaSbAs photodiodes, but without success. Although spectra could be recorded and the beam could be traced through the autocorrelator and aligned

accurately onto the photodiode with a lead selenide detector, there was never enough signal to get a two photon response.

Even if autocorrelation measurements were obtained, it would be unlikely that the result would be representive of the complete pulse bandwidth as such bandwidths are greater than the two-photon response of the photodiode. Without temporal measurements we were unable to determine whether the germanium-based dispersion compensation achieved its objective. Given more time, the next direction would be to construct a complete cover for the beam paths of the OPO to minimise disturbances from air currents and maximise the output stability. By minimising the intensity fluctuations in idler output it may have been possible to resolve an autocorrelation signal over a larger time average.

With the OPO in an uncompensated configuration and with the crystal in a positively chirped orientation (23.43 – 22.0 μm) the signal was highly chirped so the simple model outlined earlier for pulse compression was no longer valid. The very broad-bandwidth pulses this configuration created is counter intuitive, as a chirp free signal combined with a positively chirped grating produced narrow bandwidth pulses. The uncompensated signal pulse is obviously the key factor for broad-bandwidth idler generation, but without sufficient temporal data we have been unable to determine the exact processes involved. Unfortunately, further investigation was beyond the timescale of this project. However, avenues in which this work could proceed would be to firstly increase the idler output power. Near the end of the project the aging Millennia X Ti:sapphire pump laser started to fail and its output power dropped by almost 2 watts. This decreased the Ti:sapphire output power from 1.1 W to ~800 mW which could

have pushed the maximum idler output power below a measurable threshold. Once an idler output power of more than a few milliwatts is obtained autocorrelation should be possible. Further possibilities would be a FROG measurement of the idler pulses. Comparing FROG traces of the pump and idler pulses would give a greater insight into the processes involved in generating these broad bandwidth pulses.

Finally variations on the configuration of the chirped crystal grating could open up a new area of OPO based research. For instance, the grating periods of the crystal could be designed to match the quadratic chirp of a pump pulse instead of assuming a linear chirp, as used in this work.

6.5 Conclusion

The results described in this chapter have demonstrated an OPO system based on aperiodically poled lithium niobate, which was the first of its kind. It was shown that a negatively chirped grating coupled with a positively chirped pump pulse generated significantly shorter mid-infrared pulses compared to a conventional uniform grating PPLN based OPO. The shortest pulses produced were 53 fs in duration which corresponds to 5 optical cycle pulses at 3 μm.

With the help of an SHG FROG system based on a KDP crystal and a diode array, a more complete characterisation of the pump pulses was obtained.

The surprise result was the generation of extremely broad bandwidth pulses obtained when the OPO cavity was uncompensated (so had a highly chirped signal) and the crystal was orientated for positive grating chirp. Pulse bandwidths of up to 720 nm were recorded along with a few autocorrelations, which suggested highly chirped pulses. An attempt to dispersion compensate these idler pulses was made, but the germanium prism system proved too lossy. Unfortunately, without adequate temporal measurements we have been unable to determine the exact processes making these very broad bandwidth pulses. If suitably dispersion compensated, these measurements imply adequate bandwidth to support pulses containing as few as two optical cycles, a significant step towards the elusive single cycle mid-infrared pulse.

6.6 References

1 P. F. Curley, C. Spielmann, T. Brabec, F. Krausz *et al.*, "*Operation of a Femtosecond Ti-Sapphire Solitary Laser in the Vicinity of Zero Group-Delay Dispersion*", Optics Letters **18,** 54-56 (1993).

2 I. P. Christov, M. M. Murnane, H. C. Kapteyn, J. P. Zhou *et al.*, "*4th-Order Dispersion-Limited Solitary Pulses*", Optics Letters **19,** 1465-1467 (1994).

3 L. Xu, C. Spielmann, F. Krausz, and R. Szipocs, "*Ultrabroadband ring oscillator for sub-10-fs pulse generation*", Optics Letters **21,** 1259-1261 (1996).

4 I. D. Jung, F. X. Kartner, N. Matuschek, D. H. Sutter *et al.*, "*Self-starting 6.5-fs pulses from a Ti:Sapphire laser*", Optics Letters **22,** 1009-1011 (1997).

5 A. Baltuska, Z. Y. Wei, M. S. Pshenichnikov, and D. A. Wiersma, "*Optical pulse compression to 5 fs at a 1-MHz repetition rate*", Optics Letters **22,** 102-104 (1997).

6 G. Cerullo, M. Nisoli, S. Stagira, and S. De Silvestri, "*Sub-8-fs pulses from an ultrabroadband optical parametric amplifier in the visible*", Optics Letters **23,** 1283-1285 (1998).

7 M. Nisoli, S. Stagira, S. De Silvestri, O. Svelto *et al.*, "*Parametric generation of high-energy 14.5-fs light pulses at 1.5 mu m*", Optics Letters **23,** 630-632 (1998).

8 P. Loza-Alvarez, C. T. A. Brown, D. T. Reid, W. Sibbett *et al.*, "*High-repetition-rate ultrashort-pulse optical parametric oscillator continuously tunable from 2.8 to 6.8 mu m*", Optics Letters **24,** 1523-1525 (1999).

9 K. C. Burr, C. L. Tang, M. A. Arbore, and M. M. Fejer, "*Broadly tunable mid-infrared femtosecond optical parametric oscillator using all-solid-state-pumped periodically poled lithium niobate*", Optics Letters **22,** 1458-1460 (1997).

10 M. A. Arbore, O. Marco, and M. M. Fejer, "*Pulse compression during second-harmonic generation in aperiodic quasi-phase-matching gratings*", Optics Letters **22,** 865-867 (1997).

11 M. A. Arbore, A. Galvanauskas, D. Harter, M. H. Chou *et al.*, "*Engineerable compression of ultrashort pulses by use of second- harmonic generation in chirped-period-poled lithium niobate*", Optics Letters **22,** 1341-1343 (1997).

12 Deltronic/Gemfire Crystal Industries, (2471 E Bayshore Road, Suite 600, Palo Alto, CA 94303).

13 Ingcrys Laser Systems Ltd, (14 Parrs Road, Stockenchurch, High Wycombe, Bucks. HP14 3QF).

14 Rees Instruments Ltd, (Thornbrook, Weyside Park, Cattleshall Lane, Godalming, Surrey, GU7 1XE).

15 Macam Photometrics Ltd, (10 Kelvin Square, Livingstonm, EH54 5PF).

16 M. Wurm, R. A. Kaindl, K. Reimann, and M. Woerner, "*Intense femtosecond mid-infrared pulses tunable between 3-20um*", CLEO 2000 Technical Digest, 441 (2000).

Chapter 7

General Conclusions

The work in this thesis has been concerned with the design, configuration and operation of femtosecond optical parametric oscillators based on periodically-poled lithium niobate (Chapters 5 & 6) and periodically-poled rubidium titanyl arsenate (Chapter 5) for the generation of few optical cycle pulses in the mid-infrared spectral region. It has also shown the development of a Ti:sapphire ring laser design capable of producing transform limited pulses of 13 fs duration with up to a megawatt peak power (Chapter 4) and covered a variety of pulse measurement techniques.

Chapter 1 traced the history of few-cycle optical pulse generation to the current limit of 1.8 cycles [1] from an amplified laser system. A selection of possible applications of few-cycle pulses were discussed, from broadband spectroscopy in the mid infrared to the coherent quantum control of molecules. Such applications provide the motivation for few optical-cycle pulse research.

The Ti:sapphire laser is one of the most important laser sources in ultrashort pulse research, and was the driving force behind the experiments described throughout this thesis. Thus, the physical properties of the Ti:sapphire gain medium along with the mechanisms involved to achieve Kerr lens modelocking were examined. The behaviour of the resulting ultrashort pulses when propagating through linear and nonlinear media was also described.

Chapter 2 discussed the basic concepts of nonlinear optics and provided the theory behind the experiments of the later chapters. Phasematching was described along with the birefringent and quasi-phasematching (QPM) techniques used to achieve this. The general theory of QPM was reviewed along with the implementation of QPM devices by the periodic-poling technique in ferroelectric materials. It was shown that periodically poling these materials enables access to the largest nonlinear coefficients, therefore allowing more efficient frequency conversion processes.

In Chapter 3, several techniques were discussed for the measurement of ultrashort pulses. The relevant concepts behind intensity and interferometric SHG autocorrelation were introduced along with their limitations for measuring femtosecond pulses. Autocorrelators utilising two-photon absorption were presented and their experimental simplicity and ability to measure femtosecond pulses highlighted.

The limitation of $\chi^{(2)}$-based autocorrelators to provide complete phase information about the femtosecond pulses has lead to alternate measurement techniques. The frequency resolved optical gating (FROG) and sonogram time-frequency domain techniques were introduced as powerful tools to supersede autocorrelators. The concepts of these techniques were presented as a background for the experimental work presented in subsequent chapters.

Chapter 4 detailed the first of the two Ti:sapphire lasers used throughout this work. Conventional measurements showed that the Ti:sapphire ring laser produced transform-limited 13-fs pulses with peak powers up to 1 MW. At the time this was the only Ti:sapphire based laser capable of reaching such peak

powers using only standard 'off-the-shelf' components. The laser system described would be suitable as a high-intensity pump source for nonlinear optics and for other applications in which an amplified or a cavity-dumped system were previously necessary.

The relatively new technique of measuring the pulse sonogram provided a simple method for carrying out a complete measurement of the amplitude and phase of any ultrashort pulse, and its suitability to measure broad-bandwidth sub-15-fs pulses was demonstrated. This technique has formed the basis for a subsequent PhD project aiming at the development of a 'femtosecond scope' [2].

Although the ring laser could produce excellent results this was at the expense of extensive re-optimisation, often on a daily basis. The very nature of the ring configuration meant that it was highly sensitive to misalignment compared to a typical linear cavity. Although the ring laser was very capable as a pump source and produced results that were interesting in their own right, it was decided that a pump source that produced more predictable and consistent results was necessary for future OPO experiments, so in Chapter 5 the ring laser was reconfigured to a linear cavity.

Later in Chapter 4, a PPLN-based OPO was discussed with modifications to the cavity elements to minimise pulse duration broadening of the pump pulses during their frequency down-conversion to idler pulses in the mid infrared. It was believed that if the extremely short pump pulse duration could be maintained during its conversion to an idler pulse, then the number of optical cycles within the pulse envelope would be reduced. However, the results didn't show this. The high peak powers associated with the pump pulse increased the effects of

self-phase modulation on the output pulses from the OPO and the extent of the temporal walk-away severely limited the gain.

The work described in Chapter 5 overcame some of the problems that arose in the experiments of Chapter 4. A linear Ti:sapphire laser was used as the pump source for a periodically poled RTA based optical parametric oscillator. This laser produced transform limited pulses of 25 fs at 830 nm with an average power of 1.1 W. The pulse durations of ~ 25 fs from this laser were around twice that of pulses from the ring cavity design described in Chapter 4, but the greatly improved stability of the linear cavity proved to be more important than minimising the pulse duration.

A PPRTA-based OPO was demonstrated as an alternative to the PPLN OPO as described in Chapter 4. Idler pulse durations of around 100 fs at 3.1 μm were obtained, although the time-bandwidth product of these pulses suggested the presence of frequency chirp. When the signal wave of the OPO was dispersion compensated, very broadband idler pulses were generated around 3.6 μm. These pulses had a FWHM bandwidth up to 550 nm and a base bandwidth of over a micron, sufficient to support pulses containing as few as three optical cycles. However, the spectra and autocorrelation results showed signs of multiple modes or double pulsing within the idler wave and subtle changes in the cavity configuration were ineffective in removing this effect.

In Chapter 6 the research aimed to solve the remaining problems that arose in the previous experiments, namely to limit the temporal walk-away effect as described in Chapter 4 and dispersion compensate the frequency-chirped idler output seen in Chapter 5. The experiments demonstrated an OPO system based on aperiodically poled lithium niobate, which was the first of its kind. It

was shown that a negatively chirped grating coupled with a positively chirped pump pulse generated significantly shorter mid-infrared pulses compared to a conventional uniform grating PPLN based OPO. The shortest pulses produced were 53 fs in duration which corresponds to 5 optical cycle pulses at 3 μm. With the help of an SHG FROG system based on a KDP crystal and a diode array, a more complete characterisation of the pump pulses was obtained.

The surprise result was the generation of extremely broad bandwidth pulses obtained when the OPO cavity was uncompensated (so had a highly chirped signal) and the crystal was orientated for positive grating chirp. Pulse bandwidths of up to 720 nm were recorded along with a few autocorrelations, which suggested highly chirped pulses. At this point the measurements of the idler pulses became a significant difficulty. The output power of the Ti:sapphire laser was almost 300 mW below its optimum due to the failing Millennia X cw pump laser. This ultimately reduced the idler output to the threshold for autocorrelation measurement. An attempt to dispersion compensate these idler pulses was made, but the germanium prism system proved too lossy for the already weak idler output. Unfortunately, without adequate temporal measurements we were unable to determine the exact processes making these very broad bandwidth pulses. If suitably dispersion compensated, these measurements imply adequate bandwidth to support pulses containing as few as two optical cycles, a significant step towards the elusive single cycle mid-infrared pulse.

The work on APPLN based OPOs has opened another avenue for mid-infrared femtosecond pulse generation. An aperiodically poled crystal has been shown to have a significant advantage in over the uniformly poled crystals for idler

pulse compression and future work could see nonlinearly chirped crystal gratings that would produce optimum compression for input pulses of arbitrary frequency chirp.

The generation and study of ultrashort pulses has now achieved a level of understanding that they are now becoming more common as a laboratory tool, rather than just an object of research. It is the push to shorter pulse durations and ultimately single or sub-cycle pulses that will extend the forefront of ultrashort pulse research to new and exciting territories.

7.1 References

1 A. Baltuska, Z. Y. Wei, M. S. Pshenichnikov, and D. A. Wiersma, *"Optical pulse compression to 5 fs at a 1-MHz repetition rate"*, Optics Letters **22,** 102-104 (1997).

2 I. G. Cormack, W. Sibbett, and D. T. Reid, *"Practical measurement of femtosecond optical pulses using time- resolved optical gating"*, Optics Communications **194,** 415-424 (2001).

Publications

Journal Publications

T. Beddard, W. Sibbett, D. T. Reid, J. Garduno-Mejia, N. Jamasbi, and M. Mohebi, *"High-average-power, 1-MW peak-power self-mode-locked Ti:sapphire oscillator"*, Optics Letters **24,** 163-165 (1999).

T. Beddard, M. Ebrahimzadeh, T. D. Reid, and W. Sibbett, *"Five-optical-cycle pulse generation in the mid infrared from an optical parametric oscillator based on aperiodically poled lithium niobate"*, Optics Letters **25,** 1052-1054 (2000).

D. T. Reid, P. Loza-Alvarez, C. T. A. Brown, T. Beddard, and W. Sibbett, *"Amplitude and phase measurement of mid-infrared femtosecond pulses by using cross-correlation frequency-resolved optical gating"*, Optics Letters **25,** 1478-1480 (2000).

Conference Publications

T. Beddard, Z. Penman, D. T. Reid, W. Sibbett, *"Self-starting megawatt self-mode-locked Ti:sapphire laser oscillator"*, In Conference on Laser and Electro-Optics, OSA Technical Digest (Optical Society of America, Washington DC, 1999)

T. Beddard, M. Ebrahimzadeh, D. T. Reid, W. Sibbett, *"Five optical cycle pulse generation in the mid-IR using aperiodically poled lithium niobate"*, In Conference on Laser and Electro-Optics, OSA Technical Digest (Optical Society of America, Washington DC, 2000)

T. Beddard, M. Ebrahimzadeh, D. T. Reid, W. Sibbett, *"Five optical cycle pulse generation in the mid-infrared from an optical parametric oscillator based on aperiodically-poled lithium niobate"*, In Conference on Laser and Electro-Optics/Europe, OSA Technical Digest (Optical Society of America, Washington DC, 2000)

Acknowledgements

I am indebted to my supervisor, Professor Wilson Sibbett, for his support and guidance throughout my time with his group. I am extremely grateful to Dr Derryck Reid for his invaluable help and patience with me in the lab.

Thanks to the entire w-squad group, new and old: Zoë Penman for help in the lab at the start, John-Mark Hopkins for his computer insights, Paul Faller for his programming help, Gareth Valentine for his office entertainment, David Birkin for his gadget talk and Tom Brown for his company after work on a Friday night in Laffertys. I would also like to Pablo Loza-Alvarez, Bill Sleat, Edik Rafailov, Grigori Sokolovski, Iain Cormack, Ben Agate, Jacqueline Hewett and Alan Kemp for their friendship and help during the past years.

I am forever indebted to Dawn for her encouragement, understanding and motivation and for supporting me these past few months without which this would have been impossible!

Finally I would like to thank all my family for their help and encouragement and for providing the invisible force that kept me going during the write-up!

This work was funded by the Engineering and Physical Sciences Research Council to whom I am very grateful.